COMPUTATIONAL & ANALYTICAL MODELING OF THE COLLAPSE RESISTANCE OF STEEL COLUMNS

by

Julie Elizabeth Fogarty

A dissertation submitted in partial fulfillment
of the requirements for the degree of
Doctor of Philosophy
(Civil Engineering)
in the University of Michigan
2015

Doctoral Committee:

Professor Sherif El-Tawil, Chair
Professor Jerome P. Lynch
Associate Professor Jason P. McCormick
Professor Jwo Pan

DEDICATION

To my mother

Barbara A. Fogarty

ACKNOWLEDGEMENTS

Numerous people helped contribute to my desire to pursue and my ability to complete the doctoral work presented herein. First, I would like to thank my advisor, Prof. Sherif El-Tawil, for his guidance and support over the past few years. As a research mentor, there are few who can match the enthusiasm and attention to detail that I have experienced with Prof. El-Tawil. Every research meeting where I entered lost and frustrated ended with a renewed sense of purpose and knowledge about how to approach my current problem. Prof. El-Tawil is the type of person who inspires me to strive for excellence in every aspect of my professional career because his passion for our field is contagious.

I would like to thank my other committee members, Prof. Jason McCormick, Prof. Jerry Lynch, and Prof. Jwo Pan, for their advice and support in completing this work. In particular, I would like to thank Prof. McCormick for being a sounding board and constantly reminding me that everything would work out and come together.

I would also like to thank Dr. Richard and Patricia Brown for their never ending enthusiasm and brilliant plans for my next great adventure. From proofreading college application essays to suggesting a PhD, it is difficult to imagine where I would be without their guidance.

I would like to thank the many friends I have made along the way who provided much needed stress relief through non-academic pursuits. In particular, Jason Mirjah, Alicia and Jonathan Zagel, Becky Hill, and Eric Owens, whose company made the journey much more pleasant.

The research presented in this dissertation was supported by the National Science Foundation (NSF) Graduate Student Research Fellowship under Grant No. DGE 0718128, the EERI/NEHRP FEMA Graduate Fellowship, US NSF grants CMMI-0928547 and CMMI-1344372, and the University of Michigan, in particular the Third Century Initiative. The MIDEN implementation work was conducted by Jeff Morris, Ted Hall and Eric Maslowski of UM's 3D Laboratory.

Finally, I would like to thank my family for their support. Long days in the office were made bearable thanks to my uncle, Bob Tholt, who sent care packages full of delicious snacks. Computer advice, occasional proofreading, and keeping me abreast on life outside of G.G. Brown was generously provided by my brother, Joe Fogarty. The largest debt of gratitude, however, is owed to the person who has contributed most to the person I have become today, my mother, Barb Fogarty. Her unconditional love and support has been the one constant in my life and for that I am extremely grateful.

TABLE OF CONTENTS

DEDICATION ..... **ii**

ACKNOWLEDGEMENTS ..... **iii**

LIST OF FIGURES ..... **xi**

LIST OF TABLES ..... **xviii**

ABSTRACT ..... **xx**

CHAPTER 1 INTRODUCTION **1**

1.1 GENERAL 1

1.1.1 Behavior of Locally Flange Damaged Steel Columns 1

1.1.2 Behavior of Steel Columns Subjected to Combined Axial and Cyclic Loading 2

1.2 OBJECTIVES 3

1.2.1 Behavior of Locally Flange Damaged Steel Columns 3

1.2.2 Behavior of Steel Columns Subjected to Combined Axial and Cyclic Loading 4

1.2.3 Visualization of Complex Spatial Arrangements using Virtual Reality 5

1.3 STRUCTURE OF THE DISSERTATION 5

1.4 PUBLICATIONS FROM THIS DISSERTATION 6

CHAPTER 2 COLLAPSE RESISTANCE OF LOCALLY DAMAGED STEEL COLUMNS **8**

2.1 GENERAL 8

2.2 LITERATURE REVIEW 8

2.3 ANALYTICAL APPROACH 10

2.3.1 Variational Approach 10
2.3.2 Equilibrium Approach 15
2.3.3 Plastic Capacity 15
2.4 COMPUTATIONAL APPROACH 18
2.4.1 Finite Element Model Validation 20
2.5 PARAMETRIC STUDY USING VARIATIONAL APPROACH 27
2.5.1 Location of Damage 27
2.5.2 Initial Imperfection 28
2.5.3 Assessment 29
2.5.4 Partial Flange Removal 29
2.5.5 Asymmetric Damage 31
2.5.6 W30x124 Modeling 32
2.5.7 Comparison of Variational and FEM Results 34
2.6 MODELING FOR DESIGN 36
2.7 PARAMETRIC STUDY USING EQUILIBRIUM APPROACH 38
2.7.1 Comparison Between Variational and Equilibrium Approaches 40
2.8 EMPIRICAL MODEL 41
2.8.1 Best Fit Equation 41
2.8.2 Validation of Empirical Model 43
2.8.3 Application and Limitations of Best Fit Equation 47
2.9 SUMMARY AND CONCLUSIONS 48
CHAPTER 3 BEHAVIOR OF STEEL COLUMNS SUBJECTED TO COMBINED AXIAL AND CYCLIC LATERAL LOADING 50

3.1 GENERAL 50
3.2 LITERATURE REVIEW 50
3.2.1 Computational Studies 51
3.2.2 Experimental Studies 53
3.3 CURRENT AISC SEISMIC DESIGN GUIDELINES 57
3.4 FINITE ELEMENT MODELING 60
3.4.1 Prototype Column Selection 60
3.4.2 Model Setup 63
3.4.3 Length, Boundary Conditions, and Loading Scheme 64
3.4.4 Failure Criterion 66
3.4.5 Measures of Performance 71
3.5 FINITE ELEMENT MODEL VALIDATION 72
3.5.1 Model Setup 72
3.5.2 Loading Scheme 74
3.5.3 Simulation Results 76
3.6 RESULTS OF PARAMETRIC STUDY 77
3.6.1 Flange Width-to-Thickness Ratio 78
3.6.2 Web Width-to-Thickness Ratio 82
3.6.3 Unbraced Length 83
3.6.4 Regression Analysis 84
3.7 EVALUATION OF CURRENT SEISMIC DESIGN GUIDELINES 86
3.7.1 Design Aid 89
3.8 CONCLUSIONS 91

CHAPTER 4 BEHAVIOR OF STEEL COLUMNS SUBJECTED TO COMBINED AXIAL AND MONOTONIC LATERAL LOADING 92

4.1 GENERAL 92

4.2 ANALYTICAL MODELING 92

4.2.1 Formulating the Problem 93

4.2.2 Solving the Problem 97

4.2.3 Obtaining Load Deflection Curves 101

4.2.4 Strength Curve 105

4.2.5 Parametric Study 108

4.2.6 Limitations of Analytical Model 114

4.2.7 Influential Parameters 114

4.3 FINITE ELEMENT MODELING 115

4.3.1 Model Setup 115

4.3.2 Loading Schemes 116

4.4 RESULTS OF LOAD THEN DRIFT PROTOCOL 117

4.4.1 Flange Width-to-Thickness Ratio 118

4.4.2 Web Width-to-Thickness Ratio 119

4.4.3 Regression Analysis 120

4.5 RESULTS OF DRIFT THEN LOAD PROTOCOL 122

4.5.1 Initial Axial Load 125

4.5.2 Lateral Drift 128

4.5.3 Interruption in Load Path 131

4.5.4 Effective Length Factor 137

4.6 CONCLUSIONS 140

CHAPTER 5 VISUALIZATION OF COMPLEX SPATIAL ARRANGEMENTS IN VIRTUAL REALITY 142

5.1 GENERAL 142

5.2 INTRODUCTION AND MOTIVATION 142

5.3 VIRTUAL REALITY MODELS 145

5.3.1 New Virtual Reality Tools 148

5.4 EVALUATION OF VR MODELS 152

5.4.1 Theoretical Framework 152

5.4.2 Methods 155

5.4.3 Results 161

5.4.4 Discussion 167

5.5 CONCLUSIONS 169

CHAPTER 6 SUMMARY AND CONCLUSIONS 171

6.1 SUMMARY 171

6.1.1 Behavior of Locally Flange Damaged Steel Columns 171

6.1.2 Behavior of Steel Columns Subjected to Combined Axial and Lateral Loading . 172

6.1.3 Visualization of Complex Spatial Arrangements using Virtual Reality 173

6.2 CONCLUSIONS 174

6.2.1 Behavior of Locally Flange Damaged Steel Columns 174

6.2.2 Behavior of Steel Columns Subjected to Combined Axial and Lateral Loading . 174

6.2.3 Visualization of Complex Spatial Arrangements using Virtual Reality 176

6.3 FUTURE WORK 176

6.3.1 Behavior of Locally Web-Damaged Steel Columns 176

6.3.2 Behavior of Steel Columns Subjected to Combined Axial and Cyclic Loading .. 176

6.3.3 Visualization of Complex Spatial Arrangements using Virtual Reality 177

REFERENCES 178

LIST OF FIGURES

Figure 1-1. Steel coupon removal (Images courtesy of Gilsanz, Murray, Steficek LLP). 2

Figure 2-1. a) Centerline of column where the centroid of the middle segment is shifted due to damage and b) Column ilustrating damaged flange section. 11

Figure 2-2. Strength and elastic stability limits 14

Figure 2-3. Stability curves for an undamaged W14x120 with different initial imperfections (L=5.17 m). 17

Figure 2-4. Maximum load carrying capacity for an undamaged column (W14x120, L=5.17 m, $l_1 = l_2 = l_3$, f_y=280 MPa) with different initial imperfections. 17

Figure 2-5. Finite element model of column with (a) damaged center segment and (b) damaged end segment. 19

Figure 2-6. LS-Dyna model simulating experimental test setup performed by Zeinoddini et al. (2002)..... 21

Figure 2-7. a) View of indenter from experimental setup (Zeinoddini et al. 2008), b) Indenter shape B, and c) Indenter shape C. 23

Figure 2-8. Schematic view of an impacted tube and the resulting dent, bowing, and axial shortening (Zeinoddini et al. 2002). 24

Figure 2-9. Post-impact view of a specimen with no axial pre-loading from experiment (right) and simulation (left) (Zeinnddini et al. 2008)..... 25

Figure 2-10. Post-impact view of a specimen with 70% axial pre-loading from experiment (right) and simulation (left) (Zeinoddini et al. 2008)..... 25

Figure 2-11. Comparison of experimental (solid lines) and numerical (dashed lines) time histories of axial load (Zeinoddini et al. 2002)..... 26

Figure 2-12. Relationship between axial capacity and location of damaged column segment. ... 28

Figure 2-13. Relationship between axial capacity and initial imperfection..... 29

Figure 2-14. Relationship between axial capacity and damage extent within cross-section. 31

Figure 2-15. Relationship between axial capacity and damage extent within cross-section for aysmmetric damage case. 32

Figure 2-16. Relationship between axial capacity and damage extent within cross-section. 33

Figure 2-17. Relationship between axial capacity and length of damaged center column segment for a) W14x120-C-W100 and b) W30x124-C-W100..... 35

Figure 2-18. Comparison of design model, Rayleigh-Ritz, and FE models 37

Figure 2-19. Comparison between analytical, FE model, and Rayleigh-Ritz solutions (W14x120, L = 5.17 m, $l_1 = l_2 = l_3$, f_y = 345 MPa, a_0/L = 0.002) 40

Figure 2-20. Comparison between analytical, FE model, and Rayleigh-Ritz solutions (W30x124, L = 5.17 m, $l_1 = l_2 = l_3$, f_y = 345 MPa, a_0/L = 0.002) 41

Figure 2-21. Relationship between maximum load carrying capacity versus A_d/A 42

Figure 2-22. Finite element models of a W18x119 column with 0.2L damage at a) center (0.5L) and b) quarter (0.25L) height..... 44

Figure 2-23. Comparison between Equation 2-14 and finite element results..... 45

Figure 3-1. Selected columns' slenderness ratios with respect to seismic design guideline limits59

Figure 3-2. Material model calibration with A913 Grade 50 steel coupon (Kaufman et al. 2001). 64

Figure 3-3. Finite element validation model showing mesh and boundary conditions. 65

Figure 3-4. Loading protocol for a) lateral displacement and b) axial load. 66

Figure 3-5. Failure criterion for 4.57 meter W36x487-0.2Py column based on a 10% reduction in a) moment and b) lateral force. 68

Figure 3-6. Progression of axial load failure for 4.57 meter W36x4987-0.7Py column as shown by a) last half-cycle able to reach target displacement under target axial load, b) inability to reach target axial load at target displacement, and c) sudden drop in axial load and increase in axial displacement. 69

Figure 3-7. Summary of failure criterion for 4.57 m W36x487 column with CALR shown. 70

Figure 3-8. Finite element validation model showing mesh and boundary conditions. 73

Figure 3-9. Comparison of a) moment versus lateral displacement, b) lateral force versus lateral displacement, and c) P-M interaction response between computational model (dashed lines) and experimental results (solid lines) for W14x132-75. Similar comparisons are shown in d-f for the W14x175-55. 75

Figure 3-10. Comparison of deformed member at 10% drift for a) W14x132-75 and b) W14x176-55 (Newell and Uang 2006). 77

Figure 3-11. Capacity of columns with trends regarding a) flange width-to-thickness ratio and b) web width-to-thickness ratio for (1) W18x86 – 15ft, (2) W30x326 – 20ft, (3) W14x132 – 15ft, (4) W14x500 – 15 ft, (5) W27x146 – 15ft, (6) W18x119 – 20ft, (7) W30x326 – 10ft, and (8) W14x500 – 15ft. 79

Figure 3-12. Displaced shape just prior to axial failure criterion for columns under $0.20P_y$ for extremes shown in Figure 3-11(a) 80

Figure 3-13. Displaced shape just prior to axial failure criterion for columns under $0.20P_y$ comparing a) different h/t_w (same b/t), and b) different b/t (similar h/t_w) 81

Figure 3-14. Displaced shape just prior to axial failure criterion for columns under $0.20P_y$ for extremes shown in Figure 3-11(b) 82

Figure 3-15. Axial load of W24x176 column versus (a) lateral drift ratio at moment failure criterion as well as column displaced shape (2x magnified) at moment failure for W24x176 with P/Py = 0.40 for unbraced lengths (b) 6.10 m, (c) 4.57 m, and (d) 3.04 m 84

Figure 3-16. Solid curves for logarithmic expectation function plotted for a) P/P_y = 0.3, b) P/P_y = 0.4, c) P/P_y = 0.5, d) P/P_y = 0.6, e) P/P_y = 0.7, *f)* P/P_y = 0.8 along with corresponding critical axial loads for each section from finite element data. 87

Figure 3-17. Comparison of members that could not sustain $0.2P_y$ up to 4% lateral drift (circles) with CALR prediction curves. 88

Figure 3-18. Plots of the test members with arrows indicating the predicated CALR based on the regression equation. 90

Figure 4-1. Deformation of member under combined loading scheme 94

Figure 4-2. Centerline of column where the centroid of the bottom segment is shifted due to damage and cross-section illustrating section with damaged flange 94

Figure 4-3. Buckled shape and resulting moments due to displacement (P_1) and rotation (P_2) of tip loads 95

Figure 4-4. Moment Components in X-Y and Y-Z planes 98

Figure 4-5. Lateral load P_2, versus lateral displacement, u. Asymptote at Equation 4-18. 103

Figure 4-6. Axial load, P_1, versus lateral displacement, u. Asymptote at $P_{cr} = P_y$. 104

Figure 4-7. Axial load, P_1, versus lateral displacement, v. Asymptote at $P_{cr} = P_x$. 104

Figure 4-8. Axial load, P_1, versus angle of twist, β. Asymptote at $P_{cr} = P_\varphi$ 105

Figure 4-9. Strength and stability curves for W30x124-W33..... 107

Figure 4-10. Axial capacity versus lateral displacement, v, for W18x119 under different lateral forces P_2 = 4.45 kN (diamonds), 44.5 kN (squares), and 90.0 kN (triangles) with damage length d 110

Figure 4-11. Axial capacity versus lateral displacement, u, for a) W14x132, b) W18x119, and c) W30x124 under different lateral forces P_2 = 4.45 kN (diamonds), 44.5 kN (squares), and 90.0 kN (triangles) with damage length d 111

Figure 4-12. Effect of amount of damage along length for W30x124..... 112

Figure 4-13. Selected columns' slenderness ratios with respect to seismic design guideline limits. Variations of the flange and web thickness of each section are represented by the shape of the original labeled section – W36x487 (circles), W14x176 (squares), W27x146 (diamonds), W24x117 (triangles). 118

Figure 4-14. Failure modes for a W36x487 with a a) halved flange, b) halved web, c) original properties, d) doubled web, and e) doubled flange under $0.60P_y$..... 120

Figure 4-15. Deformed shape at failure and shortly after failure under initial load $0.50P_y$ for a) W27x194 (Local - Global), b) W30x191 (Local - Transition), and c) W36x282 (Local) .. 125

Figure 4-16. Relationship between axial capacity at 4% drift with respect to slenderness ratios for different initial axial loads 127

Figure 4-17. Relationship between axial capacity at each drift level with respect to slenderness ratios for an initial axial load of $0.50P_y$. 130

Figure 4-18. Local buckling seen in W36x282 at 4% drift at point of failure..... 132
Figure 4-19. Relationship between axial shortening and amount of local buckling in flange and web under 0.25Py for 2% (square), 4% (circle), and 6% (triangle) lateral drifts for columns that experienced either a global failure mode (solid) or significant local buckling (unfilled) prior to global failure. 133
Figure 4-20. Stresses in cross-section over time with cross-section indicating elements that have yielded at failure (solid)..... 135
Figure 4-21. Stress distribution over cross section at a) end of drift – 4% drift, $0.25P_y$ (dotted line), b) 4% drift, $0.36P_y$ (dash-dotted line), c) 4% drift, $0.74P_y$ (dashed line), and d) failure – 4% drift, $0.82P_y$ (solid line) 136
Figure 4-22. Relationship between initial axial load and the effective length factor for 4% lateral drift 138
Figure 4-23. Relationship between 2% (circle), 4% (triangle), and 6% (square) drift levels and the effective length factor 138
Figure 5-1. AISC Steel Sculpture as a a) physical model (www.aisc.org) and b) proposed virtual reality model. 144
Figure 5-2. User in the CAVE-like environment used in this study. 146
Figure 5-3. Users in the UM-MIDEN with the headset and hand tracking devices. 147
Figure 5-4. Several participants using a Portable VR System (Oculus Rift). 147
Figure 5-5. Static model of the AISC Steel Sculpture in the UM-MIDEN 148
Figure 5-6. View 'floating' above the sculpture. 149
Figure 5-7. View 'peering' in on a connection. 149
Figure 5-8. Translucence of the model is illustrated by the bottom left white beam 150

Figure 5-9. Five columns at various time steps illustrating a) weak-axis flexural, b) strong-axis flexural, c) torsional, d) local flange, and e) local web buckling. 151
Figure 5-10. Additional views of global and local buckling behavior 152
Figure 5-11. Test questions used to assess student understanding of buckled shapes. 156
Figure 5-12. Students interacting with the buckling columns in the MIDEN. 159
Figure 5-13. Students using the portable head mounted devices. 160
Figure 5-14. Relation among the patterns identified in the data. 169

LIST OF TABLES

Table 2-1. Material Properties 21

Table 2-2. Results from Different Indenter Shapes 23

Table 2-3. Comparison of Impact Test Results. 24

Table 2-4. Removal of Flange within Cross-Section. 30

Table 2-5. W14x120-C-100 36

Table 2-6. W30x124-C-W100 36

Table 2-7. W14x120-C-W100 DM Comparison with FE and R-R Models 38

Table 2-8. W30x124-C-W100 DM Comparison with FE and R-R Models 38

Table 2-9. List of studied parameters (Yossef et al. 2014). 39

Table 2-10. Comparison between Equation 2-14, R-R Method, and FE 43

Table 2-11. Comparison of Equation 2-14 and FE models with changes in A_d/A 46

Table 2-12. Comparison of Equation 2-14 and FE models with different locations of damage .. 46

Table 3-1. Current AISC Seismic Design Guidelines (ANSI/AISC 2010) 58

Table 3-2. Column data used for regression analysis and comparison with expected axial load. 61

Table 3-3. Loading sequence after initial axial gravity load is applied. 66

Table 3-4. Summary of drift reached based on different failure criteria under various axial loads for a 4.57 m W36x487 column. 70

Table 3-5. Evaluation of plotted regression using test sections. 90

Table 4-1. Deflected shape functions. 100

Table 4-2. Strong and weak axis capacities for different flange and web thicknesses 113

Table 4-3. Column data used for regression analysis and comparison with expected axial load116

Table 4-4. Sections investigated using DTL scheme. 123

Table 4-5. Failure modes for different levels of lateral displacement under an initial axial load of $0.25P_y$ 129

Table 4-6. Final axial load for different levels of initial axial load at each drift level. 129

Table 4-7. Parameters used to measure local and global behavior at 4% drift under $0.25P_y$ 133

Table 4-8. Predicted K_y value based on geometric properties. 139

Table 4-9. Predicted axial capacities using proposed modified effective length factor for 4% lateral drift. 140

Table 5-1. Codes applied to interviews and survey responses 162

Table 5-2. Descriptive statistics for variables related to test scores 164

Table 5-3. Comparison of means for participants with different VR techniques. 164

Table 5-4. Comparison of means between VR users and non-users 164

ABSTRACT

Understanding steel column behavior under extreme events is necessary for the safe and efficient design of steel structures. To improve this understanding, steel columns that have experienced local flange damage as well as those subjected to a combined axial and lateral loading scheme are investigated. Educational tools to better visualize steel column behavior are also presented. Given the widespread use of steel structural systems, results from this work have the potential to save many lives through improved structural design and better evaluation of structural integrity following an extreme event.

Locally flange damaged steel columns are investigated analytically and computationally to quantify the effect of damage extent and location on column load carrying capacity. Results from these studies indicate that the compressive strength of steel columns can be severely reduced following local flange damage. A simplified design model and empirical equation are presented for use by practicing engineers as a means of approximating this reduced capacity.

To address extreme seismic events, steel columns subjected to a combined axial and cyclic lateral loading scenario are studied using detailed finite element models. Regression analysis indicates that the current seismic design guidelines are not conservative. A design aide is proposed for highly ductile members using the statistically significant parameters.

Additional combined axial and monotonic lateral loading studies using analytical and computational models are undertaken to better understand column behavior. An increase in local buckling due to increased axial loads or lateral drift not only interrupts the load path, but also

weakens the boundary conditions. While the interruption due to local buckling alone is insignificant, the additional alteration of the boundary conditions can lead to lower axial capacities than expected. Modified effective length factors are proposed as a means of approximating the axial capacity of a column under this loading scenario.

The ability to communicate and increase understanding of steel column behavior is addressed using newly developed virtual reality models that are deployed in the undergraduate steel design course. Quantitative and qualitative evaluation of the impact of these models on improving student understanding of buckled shapes is also presented.

CHAPTER 1

INTRODUCTION

1.1 GENERAL

Steel columns are thin walled structural members that may be deliberately or accidentally damaged by the application of localized heating, cutting or out of plane forces on their component plates. Local damage may also be induced by loading scenarios associated with extreme events, e.g. the formation of local buckling in plastic hinge regions under seismic loading. Local damage can potentially interrupt the axial load path in a steel column, adversely affecting its collapse behavior and capacity.

The behavior of locally damaged steel columns has received little attention so far despite broader implications for the integrity of the supported structure due to the susceptibility of these compromised columns to sudden compressive failure. To address this lack of knowledge, studies regarding the general behavior of locally flange damaged columns as well as how local instabilities affect the behavior of steel columns under combined axial and lateral loading schemes are presented in this work. Further introduction regarding each of these areas is presented below.

1.1.1 Behavior of Locally Flange Damaged Steel Columns

Several recent studies have investigated how blast and impact events cause damage in steel columns. Lee et al. (2009) investigated the behavior of wide flange columns subjected to blast

load as a part of an effort to mitigate blast-induced hazards in steel frame structures. Ferrer et al. (2010) used finite element modeling to evaluate the capacity of steel columns damaged by vehicle impact. These studies and others like them are examples of research in which the conditions leading to local damage were studied, but not the effect of such damage on the load carrying capacity of the column members, as is done herein. Little is known about the effect on axial capacity of even routine events, such as steel coupon removal from flanges, as shown in Figure 1-1.

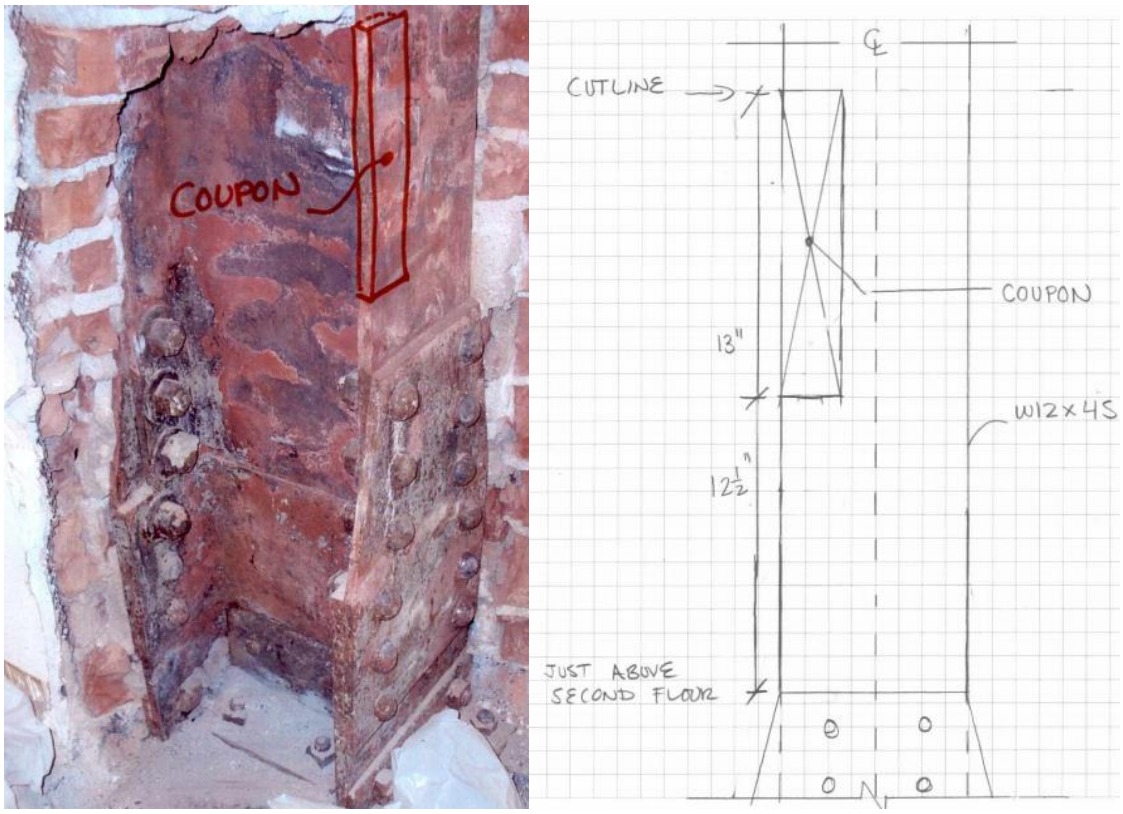

Figure 1-1. Steel coupon removal (Images courtesy of Gilsanz, Murray, Steficek LLP).

1.1.2 Behavior of Steel Columns Subjected to Combined Axial and Cyclic Loading

The fractures seen in steel moment resisting frame connections after the 1994 Northridge earthquake led to formation of the SAC Steel Project and multiple investigations regarding steel

moment frame design. The conclusions from these studies led to an increase in typical column cross-section depth due to more stringent requirements for strong column-weak beam criteria and balanced panel zone design. While deep (larger than W16) column sections now have widespread use in special moment resisting frames, there is a lack of knowledge regarding the sections under combined axial and reversed lateral loading. The fact that these deeper sections are more vulnerable to lateral torsional buckling and can be subjected to high axial loads due to seismically induced overturning moments indicates an urgent need to verify the structural integrity of column sections used in current seismic design. Another key concern is the development and growth of local buckling in plastic hinge regions as cyclic loading progresses, as observed both computationally and experimentally (Krishnan and Muto 2012, Lamarche and Tremblay 2011, Suita et al. 2007, Suita et al. 2008, Newell and Uang 2006). Since local flange and web buckling may interrupt the axial load path, these deep, slender sections may be particularly susceptible to a signifcant reduction in axial capacity, which neccessitates a better understanding of their behavior under seismic loading.

1.2 OBJECTIVES

The overarching goal of this dissertation is to understand column behavior, especially under extreme events. Several objectives are outlined below to address the concerns introduced previously. An additional educational research objective is presented as part of this work to aide instructors and students in communicating about and understanding column buckling behavior.

1.2.1 Behavior of Locally Flange Damaged Steel Columns

The objective of this work is to develop a greater understanding of the vulnerability of steel columns to localized damage. Using analytical techniques, supported by computational models,

the intent is to develop a simplified model that can be used to provide a quick and reasonable estimate of the residual capacity of compromised steel columns. Such information can be used by engineers to quickly assess column capacity in the presence of localized damage.

1.2.2 Behavior of Steel Columns Subjected to Combined Axial and Cyclic Loading

The objective of this study is to use computational models, validated with available test data, to address the following questions:

- What is the quantitative effect of local buckling on the axial resistance of steel wide-flange columns subjected to reversed lateral loading? In particular, how much of a role does local buckling as a result of seismic loading play in promoting progressive collapse?
- Under what conditions does local buckling promote flexural and lateral-torsional buckling? How do synergistic effects between local and global buckling evolve under cyclic loading conditions?
- Do the current general member requirements provided by AISC 341-10 Chapter D provide reliable design guidelines for wide-flange steel sections typically used in moment-resisting frames?

While a wide range of sections will be investigated, emphasis will be placed on the behavior of steel wide-flange members particularly susceptible to local buckling. This information will be used to further the general understanding of steel column behavior and provide data for future guidelines on general member requirements for seismic design.

1.2.3 Visualization of Complex Spatial Arrangements using Virtual Reality

The objective of this work is to develop virtual reality (VR) models and evaluate their impact using mixed methods. Ideally, these VR models will provide an interactive, exciting way for students to improve their understanding of complex spatial arrangements and encourage them to pursue a career in civil engineering. An evaluation of these tools will provide an understanding of what is difficult for students to grasp about complex spatial arrangements and how the VR tools are addressing those difficulties.

1.3 STRUCTURE OF THE DISSERTATION

A brief description of each of the seven chapters of this report is provided below.

Chapter 1: Introduction. A general overview of the motivation and objectives of this research is presented. The scope of this work and an introduction to the content to follow is also provided.

Chapter 2: Collapse Resistance of Locally Flange Damaged Steel Columns. An analytical method in conjunction with detailed finite element models are presented as a means of predicting the reduced capacity of locally damaged steel columns. These tools are used to investigate the important parameters affecting column capacity in the event of localized flange damage. Simplified procedures that can be used in a design office as well an empirical equation that can be used in the field for predicting residual axial capacity are also presented.

Chapter 3: Behavior of Steel Columns Subjected to Combined Cyclic Axial and Lateral Loading. Detailed finite element models that are validated using available experimental data are presented. An extensive parametric study is undertaken using the detailed finite element models and a statistical analysis is performed to determine the most influential parameters on predicting

the capacity of a section under a combined axial and cyclic loading scheme. A simple-to-use design aide is also presented as a supplement to current AISC seismic design guideline member requirements.

Chapter 4: Behavior of Steel Columns Subjected to Combined Monotonic Axial and Lateral Loading. An analytical method that captures torsional and local instabilities is presented as a means of understanding the effects of various parameters on the capacity of steel columns. To better understand the critical components affecting steel column performance under a combined axial and lateral loading scheme, detailed finite element models are also presented. Modification of the effective length factor is proposed as a means of predicting the capacity of members subjected to this combined loading scheme.

Chapter 5: Exploring Complex Spatial Arrangements in Virtual Reality. Virtual reality tools to aid student understanding of the behavior of structural components as they deform are presented. The impact of these tools on student learning using qualitative and quantitative methods is also discussed.

Chapter 6: Summary and Conclusions. Key findings and contributions that can be extracted from this work are summarized. Recommendations for future research related to understanding column behavior under extreme events are also included.

1.4 PUBLICATIONS FROM THIS DISSERTATION

Chapter 2 is published in two journal papers. Chapter 3 has been accepted for publication. Chapter 4 is in preparation and will soon be submitted for publication. Chapter 5 is currently under review. Details are listed below:

Fogarty, J., Yossef N.M., and El-Tawil, S. (2013). "Collapse Resistance of Locally Damaged Steel Columns." *J. of Constructional Steel Research,* 82, 195–202. **(Chapter 2)**

Yossef N.M., **Fogarty, J.**, and El-Tawil, S. (2014). "Residual Compressive Strength of Flange-Damaged Steel Columns." *J. of Structural Engineering.* **(Chapter 2)**

Fogarty, J. and El-Tawil, S. "Collapse Resistance of Steel Columns under Combined Axial and Lateral Loading" *J. of Structural Engineering,* Accepted. **(Chapter 3)**

Fogarty, J. and El-Tawil, S. "Steel Column Behavior under Combined Axial and Lateral Loading," In preparation. **(Chapter 4)**

Fogarty, J., McCormick, J. and El-Tawil, S. "Improving Student Understanding of Complex Spatial Arrangements with Virtual Reality" *J. of Engineering Education,* Submitted May, 2015. **(Chapter 5)**

CHAPTER 2

COLLAPSE RESISTANCE OF LOCALLY DAMAGED STEEL COLUMNS

2.1 GENERAL

This chapter begins with an overview of the literature relevant to locally damaged steel columns and is followed by the presentation of an analytical model based on the variational Rayleigh-Ritz technique to quantify the effect of damage extent and location on column load carrying capacity. The results of an equilibrium based analytical approach are also discussed. Detailed finite element models that are validated using available experimental results are also presented and used to parametrically investigate column capacity in the presence of localized damage.

2.2 LITERATURE REVIEW

Prior work evaluating the residual axial strength of laterally impacted steel columns has focused on tubular members used in offshore structures. Zeinoddini et al. (1999) first attempted to provide a more accurate model of a ship impact situation by assessing the dynamic stability of an axially pre-loaded steel tubular member through numerical models. They concluded that maintaining the axial pre-load during and after impact has the potential to significantly affect the residual capacity and stability of the member. An experimental set up was then devised by Zeinoddini et al. (2002) to provide benchmark data on the response of axially loaded steel tubes subjected to lateral dynamic impact loads.

Al-Thairy and Wang (2011) numerically investigated the effects of impact velocity, impact location, axial compressive load, impactor mass, and column slenderness ratio on the behavior and buckling of laterally impacted steel UC columns under axial pre-loading. The primary mode of failure for the axially unrestrained columns was global buckling and dependent on the level of impact kinetic energy. While large local flange distortion occurred at the impact location, the authors concluded that local distortion was a result and not cause of the global column failure.

Trahair et al. (2005) explored the effect of out-of-tolerance crookedness on column behavior. They suggested that the deflection caused by an impact event can be regarded as an initial crookedness and used in computation of column capacity. They also noted that damaged columns can have significant residual capacity.

Abd El-Lateef et al. (2001) investigated the elastic stability of columns in which holes were drilled. The investigation was conducted using a minimum potential energy technique and considered the effect of various boundary conditions as well as hole size and location. In a follow up study, Abd El-Lateef et al. (2001) extended their research to address columns with variable cross-sections and various types of loading conditions. The stability of eccentrically loaded steel columns with tapered and stepped cross-sections and the effect of initial imperfections was studied by Raftoyiannis and Ermopoulos (2005). The problem was addressed by solving the governing differential equations for buckling of a column with variable cross-sections. Nonlinear finite element analyses were performed to verify the analytical results. The Abd El-Lateef et al. (2000 and 2001) and Raftoyiannis and Ermopoulos (2005) studies did not explicitly consider the response of damaged columns, but their results have bearing on the work presented herein.

2.3 ANALYTICAL APPROACH

2.3.1 Variational Approach

A variational approach is used to gain insight into the effect of local damage on the critical buckling load of steel columns. The critical load of a flange-damaged column as depicted in Figure 2-1 is determined analytically using the Rayleigh-Ritz method with the following assumptions:

- Perfect supports, i.e. no eccentricity.
- Deformed shape is sinusoidal.
- Damaged part does not affect the assumed deformed shape.
- Lateral torsional buckling does not play a role in the response.
- Elastic behavior.
- Damage is symmetric, i.e. occurs to both flanges equally, and response is also symmetric, i.e. no out of plane behavior.

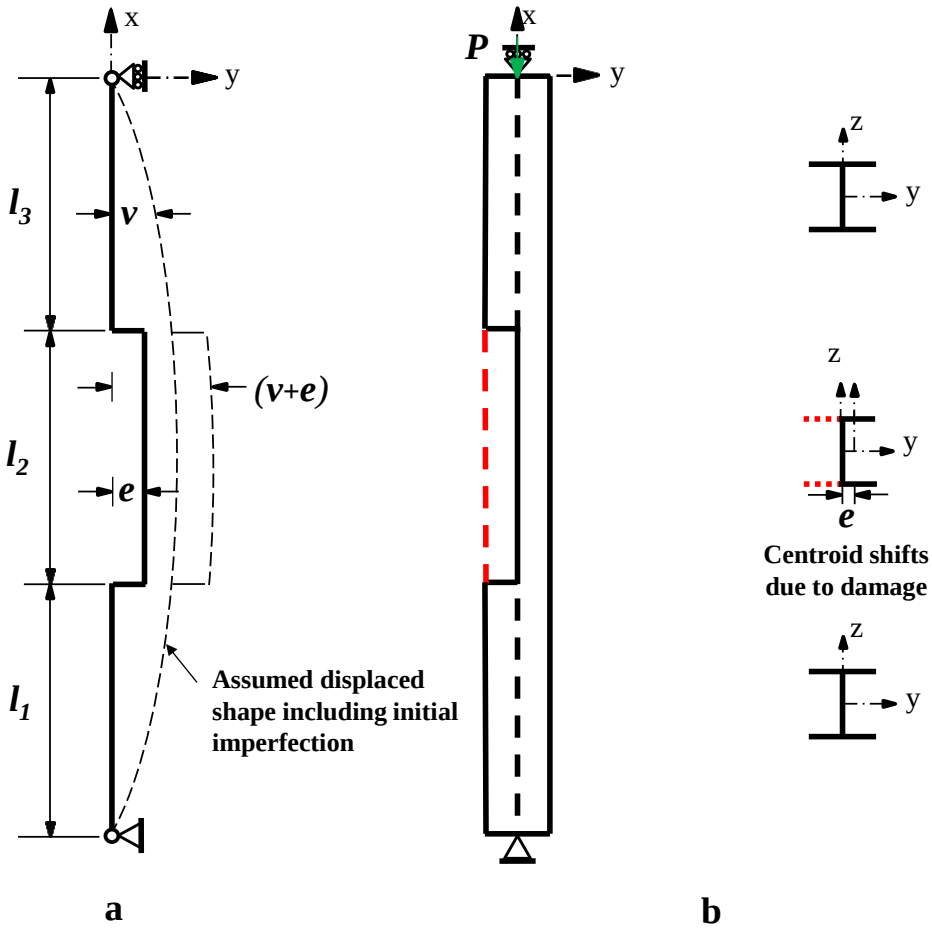

Figure 2-1. a) Centerline of column where the centroid of the middle segment is shifted due to damage and b) Column ilustrating damaged flange section.

In Figure 2-1, a column is assumed to be comprised of 3 segments. Flange damage is assumed to occur in the middle portion. As a result, the damaged cross-section in the center segment is no longer bi-symmetric, creating an effective eccentricity, *e*, in axial loading on this segment.

Using the Rayleigh-Ritz method (Chajes 1974, Cook et al. 2001), the energy functional for a column with total length *L* can be written as:

$$\Pi_p = \frac{1}{2}\int_0^L EAu_x^2 dx + \frac{1}{2}\int_0^L EIv_{xx}^2 dx + \int_0^L \frac{P}{2} v_x^2 dx - P \cdot u(L) \qquad 2\text{-}1$$

Where L is the total member length, E is the modulus of elasticity, I is the moment of inertia, A is the cross-sectional area, u is the axial displacement, v is the lateral displacement, P is the applied axial load, and the use of a subscript implies differentiation with respect to the subscript.

The second term is recast as follows. This is not only a simpler representation, but also takes advantage of the fact that utilizing a function instead of a derivative of the function generally results in a smaller error (Chen and Lui 1986).

$$\frac{1}{2}\int_0^L EIv_{xx}^2 dx = \frac{1}{2}\int_0^L \frac{M^2}{EI} dx = \frac{1}{2}\int_0^L \frac{(P\cdot v)^2}{EI} dx \tag{2-2}$$

Thus the equation to describe the column in Figure 2-1, where the total length is divided into three lengths, l_1, l_2, and l_3, and the subscript d refers to the damaged section properties respectively, can be written as:

$$\begin{aligned}\Pi_p = &\frac{1}{2}\int_0^{l_1} EAu_x^2 dx + \frac{1}{2}\int_0^{l_1} \frac{(P\cdot v)^2}{EI} dx \\ &+ \frac{1}{2}\int_{l_1}^{l_1+l_2} EA_d u_x^2 dx + \frac{1}{2}\int_{l_1}^{l_1+l_2} \frac{\left(P\cdot(v+e)\right)^2}{EI_d} dx \\ &+ \frac{1}{2}\int_{l_1+l_2}^{L} EAu_x^2 dx + \frac{1}{2}\int_{l_1+l_2}^{L} \frac{(P\cdot v)^2}{EI} dx + \int_0^L \frac{P}{2} v_x^2 dx - P\cdot u(L)\end{aligned} \tag{2-3}$$

The following functions are assumed to describe the deformed shape of a pinned-pinned column:

$$u = ax \tag{2-4}$$

$$v = b\,sin\left(\frac{\pi x}{L}\right) \tag{2-5}$$

Where a and b are Rayleigh-Ritz variables. Equation 2-4 implies that the axial deformation varies linearly, while Equation 2-5 indicates that the assumed lateral deflection varies sinusoidally. When $e = 0$ (no damage), variation of (2-3) with respect to b leads to:

$$P_{cr} = -\frac{\pi^2 EI}{L^2} \tag{2-6}$$

which is the exact Euler buckling load of the column. When $e \neq 0$ (damage is present as shown in Figure 2-1), and assuming that the column segments are thirds, variation of (2-3) with respect to b leads to

$$P = -\frac{6\pi^3 bEII_d}{L^2[b\left(3I_d\sqrt{3} + 3I\sqrt{3} + 4I_d\pi + 2I\pi\right) + 12Ie]} \tag{2-7}$$

Equation 2-7 is essentially a relationship between the applied axial load and the lateral displacement of the column, as determined by b. Solving (2-7) for b yields:

$$b = -\frac{12IPL^2e}{3PIL^2\sqrt{3} - 3PI_dL^2\sqrt{3} + 2PIL^2\pi + 4PI_dL^2\pi + 6\pi^3 EII_d} \tag{2-8}$$

Substituting b into (2-5) and plotting P with respect to v yields an elastic stability curve as seen in Figure 2-2 where the values for a 5.3 m W14x120 pinned-pinned column are employed. The influence of the damaged moment of inertia as well as the eccentricity are evident in (2-7) and (2-8), particularly the fact that as the eccentricity increases, the critical buckling load decreases.

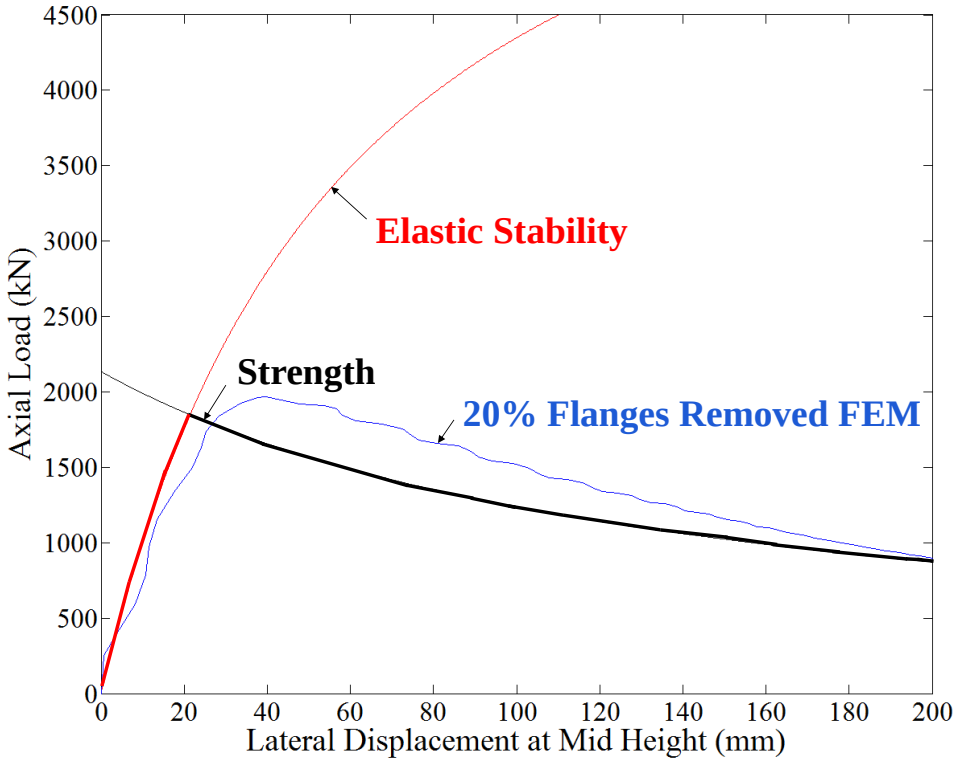

Figure 2-2. Strength and elastic stability limits

The effect of an initial imperfection can also be included in the energy functional. The initial imperfection, like the lateral deflection, is assumed to vary sinusoidally with a maximum deflection of L/500 at mid-height of the column. It can be integrated into (2-3) by modifying the second, fourth, and sixth terms that take into account flexural energy. For example, the addition of (2-9) to the lateral deflection, *v*, as it is multiplied by the applied axial load, *P*, as shown for the second term of (2-3) in (2-10) accounts for the additional bending energy caused by the assumed initial imperfection when present.

$$\frac{L}{500}\sin(\frac{\pi x}{L}) \qquad 2\text{-}9$$

$$\frac{1}{2}\int_0^l \frac{\left(P\cdot\left(v+\frac{L}{500}\sin\left(\frac{\pi x}{L}\right)\right)\right)^2}{EI}dx \qquad 2\text{-}10$$

2.3.2 Equilibrium Approach

An alternative approach using the principles of equilibrium was also developed in Yossef et al. (2014). In this approach, the governing differential equation for buckling of a column with non-uniform cross section was formulated. By applying the necessary equilibrium and compatibility boundary conditions between the various column segments (shown in Figure 2-1), the problem was solved, yielding the solution obtained from the variational approach. Although considerably more complex than the variational method presented above, employing the equilibrium approach provides confidence that the solutions obtained above are reasonable. Comparison and validation of the equilibrium approach is discussed below.

2.3.3 Plastic Capacity

As an imperfect steel column is loaded, nonlinear geometric effects will cause an increase in the applied moments at all cross-sections within the column, causing the column to gradually buckle out of plane. The critical cross-section, i.e. the one where the demand to capacity ratio – in the axial-moment interaction sense - is highest, will form a plastic hinge precipitating failure of the column. The critical cross-section will more likely occur in the damaged segment, especially if it is in the middle, because the loss of portions of the flanges will reduce capacity in that region.

The previous derivations pertain to elastic stability only and do not account for the inelastic behavior of the column. Using simple plastic analysis and enforcing the AISC-LRFD (2010) moment versus axial load interaction relationship in (2-11) for axial loads greater than $0.20P_y$,

the relation between applied axial load and v is derived as shown in (2-13), where v_0 is the initial column imperfection, M_{pd} is the plastic moment capacity of the center (damaged) segment, and A_d is the cross-sectional area of the damaged segment.

$$\frac{P}{A_d f_y} + \frac{8}{9}\frac{M}{M_{pd}} = 1.0 \qquad 2\text{-}11$$

$$M_p = P * (v + e + v_0) \qquad 2\text{-}12$$

$$P = \frac{9M_{pd}A_d f_y}{8A_d f_y(v + e + v_0) + 9M_{pd}} \qquad 2\text{-}13$$

The results of (2-13) are plotted in Figure 2-2 for the variational approach. Assuming no interaction between elastic stability response and inelastic behavior, the heavy curves in Figure 2-2 are a representation of the load versus lateral deflection response of the column.

With respect to the equilibrium based approach, the capacity of the undamaged column, designated P_u henceforth, is assumed to be reached when the elastic stability curve (obtained in Yossef et. al (2014)) intersects the plastic strength curve plotted by Equation 2-13. Figure 2-3 shows the details of the computations for an undamaged column with different levels of initial imperfection. As shown in Figure 2-4 the presence of cross-sectional damage pushes down both elastic and plastic curves, lowering their intersection point, signifying a reduction in load carrying capacity of the damaged column, designated P_{ud} henceforth.

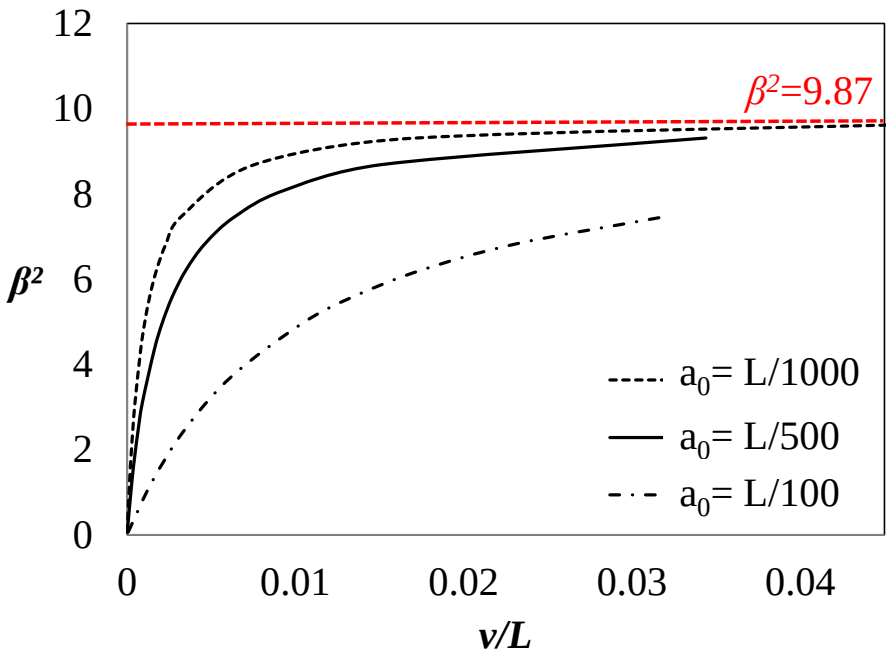

Figure 2-3. Stability curves for an undamaged W14x120 with different initial imperfections (*L*=5.17 m).

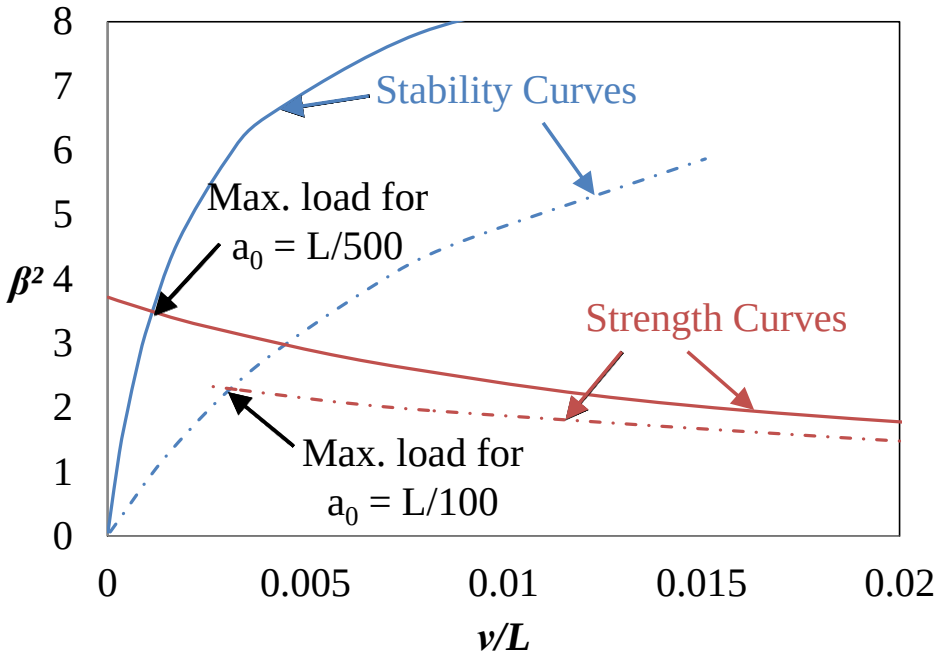

Figure 2-4. Maximum load carrying capacity for an undamaged column (W14x120, *L*=5.17 m, $l_1 = l_2 = l_3$, f_y=280 MPa) with different initial imperfections.

2.4 COMPUTATIONAL APPROACH

Two prototype columns are selected to investigate collapse resistance in the presence of local damage. The first is a 5.3 m W14x120 column, which represents a typical gravity column in a 10-story building whose resistance to progressive collapse was studied by Khandelwal et al. (2008). Unlike columns in moment bays, which are primarily designed to provide lateral resistance and are therefore lightly loaded in compression, gravity columns generally carry a heavy axial load and can be particularly susceptible to localized damaged. To determine if the characteristics of the cross-section play a role in the behavior of the columns, a 5.3 m W30x124 column is also investigated. This section is chosen due to its similar area but significantly different aspect ratio when compared with the W14x120 column.

Both columns are discretized using the commercial software Hypermesh (2011) as shown in Figure 2-5. The columns are modeled using fully integrated Belytschko-Wong-Chiang shell elements. Rigid plate caps are attached at either end to distribute the applied loads over the entire cross section without causing local deformation. As shown in Figure 2-5, rotation around the web is permitted at the lower end, while rotation around the web and vertical (z) translation are permitted at the top end. An initial imperfection with an assumed sinusoidal shape with a maximum deflection of $L/500$ at the mid-height is implemented. This maximum imperfection is greater than the $L/1000$ assumed in AISC (2010) to indirectly account for residual stresses, which are not included in the simulation. Figure 2-5 shows an example of the models utilized herein and the imposed boundary conditions.

After removal of the flanges in the center or end segment of the column to simulate flange damage (see Figure 2-5(a) and Figure 2-5(b), respectively), a displacement controlled load is

applied at the rate of 42.4 mm/sec to determine the capacity of the pinned-pinned column. The loading rate is selected through a trial and error process as a compromise to reduce computational run time while minimizing the dynamic effects associated with rapid loading. The models are built in the same general manner as those used in the validation scheme described next and solved on the LS-DYNA (2005) platform.

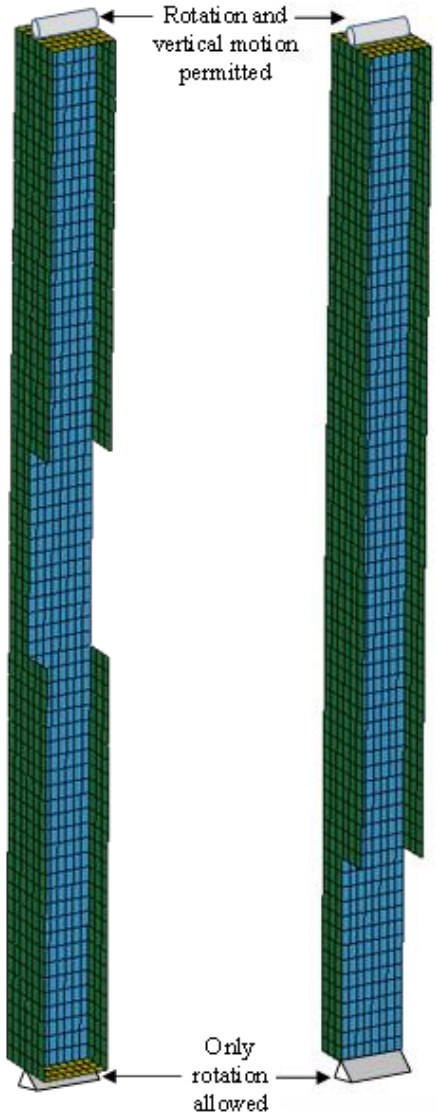

Figure 2-5. Finite element model of column with (a) damaged center segment and (b) damaged end segment.

2.4.1 Finite Element Model Validation

Zeinoddini et al. (2002) conducted tests of tubular members that were laterally impacted while subjected to a sustained axial load. These tests were the only ones the author was able to find that address steel column stability in the presence of localized damage. They therefore represent a unique opportunity to validate the finite element models developed in this work.

2.4.1.1 Model Setup

A detailed finite element model of the test set up is created using the commercial code LS-DYNA (2005). The model involves five major components and its properties are based on the measured information reported in Zeinoddini et al. (2002). The tubular specimen, consisting of fully integrated Belytschko-Wong-Chiang shell elements, measures 1000 mm in length and 1.99 mm in thickness with a center-to-center diameter of 99.98 mm. Material properties are listed in Table 2-1. Rigid links are used to connect the circumferential nodes to a central node at each end of the tubular specimen. The central node at the right end in Figure 2-6 is constrained against all translations and rotations. A spring with stiffness 1667.7 N/mm is attached to the central node on the left end (labeled A in Figure 2-6) and a node 350 mm to the left of the tubular specimen (labeled B in Figure 2-6). Both nodes A and B are constrained against all rotations and translations except for translation in the longitudinal direction. An initial displacement was applied to node B to simulate the action of the hydrualic jack in the test, which applies an axial load to the test setup through spring AB.

Table 2-1. Material Properties

Component	E (GPa)	ρ (tonne/mm^3)	σ_y (N/mm^2)	σ_u (N/mm^2)
Tubular Specimen	200,000	7.85E-09	498.5	532
Indenter	206,820	7.75E-09	-	-
Load Cell	200,000	7.85E-09	-	-
Weight Block	200,000	3.27E-08	-	-

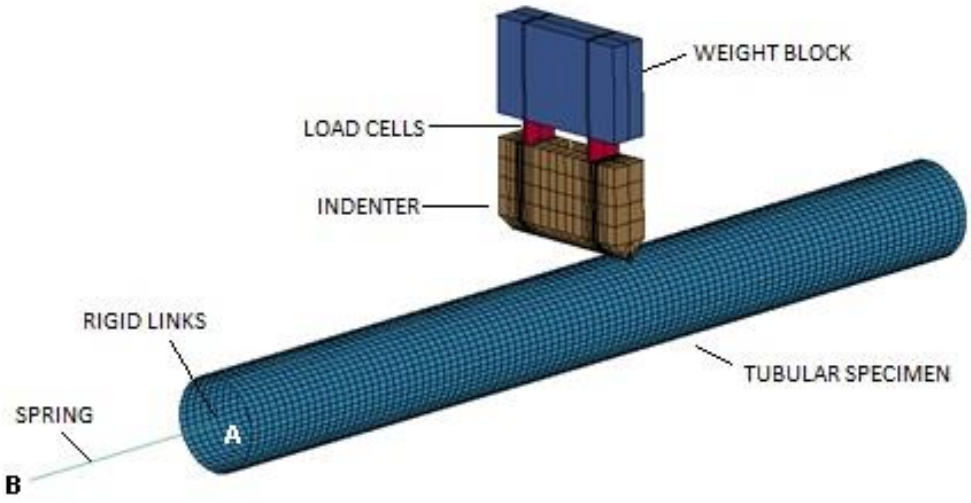

Figure 2-6. LS-Dyna model simulating experimental test setup performed by Zeinoddini et al. (2002).

A small load is also placed on the tubular specimen at midspan to cause an initial imperfection of 0.52 mm meant to imitate the measured out-of-straightness. To address the strain rate sensitivity that arises from the short impact duration, values of C=100 and q=10 for the Cowper-Symonds equation in LS-DYNA (2005) are incorporated in the tubular specimen material model. These values were utilized by Zeinoddini et al. (1999) in their numerical model and reflect coefficients obtained from comparisons with existing experimental data for a similar material (Zeinoddini et a. 2008, Jones 1989).

The striker consists of the indenter, load cells, and weight block. Each component is made up of fully integrated brick elements with material properites listed in Table 2-1. The total weight of

the striker is 25.450 kg and impacts the tubular specimen with a velocity of 7 m/s. Interpenetration between all components is prohibited.

2.4.1.2 Mesh Sensitivity

A mesh sensitivity study is first performed to ensure that the mesh being used leads to reasonable results. The mesh used by Zeinoddini et al. (2008) was initially considered but due to the high aspect ratio of the elements near the region of impact, smaller elements with an aspect ratio closer to unity are chosen herein. The final mesh seen in Figure 2-6 is selected because there are insignificant changes in the results upon furthering mesh refinement.

2.4.1.3 Indenter Model

The shape of the indenter was not explicitly described in Zeinoddini et al. (2002) other than to say that it was "sufficiently rounded to avoid the occurrence of local tearing in the specimen". The clearest image of the indenter can be seen in Figure 2-7a and two different approximations of the shape are utilized (Figure 2-7b and Figure 2-7c) to determine if the shape has any effect on the results. As seen in Table 2-2, the shape of the indenter plays a minor role in the amount of damage that occurrs to the tubular specimen. The indenter shape seen in Figure 2-7b is chosen for further validation of the model.

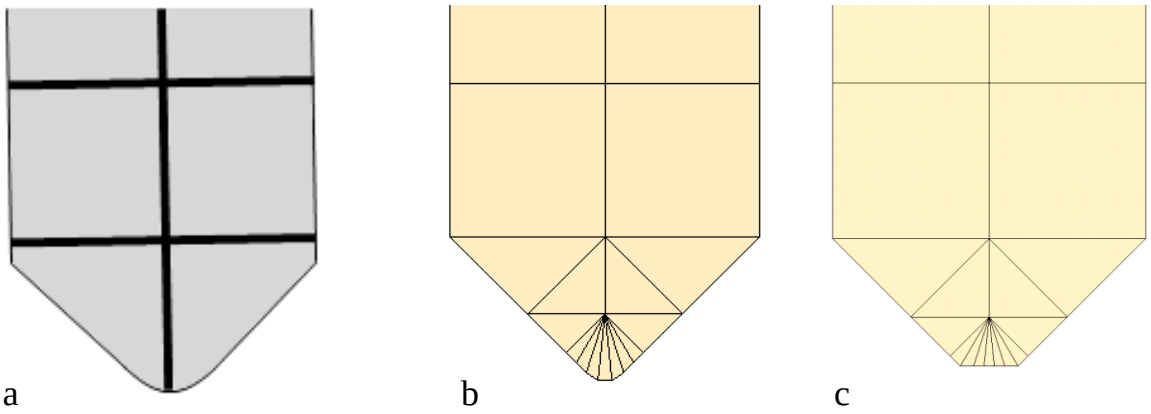

Figure 2-7. a) View of indenter from experimental setup (Zeinoddini et al. 2008), b) Indenter shape B, and c) Indenter shape C.

Table 2-2. Results from Different Indenter Shapes

P/Py (%)	Indenter	Dent (mm)	Bowing (mm)	Shortening (mm)
0	B	15.28	0.00	0.42
	C	15.42	0.02	0.45
27	B	18.37	0.69	1.48
	C	18.42	0.73	1.46

2.4.1.4 Simulation Results

Loads corresponding to a percentage of the squash load ($P_y=\pi Dt\sigma_y$=300 kN) are applied to the tubular specimen in the manner mentioned above and either the damage or failure of the specimen is recorded. Table 2-3 lists the values for the dent, bowing, and shortening of the specimen measured from the locations indicated in Figure 2-8. Figure 2-9 and Figure 2-10 illustrate the similarities between the experimental and numerical simulations, while Figure 2-11 shows that the axial load applied to the specimen, which decreases during the test due to shortening of the specimen, is well simulated by the finite element model. Table 2-3 also lists the final axial load as compared with the values provided from the experimental data.

Table 2-3. Comparison of Impact Test Results.

	Dent		Bowing		Shortening		Final Axial Load	
P/Py	Model	Exp.	Model	Exp.	Model	Exp.	Model	Exp.
0	17.90	15	0.96	1.8	0.56	0.3	-	-
0	17.90	16.28	0.96	2.2	0.56	0.4	-	-
25	21.70	21.5	1.80	3.0	1.68	-	0.24	-
27	21.94	22	1.94	3.2	1.78	0.8	0.26	0.26
50	27.57	25.3	4.49	5.6	3.27	2.3	0.49	0.44
60	34.12	28.4	7.74	9.3	7.73	3.1	0.57	0.52
62	38.00	30.1	10.45	10.4	9.37	3.4	0.58	-
65	Specimen failed in experiment and also in simulation							
70	Specimen failed in experiment and also in simulation							
72	Specimen failed in experiment and also in simulation							

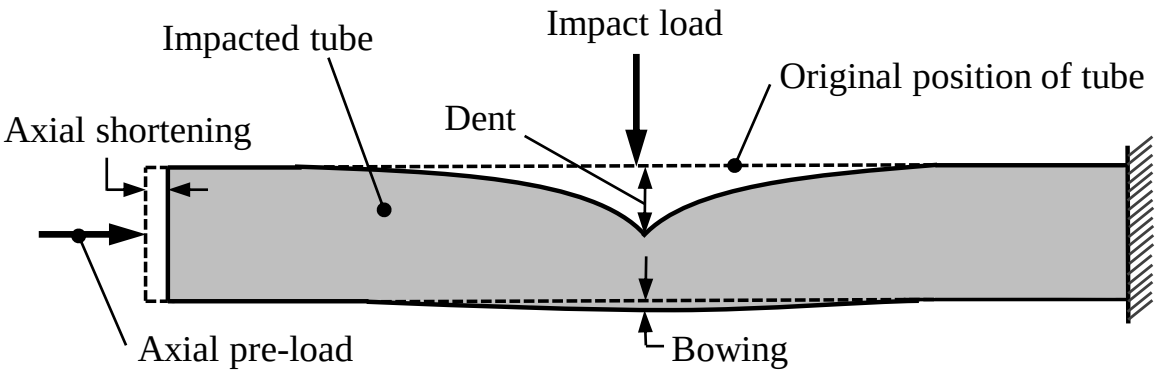

Figure 2-8. Schematic view of an impacted tube and the resulting dent, bowing, and axial shortening (Zeinoddini et al. 2002).

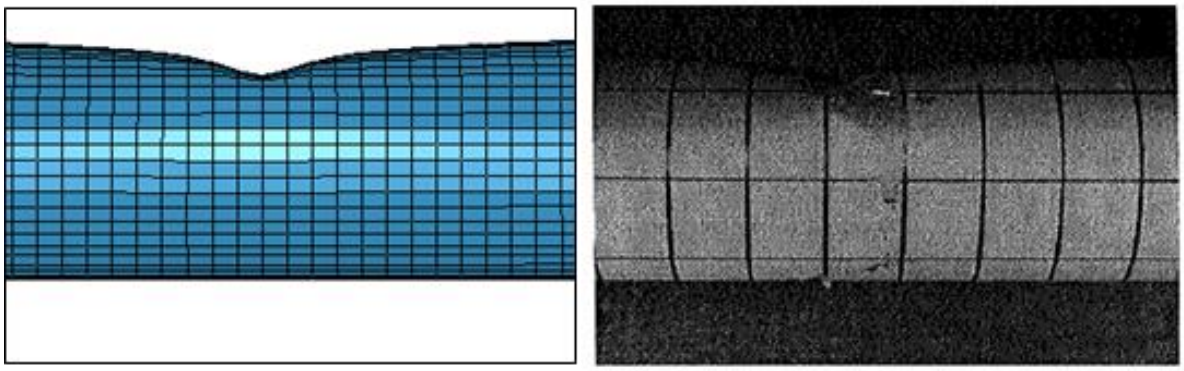

Figure 2-9. Post-impact view of a specimen with no axial pre-loading from experiment (right) and simulation (left) (Zeinnddini et al. 2008).

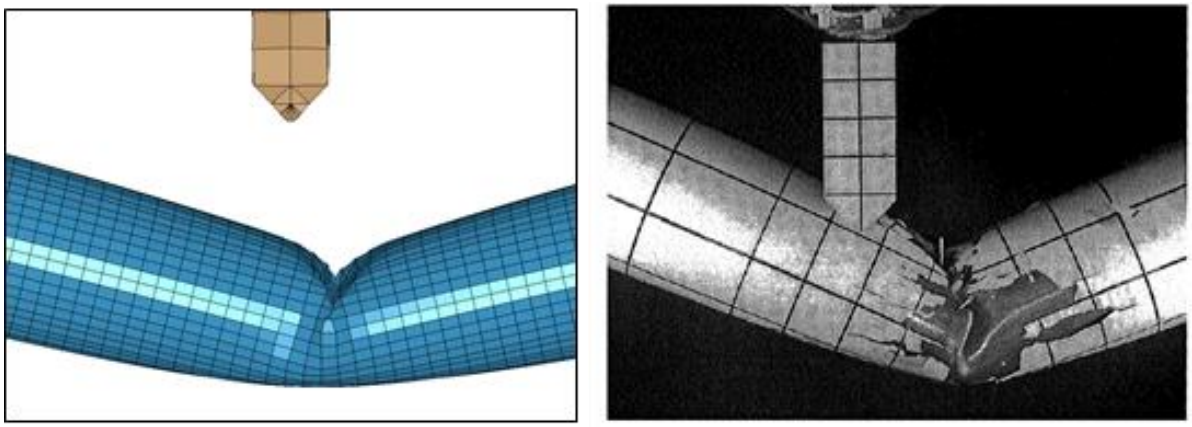

Figure 2-10. Post-impact view of a specimen with 70% axial pre-loading from experiment (right) and simulation (left) (Zeinoddini et al. 2008).

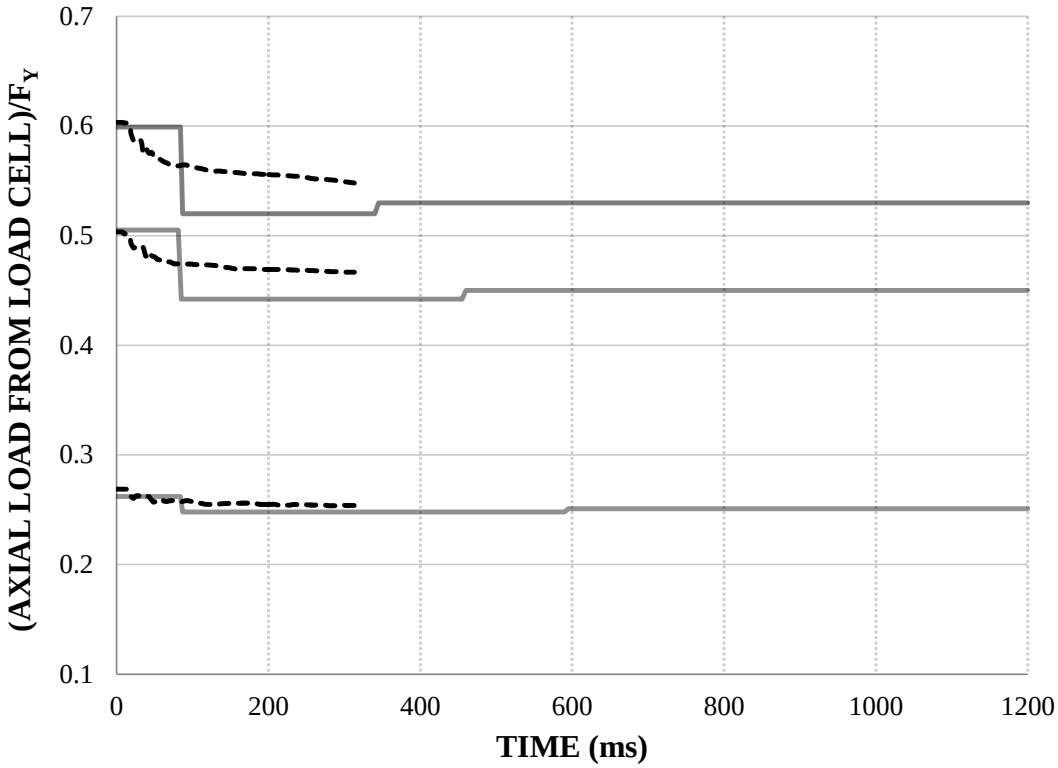

Figure 2-11. Comparison of experimental (solid lines) and numerical (dashed lines) time histories of axial load (Zeinoddini et al. 2002).

While some discrepancies exist, the values from the simulation are generally deemed to match reasonably well with the experimental values, especially at lower load levels. Discrepancies between the simulation and experimental data are attributed to: 1) the fact that the boundary conditions are over constrained in the numerical model, e.g. full rotational fixation is assumed at the ends, but that is likely not the case in the experiments; 2) experimental scatter; and 3) differences in the assumption of imperfection values and distribution. As the loads approach those that cause failure of the tube, the numerical values become less accurate. However, despite the less accurate values at higher load levels, the model captured failure instability at 65% pre-loading, unlike the numerical model created by Zeinoddini et al. (1999), which was unable to do so. Specifically, the proposed model fails at the 65%, 70%, and 72% loadings which is in accord with the failures that occurred in the experimental setup.

2.5 PARAMETRIC STUDY USING VARIATIONAL APPROACH

A parametric study is performed using the variational approach to determine the effect that local flange damage has on the axial capacity of a column. The various simulation cases performed in the parametric study are referred to in the following manner:

W14x120-X-LY-WZ

Where X designates the location of damage as either Center (C) or End (E), Y indicates the amount of damage along the length as a percentage ranging from 6 (%) to 50 (%), which are lower and upper bounds of the amount of damage considered, and Z is the amount of an individual flange removed as a percentage ranging from 33 (%) to 100 (%). For example, W14x120-E-L6-W100 implies a column with end damage that extends 6% along the column and entails removal of the entire flange along that length.

2.5.1 Location of Damage

Flanges are removed from both the center and end segments of the W14x120 column to assess the effect of the location of damage. The comparison shown in Figure 2-12 indicates that damage to the center of the column is more detrimental to the resulting axial resistance with decreasing significance as the length of the damage increases. The percent difference of the axial capacities in the two different locations at the same length of damage ranges from 7-28%. This indicates that the location of the damage (end or center) is slightly more influential in cases where there is less damage along the length.

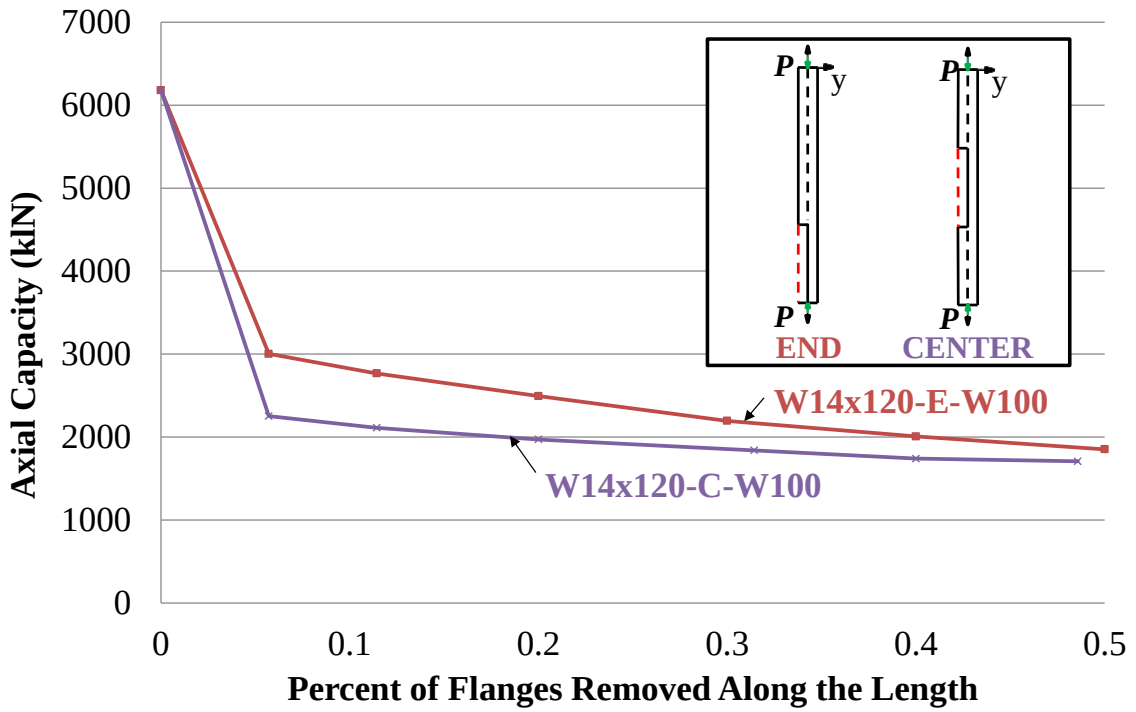

Figure 2-12. Relationship between axial capacity and location of damaged column segment.

2.5.2 Initial Imperfection

The importance of the initial imperfection of the W14x120 column is also considered. As expected, the axial capacity at all damage levels decreases as the initial imperfection increases, as shown in Figure 2-13. Moreover, the general trend of axial capacity versus length of damage remains the same. Clearly, the amount of initial imperfection plays an important role in overall column axial resistance, but the general trend as damage length increases is insensitive to its value.

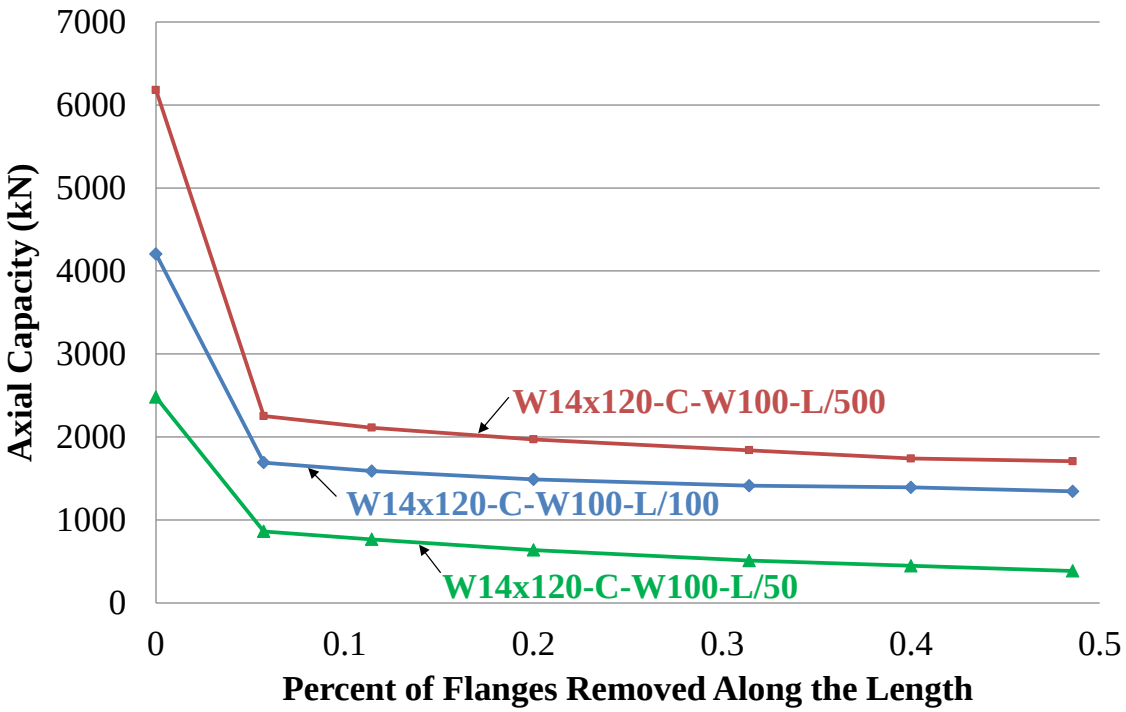

Figure 2-13. Relationship between axial capacity and initial imperfection.

2.5.3 Assessment

The simulation results from both of the above parameters show that axial load carrying capacity of the W14x120 column drops sharply when the flanges are removed. The drop in capacity increases as more of the flanges is removed along the length; however, the effect is mild. This observation implies that, for the W14 section, any interruption of the load path by damage to the flange is more influential than the length of damage along the column.

2.5.4 Partial Flange Removal

The above observations are based on simulations where the entire flange is removed along the assumed damaged length. The effect of partial flange removal within the cross-section along this length is studied to determine the effect of the amount of damage within the cross section. Table 2-4 shows the percentages of the damaged column capacity with respect to the undamaged

column axial capacity. The reduction between the axial capacity of the W14x120-E-W100 and W14x120-E-W33 cases increases slightly as the amount of damage along the length increases as seen in the fourth column of Table 2-4. This trend is also evident for the W14x120-C cases. The differences, which are around half as seen in Table 2-4, indicate that the amount of damage in the cross section has a significant effect on the reduction of the axial capacity, as expected. However, while there is still a sharp drop when flanges are removed as seen in Figure 2-14, the severity of this drop is heavily influenced by the amount of damage within the cross-section.

Table 2-4. Removal of Flange within Cross-Section.

Flange Removal Along Length (%)	W14x120-E			W14x120-C		
	Axial Capacity (%)		%	Axial Capacity (%)		%
	W33[a]	W100[a]	Reduction[b]	W33[a]	W100[a]	Reduction[b]
L6	94.6	47.3	50.0	74.4	36.3	51.2
L10	88.2	43.6	50.6	70.1	33.5	52.2
L20	81.4	39.3	51.7	66.5	31.1	53.2
L30	74.5	34.6	53.5	63.0	29.0	54.0
L40	68.9	31.6	54.1	61.3	27.4	55.3
L50	64.6	29.2	54.8	59.9	26.9	55.1

[a]WZ indicates the percentage (Z) of flange removed within the cross-section.
[b]Difference between W33 and W100 axial capacities divided by W33 axial capacity.

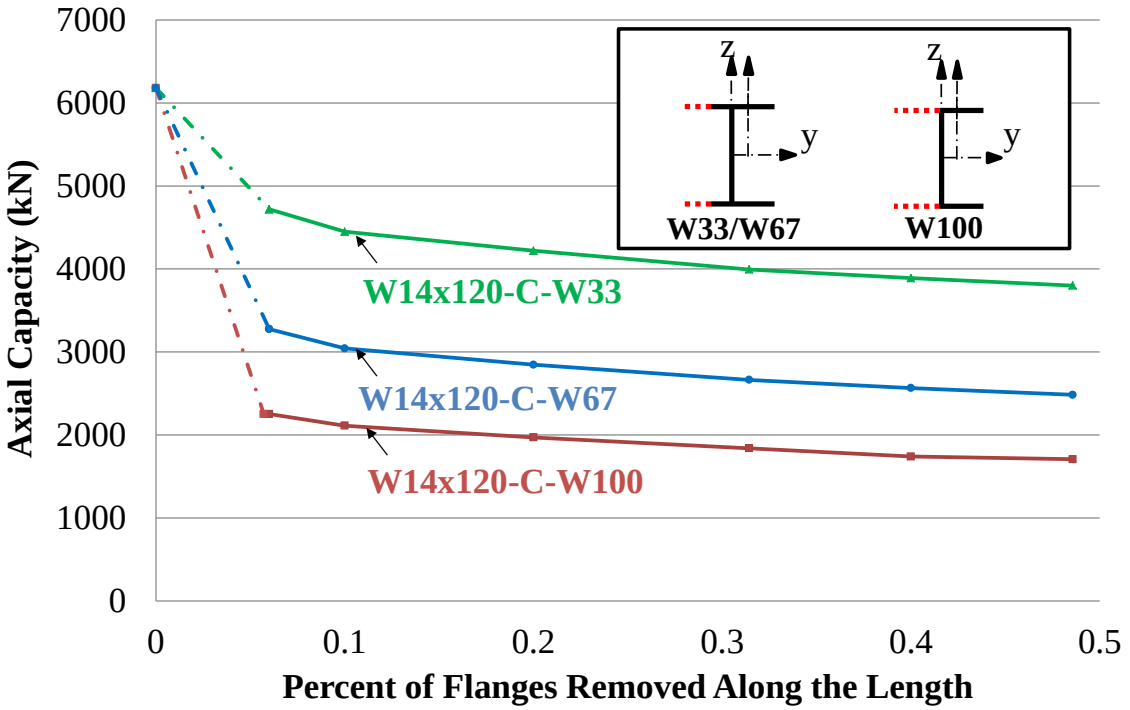

Figure 2-14. Relationship between axial capacity and damage extent within cross-section.

2.5.5 Asymmetric Damage

The effect of asymmetric damage is also investigated for the W14x120 column by removing only one of the flanges seen damaged in the cross-sections of Figure 2-1. Variations in the amount of damage along the length and within the cross-section previously studied in the symmetric case are investigated as shown in Figure 2-15. Despite the asymmetric damage, global buckling remains the predominant mode of failure observed in each of the finite element models with varying amounts of damage along the length of the column. The difference between the axial capacity of a column with 1/3 of the flange removed and the full flange removed remains on average 29% for the different cases of amount of flange removal along the length. This value is slightly more than half of the lowest percent difference seen in the symmetric case and implies a less significant effect on the reduction in axial capacity. There is also only an 11% difference between the axial capacity of a column with 6% of the flanges removed along the length and a

column with 50% of the flanges removed along the length. These values again support previous observations about the significant effect of interruption of the load path.

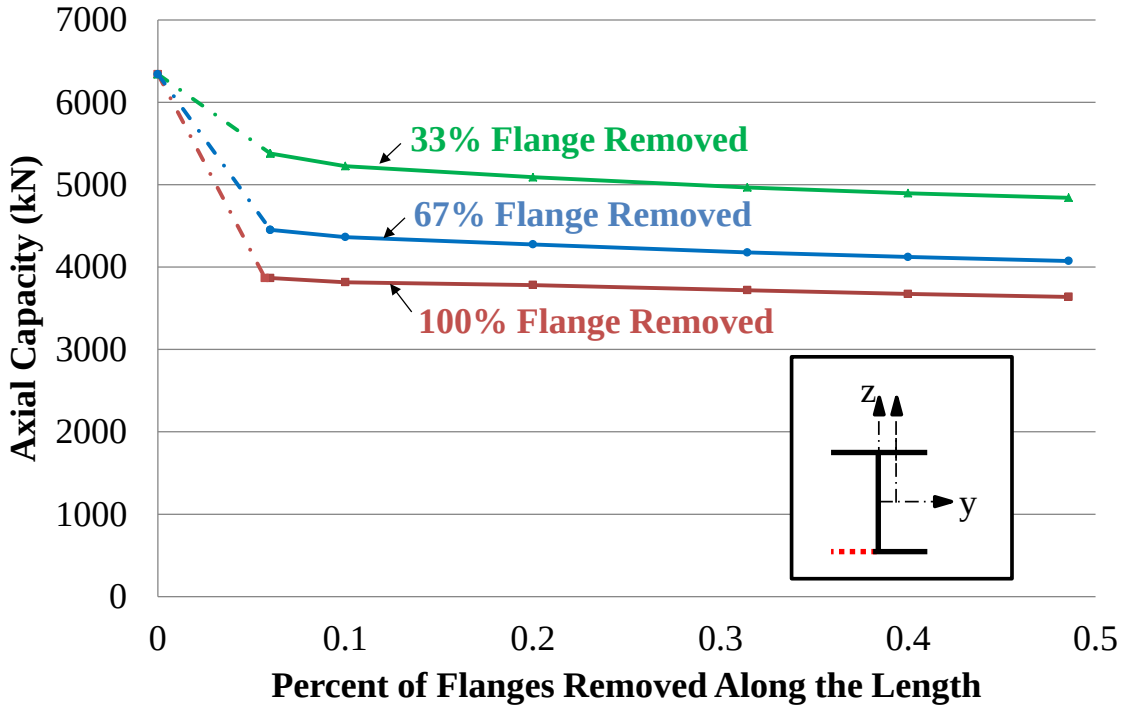

Figure 2-15. Relationship between axial capacity and damage extent within cross-section for aysmmetric damage case.

2.5.6 W30x124 Modeling

Simulations show that removal of elements from the center of the column results in behavior that is similar to the W14x120 section. In particular, there is a sharp initial drop followed by a mild decrease in axial capacity as more elements are removed along the length of the column. However, removing elements from the end segment of the column yields a more gradual decrease in the axial capacity than seen for the W14x120 column as depicted in Figure 2-16.

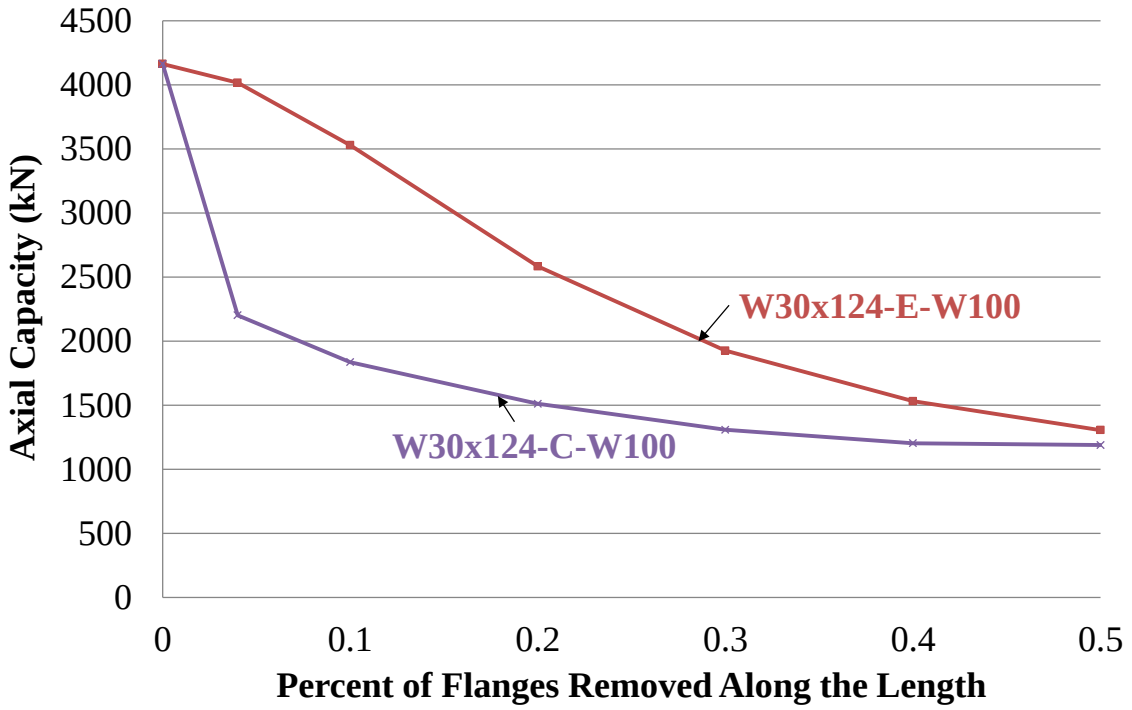

Figure 2-16. Relationship between axial capacity and damage extent within cross-section.

Viewing the simulations of both the W14 and W30 column in the case where 6% of the elements were removed along the length shows that there are substantial differences in how the columns behave when loaded. In the W14 case, a plastic hinge forms at the location of the damage, whether it is centered or at the end. However, in the W30 case, a plastic hinge forms at the center of the column regardless of the location of the damage. The reason for the differences in behavior stems from differences in the geometry between the two cross-sections. The W14 section has larger flanges (b_f = 14.7 in) than the W30 section (b_f = 10.5 in). Hence removal of flanges in the W14 section 1) weakens the axial capacity of the section considerably more and 2) creates a substantially greater eccentricity than in the W30 case. These effects promote an unfavorable axial/flexural interaction in the damaged W14 section when the damage occurs at the member's end, leading to early formation of a plastic hinge at the member end. In contrast,

the W30 section's ends do not yield despite the damage, leaving the member to be dominated by behavior at the member's center, where the moment due to the initial imperfection is greatest.

These results suggest that the location of the localized damage can play an influential role in certain types of cross-sections, especially those with more square aspect ratios, which are popular for gravity columns.

2.5.7 Comparison of Variational and FEM Results

The finite element solution is plotted versus the analytical solution shown in Figure 2-2 for the case of W14x120-C-L20-W100. The numerical and analytical curves appear to match at the beginning and end, but deviate in the middle. However, the peak load predicted by the analytical model is a reasonable approximation of the numerical data as shown in Figure 2-17 with the percent errors for each case given in Table 2-5 and Table 2-6. The W14x120-C-L6-W100 and W30x124-C-L20-W100 cases present the largest percent errors with the maximum being 15.1%. In the W14x120 cases, the analytical solution is more conservative than the FEM whereas the opposite is true for the W30x124 column in every case but the smallest length of damage.

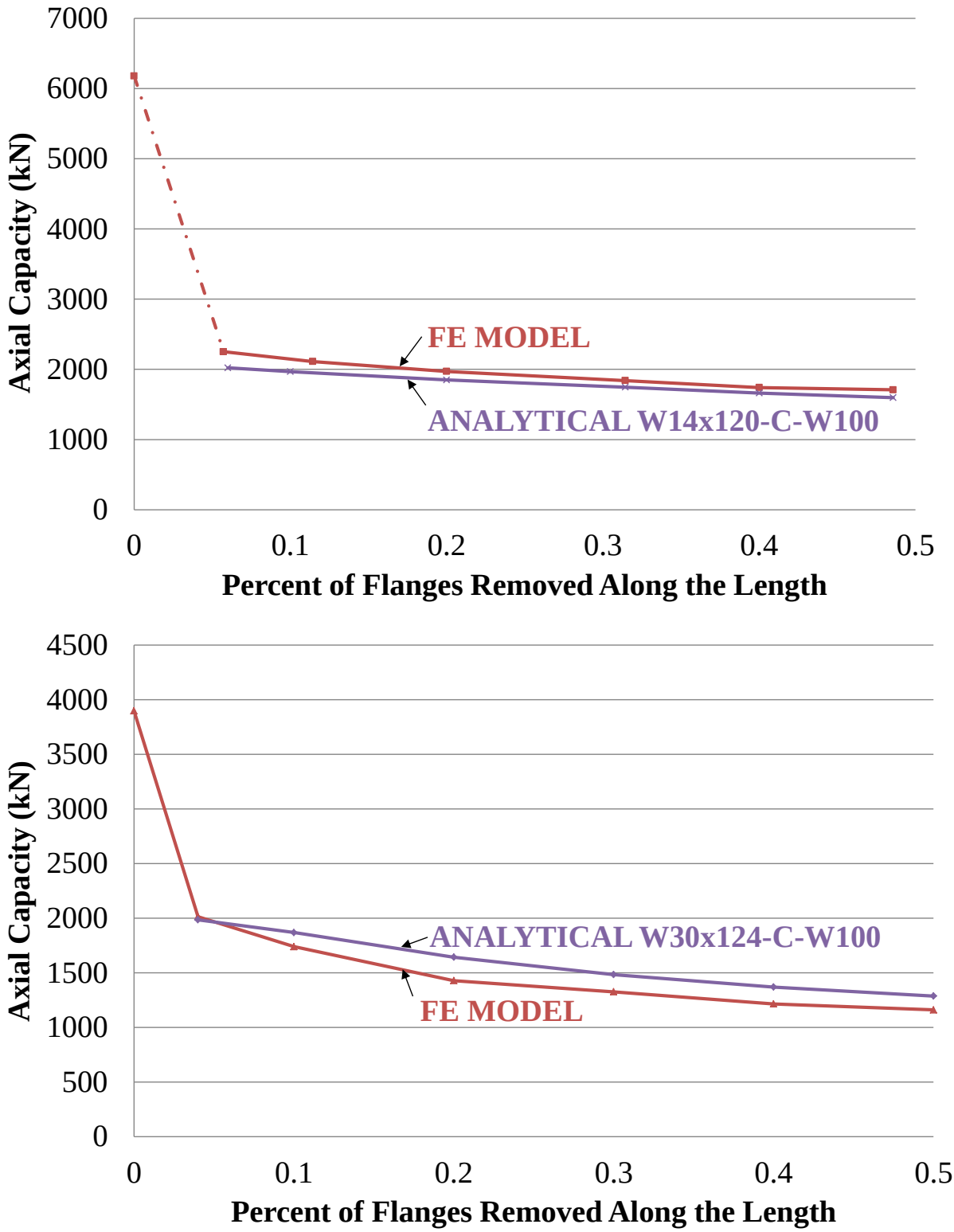

Figure 2-17. Relationship between axial capacity and length of damaged center column segment for a) W14x120-C-W100 and b) W30x124-C-W100

Table 2-5. W14x120-C-100

Flange Removed Along Length (%)	R-R	FE	Percent Difference[c] (%)
L6	2022	2300	12.1
L10	1968	2122	7.3
L20	1849	1970	6.2
L30	1746	1840	5.1
L40	1663	1740	4.4
L50	1597	1708	6.5

[c]Difference of FE and R-R values divided by FE value.

Table 2-6. W30x124-C-W100

Flange Removed Along Length (%)	R-R	FE	Percent Difference[d] (%)
6	1985	2013	1.4
10	1864	1740	-7.2
20	1644	1428	-15.1
30	1484	1325	-12.0
40	1366	1214	-12.4
50	1286	1160	-10.9

[d]Difference of FE and R-R values divided by FE value.

2.6 MODELING FOR DESIGN

As previously noted, Figure 2-2 suggests that the peak finite element solution is reasonably close to the intersection of the Rayleigh-Ritz solution ('stability' curve in Figure 2-2) and the plastic strength solution ('strength' curve in Figure 2-2). Of the two curves (stability and strength), the former is not easy to compute in a design office setting. However, a simplified design-oriented model (henceforth designated DM) can be constructed to facilitate the design computations. To achieve this objective, a model resembling Figure 2-1 is created using linear elastic beam-column elements and a geometrically nonlinear analysis is conducted under increasing axial loading. Such an analysis is within the reach of most structural analysis software used in design

offices. Figure 2-18 shows that the difference between the Rayleigh-Ritz solution and the simplified model is small. Compared to the finite element models as shown in Table 2-7 and Table 2-8, it is clear that DM is reasonably accurate in providing a similar approximation to the analytical solution obtained using the Rayleigh-Ritz method. This observation indicates that the simplified model is useful in providing a quick estimate of the reduced axial capacity due to localized column damage for cross-sections similar to the ones studied herein. Additional studies covering a broad set of cross-sections are needed to generalize this observation.

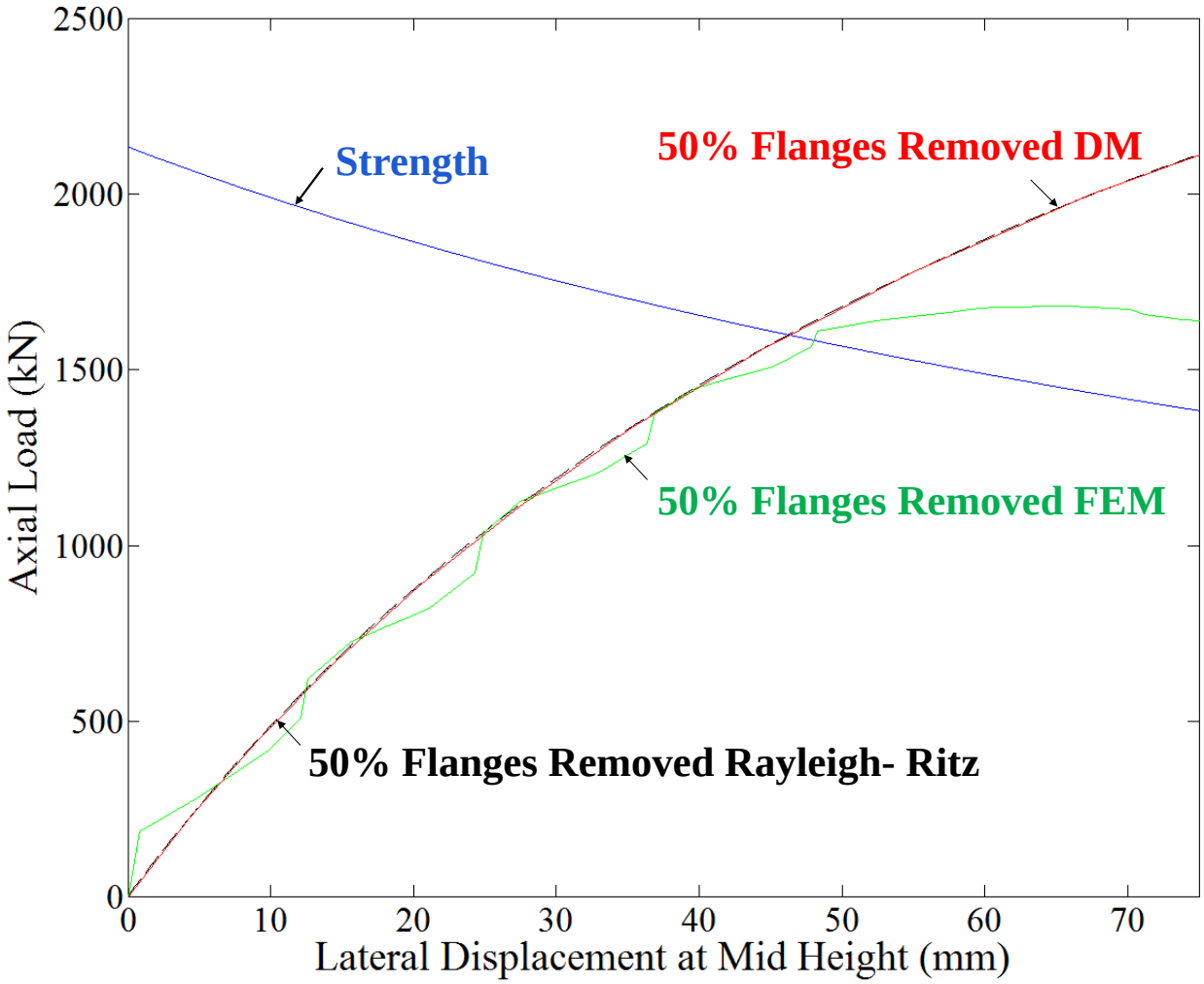

Figure 2-18. Comparison of design model, Rayleigh-Ritz, and FE models

Table 2-7. W14x120-C-W100 DM Comparison with FE and R-R Models

	DM	FEM	% Difference[e]	DM	R-R	% Difference[f]
L6	2014	2251	-10.5	2014	2022	-0.4
L10	1930	2111	-8.6	1930	1968	-1.9
L20	1825	1945	-6.2	1825	1849	-1.3
L30	1713	1840	-6.9	1713	1746	-1.9
L40	1649	1740	-5.2	1649	1663	-0.8
L50	1599	1708	-6.4	1599	1597	0.2

[e]Difference of DM and FE values divided by FE value.
[f]Difference of DM and R-R value divided by R-R value.

Table 2-8. W30x124-C-W100 DM Comparison with FE and R-R Models

	DM	FE	% Difference[g]	DM	R-R	% Difference[h]
L6	2033	2014	1.0	2033	1985	2.4
L10	1837	1740	5.6	1837	1864	-1.5
L20	1610	1428	12.7	1610	1644	-2.1
L30	1454	1325	9.7	1454	1484	-2.0
L40	1352	1215	11.3	1352	1336	1.2
L50	1275	1160	9.9	1275	1286	-0.9

[g]Difference of DM and FE values divided by FE value.
[h]Difference of DM and R-R value divided by R-R value.

2.7 PARAMETRIC STUDY USING EQUILIBRIUM APPROACH

Extensive simulations were conducted using the equilibrium approach outlined in Yossef et al. (2014) to explore the effect of various influential parameters on column response. The parameters considered include column cross-section, length of damaged segment, damage location, amount of flanges removed in the damaged segment, column slenderness and initial imperfection. One hundred seventy two variations were analyzed to fully investigate the effect of these parameters and develop an empirical equation for quickly determining column capacity. Table 2-9 shows a list of the selected parameters.

Table 2-9. List of studied parameters (Yossef et al. 2014).

Column Cross Section	a_0 - Initial imperfection	L - Column Length (m)	l_2 - Length of Damaged Segment	Amount of Flange Damage (b is flange width)	Damage Location
W24x 176	L/500	3.50	$L/3$	0.1b, 0.2b, 0.3b, 0.4b, 0.5b	Center Segment
		5.18			
		7.00			
W14x120	L/500	5.18	0.06L, 0.1L,0.2L, 0.3L, 0.4L,0.5L	0.5b	Center Segment
W14x120	L /50, L/100, L/250, 0.006L	5.18	L/3	0.1b, 0.2b, 0.3b, 0.4b, 0.5b	Center Segment
W24x 176					
W30x 124					
W36x 262					
W40x 267					
W30x 124	L/500	3.50	L/3	0.1b, 0.2b, 0.3b, 0.4b, 0.5b	Center Segment
		5.18			
		7.00			
		5.18	0.06L, 0.1L,0.2L, 0.3L, 0.4L,0.5L	0.5b	
W14x120	L/500	5.18	L/3	0.5b	From bottom, starting at 0.1L, 0.2L, 0.3L, 0.4L, 0.5L, 0.6L
W24x 176					
W30x 124					
W36x 262					
W40x 267					

2.7.1 Comparison Between Variational and Equilibrium Approaches

The comparisons are shown in Figure 2-19 and Figure 2-20 for the W14x120 and W30 x124 columns, respectively. The plots are for columns for which half of the flange is removed along the central segment and the central segment length varies from 0 (no damage) to half the column length. It is clear that the variational analytical solution matches well with both the finite element and Rayleigh-Ritz results.

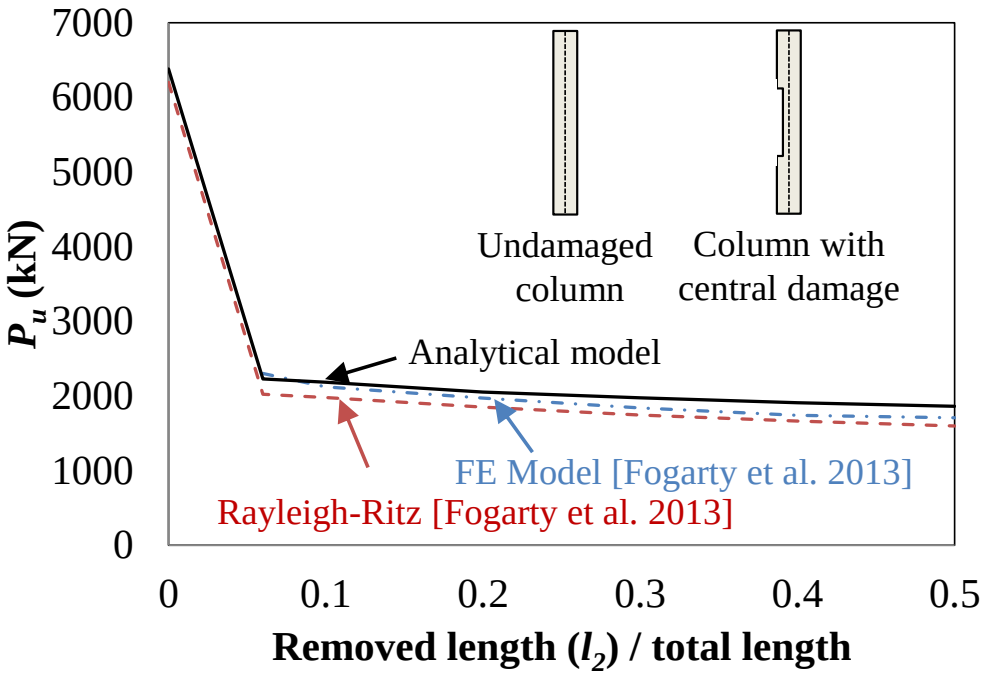

Figure 2-19. Comparison between analytical, FE model, and Rayleigh-Ritz solutions (W14x120, L = 5.17 m, $l_1 = l_2 = l_3$, f_y = 345 MPa, a_0/L = 0.002)

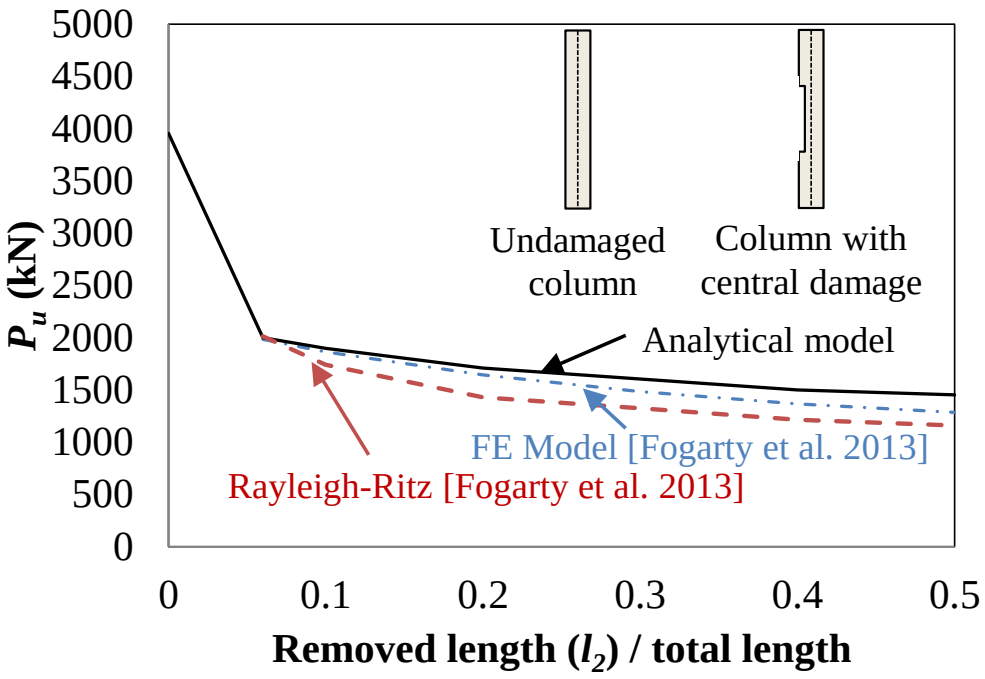

Figure 2-20. Comparison between analytical, FE model, and Rayleigh-Ritz solutions (W30x124, L = 5.17 m, $l_1 = l_2 = l_3$, f_y = 345 MPa, a_0/L = 0.002)

2.8 EMPIRICAL MODEL

2.8.1 Best Fit Equation

All the parameters studied in Table 2-9 are plotted in aggregate in Figure 2-21, which shows the relationship between P_{ud}/P_u & A_d/A. The data covers all of the parameters considered in the equilibrium approach, i.e. different damaged segment lengths, damage locations, amount of damage in the cross-section, column slenderness, and initial imperfections. The results remain in a narrow band in the figure suggesting that the ratio of the damaged to undamaged column cross-sectional area, A_d/A, is an important parameter for predicating the residual load carrying capacity of a steel column with symmetrically damaged flanges. The best fit curve in Figure 2-21 can be represented as:

$$P_{ud}/P_u = 4.64\,(A_d/A)^2 - 5.80(A_d/A) + 2.16 \qquad \text{2-14}$$

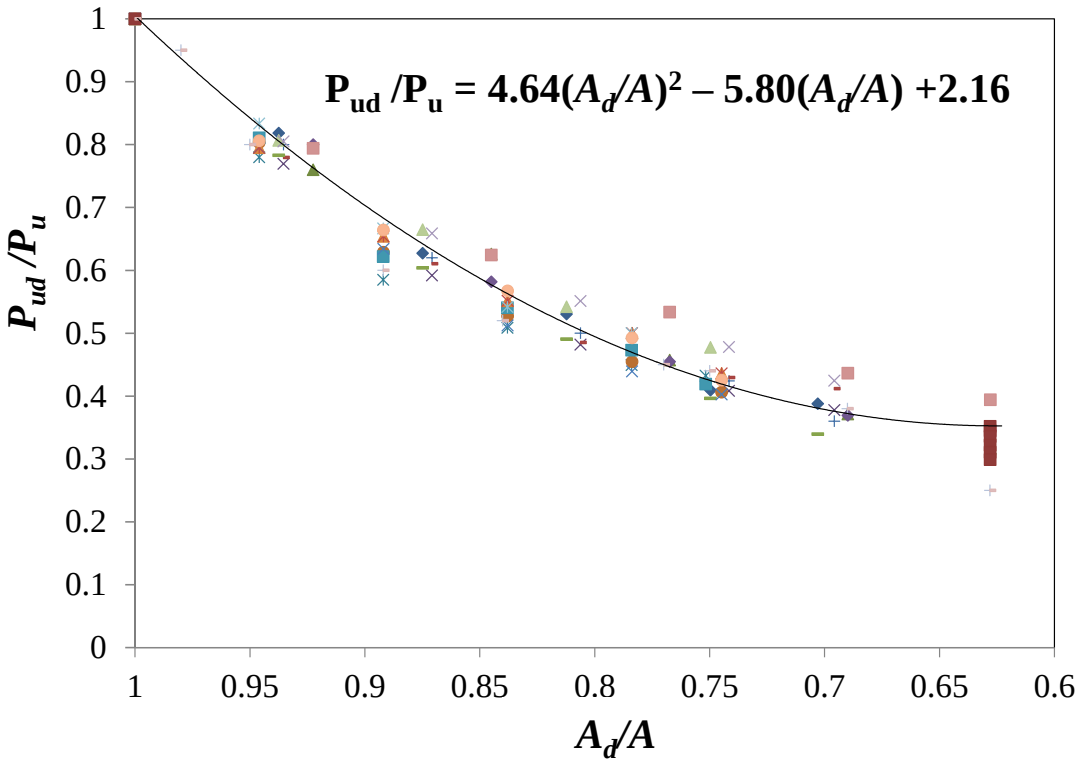

Figure 2-21. Relationship between maximum load carrying capacity versus A_d/A

When the column has not suffered a permanent global imperfection due to the damage initiating event, then P_u can be computed using code equations. Otherwise, it can be computed as the intersection of the stability curve and the plastic strength solution as shown in Figure 2-4. Of the two curves (stability and strength), the former is not easy to compute and the design model presented above provides a simplified way to facilitate the calculation. This alternative approach is within the reach of most structural analysis software used in design offices and can be used to compute P_u for a given initial imperfection.

2.8.2 Validation of Empirical Model

To show that Equation 2-14 yields reasonable answers, its results are compared to data from the Rayleigh-Ritz method and detailed finite element models presented above. Table 2-10 shows the column capacity based on these three methods for a column with L=530 cm, f_y =345 MPa, a_0 =0.002L, and a centrally damaged segment of 0.3L. Differences of 2.3% to 8.4% between the proposed equation and available data provide confidence that Equation 2-14 is yielding realistic results.

Table 2-10. Comparison between Equation 2-14, R-R Method, and FE

Damaged Column	Equation 2-14	Results from Rayleigh-Ritz and Computational Work			
	P_{ud} (kN)	Analytical	Difference	F.E	Difference
W14x120	1787	1746	2.3%	1840	3%
W30x124	1447	1484	2.5%	1325	8.4%

Additional finite element simulations using models similar to those developed previously were created to provide a comprehensive comparison to Equation 2-14. In the previous study, detailed finite element models of W14x120 and W30x124 columns with various amounts of damage both along the length and within the cross-section were modeled. These columns were validated using

similar modeling techniques to those employed in creating the finite element models to replicate the results from an experimental study by Zeinoddini et al. (2002).

The additional columns are modeled in this study using fully integrated Belytschko-Wong-Chiang shell elements. Rigid plate caps are attached at either end to distribute the applied loads over the entire cross section without causing local deformation. As shown in Figure 2-22, rotation around the web is permitted at the lower end, while rotation around the web and vertical (z) translation is permitted at the top end. The geometry is modified to include an initial imperfection that assumes a sinusoidal shape with a maximum deflection of L/500 at mid-height. This maximum imperfection is greater than the L/1000 assumed in AISC (2006) to indirectly account for residual stresses, which are not included in the simulation.

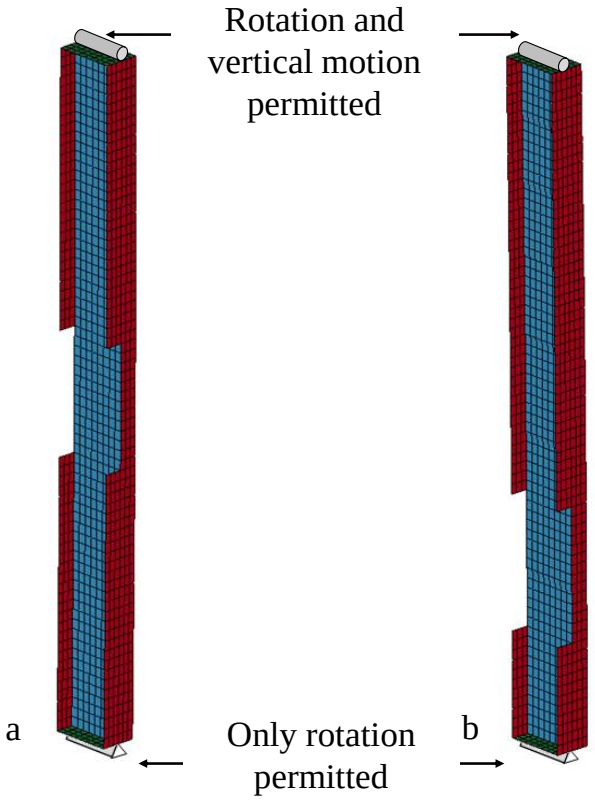

Figure 2-22. Finite element models of a W18x119 column with 0.2*L* damage at a) center (0.5*L*) and b) quarter (0.25*L*) height

The additional column sections that are modeled, as shown in Figure 2-22, include W18x119, W21x111, W27x178, W33x201, and W36x194 with a centrally damaged segment of 0.2L or 0.34L. All of these columns were not used in the calibration of Equation 2-14 to ensure that this is a true validation exercise. To investigate the location of damage, flanges are removed at the middle of the column and at quarter height. The comparison of the data is summarized in Table 2-11 and Table 2-12, respectively, and collectively plotted against Equation 2-14 in Figure 2-23. The naming scheme in Figure 2-23 signifies the characteristics of the case considered, e.g. Quarter-0.2L-W66 means that the center of the damaged segment is located at quarter length from the bottom, is 0.2L long and that 66% of the flange is removed. Figure 2-22 also provides insight into the naming scheme.

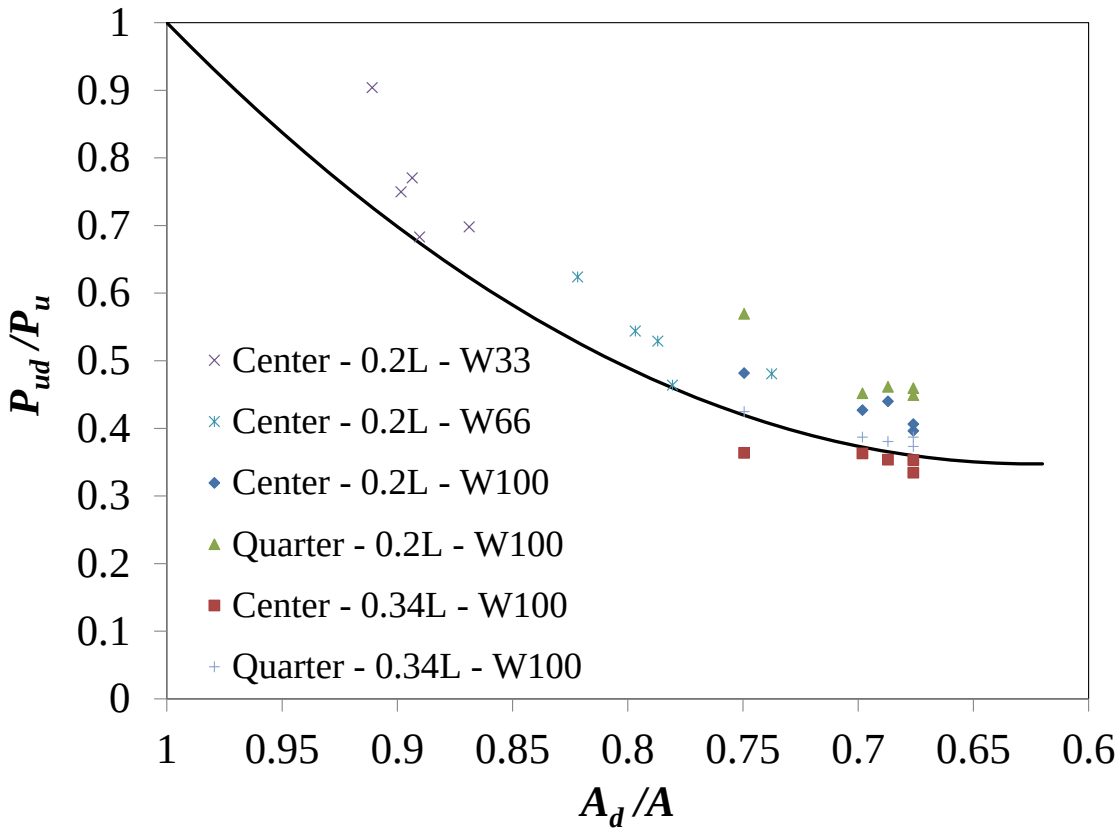

Figure 2-23. Comparison between Equation 2-14 and finite element results

Table 2-11. Comparison of Equation 2-14 and FE models with changes in A_d/A

Column	Equation 2-14 P_{ud} (kN)	FEM Center W33*	Error	Equation 2-14 P_{ud} (kN)	FEM Center W66**	Error
W18x119	3116	3490	11%	2031	2403	15%
W21x111	3337	3382	1.3%	2277	2296	0.8%
W27x178	5833	6590	11%	4013	4525	11%
W33x201	6778	7322	7.4%	4728	5311	11%
W36x194	5330	6630	20%	3866	4575	16%

*Solution computed from FE model for damage in column center (0.2L length) and 1/3 of the flange removed
**Solution computed from FE model for damage in column center (0.2L length) and 2/3 of the flange removed.

Table 2-12. Comparison of Equation 2-14 and FE models with different locations of damage

Column	Equation 2-14 P_{ud} (kN)	FEM Center*	Error	FEM Quarter**	Error
W18x119	1798	2032	12%	2297	22%
W21x111	1780	1962	9.0%	2224	20%
W27x178	3126	3764	17%	3947	21%
W33x201	3635	4167	13%	4411	18%
W36x194	3076	3534	13%	4177	26%

* Solution computed from FE model for damage in column center (0.2L length), full flange removed
** Solution computed from FE model for damage centered at quarter length from bottom (0.2L length), full flange removed.

With errors ranging from 0.8 to 20 percent (Table 2-11) and averaging 10.5%, the capacities of columns with various amounts of damage within the cross-section in the center are reasonably predicted by Equation 2-14. Errors for the simulations where the location is not at the center of the column (Table 2-12) are higher and range from 9 to 26 percent (with an average of 17.1%) for damage at quarter height.

2.8.3 Application and Limitations of Best Fit Equation

Equation 2-14 is intended to estimate the residual load-carrying capacity for columns with symmetric, localized flange damage for W-shape columns buckling about their weak axis for a pin-pin situation. As shown above, the results become more conservative when the damage occurs away from the center segment. Common techniques used for adjusting strength as a function of boundary conditions can be employed to account for the site-assessed boundary conditions as needed, although selection of a pin-pin condition is conservative for a braced structure and is the only boundary condition utilized in this study.

Common sense should be exercised when selecting the variables to go into the equation. For example the engineer assessing damage should conservatively estimate how much of the flange is "damaged" and therefore no longer effective. Clearly this is a subjective process and its accuracy depends on the competence and experience of the engineer.

When the initial imperfection of the column has not been adversely affected by the damage incident, reasonable values for a_o are $L/500$, which accounts for the $L/1000$ tolerance specified in AISC and another $L/1000$ to account for residual stresses. When the damaging event causes an out of straightness to occur, the maximum measured value can be used instead.

Equation 2-14 should not be applied to a column that is expected to buckle about its strong axis or in an unbraced structure. Also, the equation conservatively assumes that symmetric flange damage occurs and will yield conservative results when the damage is localized to only one flange. Further research is needed to address situations beyond the conditions for which Equation 2-14 was generated.

2.9 SUMMARY AND CONCLUSIONS

Numerical and analytical solutions were presented for the case of a steel column with localized flange damage. The first analytical model was developed using a variational scheme and the results were compared to data from detailed finite element models that were validated through comparisons with experimental results. Results from an analytical approach based on the governing differential equation for buckling of a column with a non-uniform cross-section were compared with the values obtained using a variational analytical method as well as with detailed finite element models validated using available experimental data. In spite of the limiting assumptions made in developing the analytical models, the results are valuable because they shed light on the main variables that influence the problem.

Results from the finite element model indicate that the axial capacities of the columns considered in this work are sensitive to localized flange damage, dropping 60% when a small part of the flange (6% along the length) is removed in the central portion of the column. The axisymmetric damage cases experienced the smallest reduction whereas the W14x120-C-W100 and W30x124-C-W100 cases experienced the largest reduction in axial resistance. While the various parameters investigated have different effects on the magnitude of the reduced axial capacity, they all exhibit the same overall trend of an initial sharp reduction followed by mild decrease with

increasing amounts of damage along the length for the W14x120 column. However, this trend was not seen in the W30x124-E cases implying that the aspect ratio of the column plays an important role in the rate at which the axial resistance reduces with respect to the amount of damage along the length of the column. A simplified design model was proposed to enable a practical approach for obtaining the stability curve and predicting the reduced axial capacity. Maximum errors of 2.4% between the DM and the variational analytical model and 12.7% between the DM and the detailed finite element model were obtained indicating that the design model provides a reasonable approximation of the reduced axial capacity for the types of cross-sections studied.

All three techniques correlated well and showed that compressive strength can be severely reduced in the presence of local flange damage. Most importantly, the capacity of the damaged column relative to its original capacity is primarily a function of the ratio of the cross-sectional area in the damaged segment to the area of the undamaged cross-section. The trend correlating these two ratios was insensitive to the type of cross-section considered indicating its general versatility for use in estimating the axial compressive capacity of flange-damaged columns.

An empirical equation was derived based on the results of the equilibrium-based parametric study. The format of the equation is chosen to be simple so that practicing engineers can use it to quickly approximate the capacity of a steel column that has undergone localized flange damage. The equation is shown to be reasonably accurate for the range of variables and cross-sections considered in this study. Further research is necessary to ensure that this equation is generally applicable.

CHAPTER 3

BEHAVIOR OF STEEL COLUMNS SUBJECTED TO COMBINED AXIAL AND CYCLIC LATERAL LOADING

3.1 GENERAL

This chapter presents an overview of the relevant literature and introduces the current seismic design guidelines. Detailed finite element models are then presented that were validated based on the limited available experimental data. An extensive parametric study is performed to determine the effect of various geometric parameters on the axial resistance of deep, slender sections. A simple-to-use design aid is presented as a supplement to current AISC seismic design guidelines.

3.2 LITERATURE REVIEW

Seismic loads can cause extreme deformation demands or forces on structural components and thus reduce the integrity and capacity of a structural system. Collapse of a structure under seismic loading is defined as the inability of the system to continue to support gravity loads during an earthquake. The loss of stiffness and strength in structural components can result in partial or total collapse of a structure during or after a severe seismic event (Zareian et al. 2010). The collapse of a structure during seismic events is typically classified as either sidesway or vertical. Significant P-delta effects resulting from a reduction in the load carrying capacity of the lateral load resisting structural components can lead to system instability and thus collapse in a sidesway manner (Takizawa and Jennings 1980). Vertical (progressive) collapse can result from

one or more gravity load bearing structural components failing and triggering adjacent component failure (Zareian et al. 2010), i.e. leading to progressive vertical collapse.

Modeling and predicting the collapse of structures under seismic loads is complex due to the uncertainty associated with ground motion and building model attributes as well as the complexity and computational effort required to run nonlinear dynamic analyses, especially up to and during collapse. Regardless of these challenges, many have expressed a need to further the state of knowledge regarding the limit state of collapse under seismic loads due to the severe consequences of partial or total failure. However, the majority of studies to date have focused on sidesway collapse (Lignos 2008), even though it is recognized that the loss of axial load carrying capacity of a column within a structure during a seismic event can lead to progressive vertical collapse.

Past research in progressive vertical collapse has focused primarily on the vulnerability of reinforced concrete columns (Moehle et al. 2002, Setzler and Sezen 2008, Wu et al. 2010). This was motivated by column failures in reinforced concrete structures built prior to modern seismic design guidelines. Column failure and subsequent pancake collapses of reinforced concrete buildings during seismic events have been attributed to the lack of ductile detailing in older structures (Wu et. al 2010). In contrast, much less research has been devoted to steel columns, and little is known about the degradation in axial capacity that they may suffer as a result of lateral seismic loading.

3.2.1 Computational Studies

Krishnan and Muto (2012) investigated the response of tall steel buildings subjected to severe seismic excitations. The results of their simulations indicate that a collapse mechanism occurs

when plastic hinges form at the top of all columns in an upper story and at the bottom of all columns in a lower story to create a "quasi-shear band (QSB)." When the overturning moment from the inertia of the upper block of stories overrides the capacity of the plasticized QSB, a sidesway collapse mechanism is initiated. The mechanism is then overtaken by gravity once the quasi shear band is destabilized by seismic waves imparting a velocity to the base stories in the opposite direction of the block of stories above the QSB. This collapse mode was predicted by Lignos et al. (2011) and observed in full scale 4-story steel moment frame shake table tests performed by Suita et al. (2008). However, Krishnan and Muto note that many numerical models of steel strutcures do not include the effect of local flange buckling even though it may play a critical role in a structure subjected to a multi-cycle seismic excitation.

Newell and Uang (2006) computationally investigated the behavior of three W27 sections and noticed severe local flange and web buckling. Significant strength degradation was noticed as a result of the local buckling and several of their models were unable to complete the applied loading sequence. The deep columns were unable to withstand the combination of a high axial load and lateral cyclic load that are possible under an extreme seismic event. The rapid degredation seen in this numerical study due local buckling was also observed by Lignos and Krawinkler (2011) in their database for deterioration of steel component modeling that focused on wide-flanged steel beams.

Elkady and Lignos (2014) also computationally investigated deeper sections under a combined axial and cyclic loading scheme, focusing on the axial shortening and pre-capping rotations of typical first-story interior columns. They recommend a reduction in the current AISC high ductility compactness limits for sections used in lower stories of special moment systems, but

note that their results are dependent on the applied loading and boundary conditions and do not consider different member lengths.

3.2.2 Experimental Studies

Testing specimens or subassemblages all the way up to collapse is dangerous and expensive, which has limited experimental research in this area. With the objective of providing experimental data for calibration of inelastic, cyclic models, Vian and Bruneau (2001, 2003) conducted shake table tests on 15 four-column frame specimens (SDOF) up to collapse. Their experiment is meant to be applicable to both steel and concrete structures that generally exhibit a bilinear behavior. They concluded that the stability coefficient had the most significant effect on the probability of collapse of the frame. As the stability factor increased, the level of ductility, sustainable drift, and spectral acceleration withstood by the system decreased.

While columns are often the most critical components of structures susceptible to damage under seismic loading, little research has focused on the behavior of steel columns subject to these loading scenarios. Lamarche and Tremblay (2011) performed full scale compression buckling tests on steel columns subjected to monotonically and cyclically applied concentric as well as eccentric axial loading. The experimental results were then compared with a model created in the OpenSees framework using nonlinear beam-column elements with cross-section fiber discretization. Lamarche and Tremblay determined that inclusion of residual stresses can lead to reductions of up to 30% of the compressive strength of the steel columns and can potentially make the difference as to whether or not a column will buckle under seismic loading. The authors concluded that local buckling in centrally loaded columns did not significantly impact the column post-buckling axial strength based on the quasi-static cyclic test of a W12x87

column. However, local flange buckling did occur before global buckling when the column had an eccentric axial load in the experimental test. The axial capacity predicted by the numerical models in the eccentric loading case was higher than that seen in the experimental column most likely due to the lack of inclusion of local buckling effects in the OpenSees framework.

Lignos and Krawinkler (2009) analyzed experimental data of 115 tubular steel beam-column members subjected to combined axial compression and bending. The major observation was the rapid deterioration of column strength for depth to thickness ratios exceeding 30 combined with high axial load ratios exceeding 30% of the nominal capacity. This conclusion was also observed in the four-story full-scale collapse test at the E-Defense facility. Suita et al. (2008) subjected a full-scale steel moment frame building to both design-level ground motions as well as much larger ground motions to obtain data on real structural behavior up to collapse that could be compared to numerical simulations. The four story building they tested was designed based on current Japanese code requirements and subjected to a ground motion record from the 1995 Kobe earthquake. Due to improvements in the moment connection design and the depth to thickness ratio of the tubular steel columns that was equal to 30, local buckling occurred in the columns causing a weak story collapse mechanism instead of an overall sway mechanism. Further information about the deformation and progression of damage can potentially be used to compare with analytical models in the future.

Nakashima and Liu (2005) tested 1:10 scale tubular steel specimens under combined axial and cyclic loading. A range of axial load levels resulted in different observed failure modes with columns under higher axial loads reaching their maximum strength at lower lateral drift ratios and exhibiting a local "elephant-foot" buckling failure mode. The columns were unable to sustain the large (P/P_y=0.6) applied axial load at drift levels of 4%.

Newell and Uang (2006) experimentally investigated nine full-scale W14 steel sections meeting the ANSI/AISC 341-05 seismic compactness requirements under a combined axial compression and biaxial flexure loading sequence. They developed a statistically based loading scheme using rainflow counting to represent the expected number and distribution of cycles, maximum and cumulative drift, and maximum drift seen by a first story column using computational analyses of 3-story and 7-story buckling resistant braced frames (BRBF) subjected to 20 ground motions. An initial gravity load was applied and followed by in-phase, increasing amplitude cyclic axial load and story drift. Flange local buckling was observed in all but one specimen, but the level of buckling was considered insignificant at drift levels far exceeding the maximum expected drift for a BRBF. The authors concluded that this was due to the stocky nature of the chosen columns.

The tests performed by Newell and Uang (2006) also indicated that the initial residual stress distribution did not significantly affect the axial load-moment interaction or moment versus drift response. Nakashima et al. (1990) conducted small scale tests on 42 compact wide-flange steel columns subjected to axial and monotonic lateral loading. The three columns with the largest slenderness ratios under an axial load greater than or equal to $P/P_y=0.3$ were the only specimens to exhibit local buckling. The local buckling did not result in a significant change in the load deflection behavior. Lateral torsional buckling was also considered negligible in the study due to the fact that it only occurred after every specimen had reached the maximum first-order end moment and was a result of local flange buckling at an earlier stage in the loading scheme. Based on a survey of 224 experimental tests on wide-flange steel beam-columns subjected to combined concentric axial loading and monotonic lateral loading, Nakashima (1994) also concluded that the residual stresses and initial out of straightness did not significantly affect the ductility ratio.

Lignos (2008) performed shake table tests on two 1:8 scale models of a four story steel perimeter moment resisting frame structure. Due to weight limitations of the shake table being used, only half of the four-story structure was physically created. A mass simulator frame was created to support the masses and gravity loads of half of the structure since the gravity loads were necessary for modeling P-delta effects and sidesway collapse. Plastic point hinges were attached at the ends of all beams and columns to simulate the strength and stiffness properties of plastic hinge regions in the prototype structure. Both models collapsed due to a 3-story mechanism, with plastic hinges forming at the top of the third story column despite the fact that the structures fulfilled the strong column weak beam criterion. Lignos stressed the importance of having accurate deterioration models when comparing the results of a simple analytical model to the behavior of the physical test frame. He noted the importance of the post-capping rotation capacity for predicting collapse capacity analytically. The pre-test and post-test simple analytical model used by Lignos led to the conclusion that predicting collapse of a structure with reasonable accuracy using an analytical model is at least feasible.

Cheng et al. (2013) subjected six deep wide-flange cantilever sections to a constant axial load combined with a cyclic lateral displacement up to 0.02 rads and then monotonic lateral displacement until failure. The failure mechanism for each section was attributed to local instabilities. The authors also noted that individual plate limits common in most current design specifications, and AISC (2010) in particular, may not adequately predict the behavior of the sections due to interaction between the flange and web elements. Zargar et al. (2014) investigated a 1:8 scale W36x652 subjected to large drifts under high axial demands. The dominant modes of failure for this particular section under various cyclic and monotonic loading histories are lateral-torsional buckling and web local bucking. The Cheng et al. (2013) and

Zargar et al. (2014) studies are the only existing experimental studies the authors could find that specifically focused on deep steel sections subjected to combined axial and lateral loading, highlighting the lack of data in this area. More importantly, the fact that the deep steel members in these studies experienced significant local buckling and failure under drifts less than 0.04 rads shows that there is a need for further investigation.

3.3 CURRENT AISC SEISMIC DESIGN GUIDELINES

To choose appropriate sections to investigate for the first objective and achieve the second objective, a summary of the current design guidelines which are based on individual plate slenderness limitations is useful. General requirements are outlined in Chapter D of the Seismic Provisions for Structural Steel Buildings (ANSI/AISC 2010) for both moderately and highly ductile steel members and are summarized for highly ductile column members in Table 3-1. As defined in the specification (ANSI/AISC 2010), a highly ductile member is one that is "expected to undergo significant plastic rotation (more than 0.04 rad) from either flexure or flexural buckling under the design earthquake." Table 3-1 indicates that the flange width-to-thickness (b/t) ratio is based solely on material properties, E and F_y, while the web width-to-thickness (h/t_w) ratio is determined by these properties as well as $C_a=P_u/\varphi_c P_y$, which is the ratio of the required strength, P_u, to available strength, $P_y=F_yA_g$, multiplied by the strength reduction factor for compression, $\varphi_c = 0.90$. Limitations for the width-to-thickness ratios, λ_{hd} for highly ductile members, are shown in Figure 3-1 for the specific material properties of the members used in this study (discussed later on). The current member requirements for the width-to-thickness ratios are based on small scale, compact sections subjected to axial compression and pure bending under monotonic, but not cyclic, loading (Lay 1965, Kemp 1986, Dawe and Kulak 1986).

Table 3-1. Current AISC Seismic Design Guidelines (ANSI/AISC 2010)

Description of Element	Width-to-Thickness Ratio	Limiting Width-to-Thickness Ratio
		λhd Highly Ductile Members
Flanges of rolled I-shaped sections.	b/t	$0.30\sqrt{E/F_y}$
Webs of rolled I-shaped sections used as columns	h/tw	For $C_a \leq 0.125$ $2.45\sqrt{E/F_y}(1-0.93C_a)$ For $C_a > 0.125$ $0.77\sqrt{E/F_y}(2.93-C_a)$ $\geq 1.49\sqrt{E/F_y}$ where $C_a = \frac{P_u}{\phi_c P_y}$ $(LRFD)$

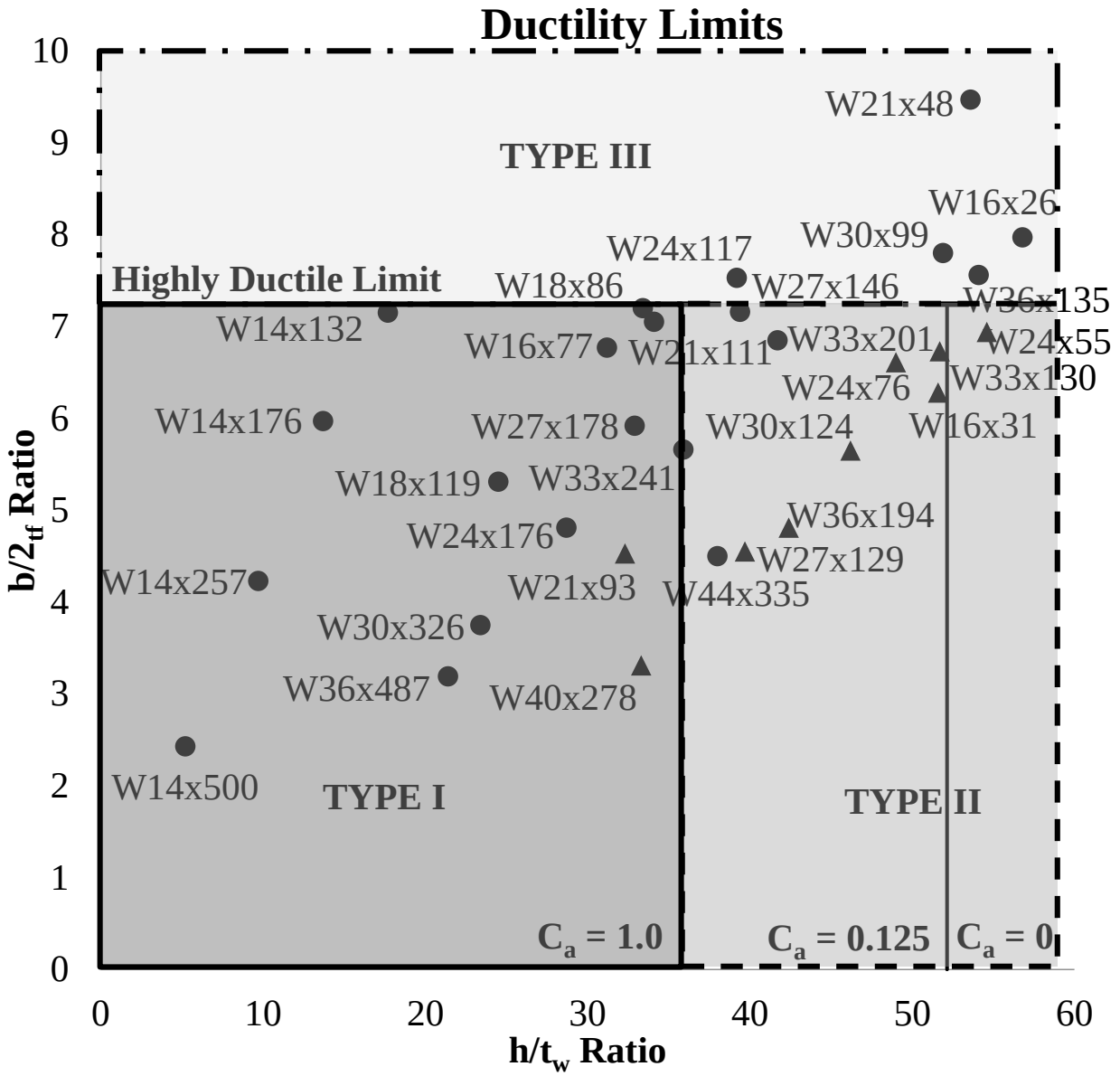

Figure 3-1. Selected columns' slenderness ratios with respect to seismic design guideline limits

Based on the current design guidelines as well as the behavior seen in the limited experimental studies conducted to date, the parameters of interest include the flange and web width-to-thickness ratios, the length of the column, the level of applied axial load, and the boundary conditions. The slenderness ratios of the column as well as variation in the applied axial load are of concern since they are the basis for the current member requirements. The vulnerability of

deeper sections to lateral torsional buckling indicates a need to study the length and boundary conditions of these members under a combined axial and cyclic loading scheme.

3.4 FINITE ELEMENT MODELING

To investigate the collapse behavior of steel columns and the current AISC seismic design guidelines, a number of carefully selected wide flange column members are subjected to a combined axial and cyclic lateral load protocol using finite element simulation.

3.4.1 Prototype Column Selection

Typical column cross-sections found in the steel prototype buildings commissioned by the National Institute of Science and Technology (NIST) and the SAC Steel Project are the basis for the selected sections in this study (Khandelwal et al. 2008). These columns consist of sections that make up the lateral load resisting frame on the first or second story of a structure where axial loads are expected to be largest during a seismic event. Several other columns are chosen due to the availability of experimental data or in an effort to provide a wider range of local slenderness ratios.

As seen in Figure 3-1, the selected columns meet the highly ductile seismic requirements (in the region designated TYPE I in Figure 3-1), are highly ductile for specific axial load ranges (TYPE II) or are on the cusp of being highly ductile (TYPE III). TYPE III members exceed the highly ductile flange width-to-thickness ratio, but were chosen to explore the current guidelines in the event that they are found to be overly conservative.

Based on the AISC (2010) guidelines, the W36x194 is slender in compression due to the h/t_w, but meets the seismic member requirements for a highly ductile member as long as the ratio of

required strength to nominal axial strength, C_a, does not exceed 0.64. The other columns listed under TYPE II in Table 3-2 are similar to the W36x194 with different ratios of required strength to available strength needed to meet the highly ductile requirements. This is also shown in Figure 3-1 by the fact that these columns are below the horizontal solid line (flange width-to-thickness limit) and to the right of the leftmost solid vertical line (h/t_w limit for $C_a=1$).

Table 3-2. Column data used for regression analysis and comparison with expected axial load.

Section	$\frac{h}{t_w}$	$\frac{b}{t}$	$\frac{L}{r_y}$	$\frac{JS_x}{h_o}$	$\frac{\sqrt{JI_y}}{G}$	F_{ez}	CALR (FE)	Maximum Expected P/P_y (AISC Guidelines)
TYPE I								
W14x132	17.7	7.15	47.90	0.0043	0.0025	3.26	0.80	0.85
W14x176	13.7	5.97	44.75	0.0068	0.0046	3.82	0.70	0.86
W14x257	9.71	4.23	43.58	0.0131	0.0099	5.10	0.70	0.87
W14x500	5.21	2.43	40.67	0.0383	0.0377	8.90	0.80	0.89
W18x86	33.4	7.2	68.44	0.0014	0.0008	1.45	0.30	0.71
W18x86	33.4	7.2	45.63	0.0014	0.0019	2.75	0.50	0.86
W18x119	24.5	5.31	89.39	0.0026	0.0009	1.29	0.30	0.56
W18x119	24.5	5.31	67.04	0.0026	0.0016	1.75	0.40	0.72
W18x119	24.5	5.31	44.70	0.0026	0.0036	3.07	0.60	0.86
W21x93*	32.3	4.53	97.58	0.0015	0.0007	3.85	NM**	0.50
W21x111	34.1	7.05	62.18	0.0013	0.0013	1.26	0.50	0.75
W21x111	34.1	7.05	41.46	0.0013	0.0030	2.48	0.60	0.88
W24x176	28.7	4.81	59.14	0.0022	0.0033	1.19	0.50	0.63
W24x176	28.7	4.81	78.85	0.0022	0.0019	0.83	0.50	0.77
W24x176	28.7	4.81	39.42	0.0022	0.0074	2.22	0.60	0.89
W27x178	32.9	5.92	73.81	0.0015	0.0018	0.65	0.40	0.67
W27x178	32.9	5.92	36.91	0.0015	0.0073	2.00	0.50	0.80
W27x178	32.9	5.92	55.36	0.0015	0.0033	1.00	0.60	0.90
W30x326	23.4	3.75	66.71	0.0033	0.0062	0.76	0.30	0.72
W30x326	23.4	3.75	50.03	0.0033	0.0110	1.09	0.50	0.83
W30x326	23.4	3.75	33.35	0.0033	0.0248	2.02	0.80	0.90
W33x241	35.9	5.66	66.21	0.0013	0.0057	0.81	0.20	0.71
W33x241	35.9	5.66	49.65	0.0013	0.0057	0.81	0.30	0.82

W33x241	35.9	5.66	33.10	0.0013	0.0128	1.67	0.60	0.90
W36x487	21.4	3.19	60.38	0.0023	0.0133	0.65	0.40	0.76
W36x487	21.4	3.19	45.29	0.0023	0.0236	0.93	0.50	0.86
W36x487	21.4	3.19	30.19	0.0023	0.0530	1.75	0.80	0.90
W40x278*	33.3	3.31	71.41	0.0017	0.0057	0.15	NM**	0.69
TYPE II								
W16x31*	51.6	6.28	153.8	0.0006	0.0001	0.71	NM**	0.13
W16x77	31.2	6.77	72.84	0.0017	0.0021	1.68	0.30	0.30
W24x55*	54.6	6.94	134.3	0.0004	0.0002	0.40	NM**	0.07
W24x76*	49.0	6.61	93.79	0.0007	0.0005	0.60	NM**	0.26
W27x129*	39.7	4.55	81.58	0.0012	0.0014	0.24	NM**	0.61
W27x146	39.4	7.16	56.14	0.0010	0.0022	0.94	0.30	0.72
W27x146	39.4	7.16	37.43	0.0010	0.0049	1.92	0.50	0.72
W30x124*	46.2	5.65	80.83	0.0008	0.0012	0.51	NM**	0.39
W33x130*	51.7	6.73	75.45	0.0006	0.0012	0.47	NM**	0.13
W33x201	41.7	6.85	50.60	0.0009	0.0039	0.77	0.40	0.61
W33x201	41.7	6.85	33.74	0.0009	0.0087	1.62	0.50	0.61
W36x194*	42.4	4.81	70.18	0.0009	0.0028	0.47	NM**	0.58
W44x335	38.0	4.50	51.57	0.0013	0.0092	0.40	0.30	0.81
TYPE III								
W16x26*	56.8	7.97	161.1	0.0004	0.0000	0.63	NM**	NHD***
W21x48*	53.6	9.47	108.7	0.0004	0.0002	0.62	NM**	NHD***
W24x117*	39.2	7.53	61.26	0.0010	0.0014	1.02	NM**	NHD***
W30x99*	51.9	7.80	85.83	0.0005	0.0007	0.48	NM**	NHD***
W36x135*	54.1	7.56	75.61	0.0005	0.0012	0.42	NM**	NHD***

*Sections not used in regression analysis

**CALR is Not Measured (NM) since section did not reach 4% drift under $0.20P_y$

***Not Highly Ductile (NHD) member based on current design guidelines

The maximum expected value of P/P_y occurs when $C_a=1$ implying that ratio of axial demand to the squash load of the section is equal to ϕ_c, which is the resistance factor for compression, or 0.90. This is assuming the compression strength of the member is capable of reaching $0.90P_y$ prior to buckling. To account for buckling, the expected value for TYPE I and TYPE II members listed in Table 3-2 is the smaller of the values calculated using 1) the limits in Table 3-1, and 2) the nominal compressive strength equations of Chapter E (AISC 2010) divided by P_y. The interaction of the axial load and moment is neglected in determining the expected axial load per ANSI/AISC 2010 Chapter D Section 4a(2) and a conservative value of $K=1$ is used to determine the capacity of the members as suggested in the specification. For TYPE III members, an expected value of $P/P_y = NHD$ $(not\ highly\ ductile)$ indicates that the member cannot be considered highly ductile under the current AISC seismic design guidelines and is not expected to reach 4% drift under the combined loading scheme.

3.4.2 Model Setup

Detailed finite element models of the cross-sections shown in Figure 3-1 are created using the commercial software Hypermesh (2011) and analyzed using the commercial code LS-Dyna (2005). The columns are modeled using fully integrated shell elements (ELFORM 16) based on the formulation described by Engelmann et al. (1989) for a large-displacement small-strain context. The geometry is modified to include an initial imperfection that assumes a sinusoidal shape with a maximum deflection of L/1000 at mid-height. Sensitivity studies are performed to ensure an appropriate mesh is selected for further investigations. A mixed isotropic-kinematic hardening plasticity model (LS-Dyna MAT_003) is used and calibrated with available steel coupon data (Kaufman et al. 2001) as shown in Figure 3-2. It is clear from the figure that the

stiffness and hardening response of the model matches reasonably well with experimental data and is deemed adequate for this particular study.

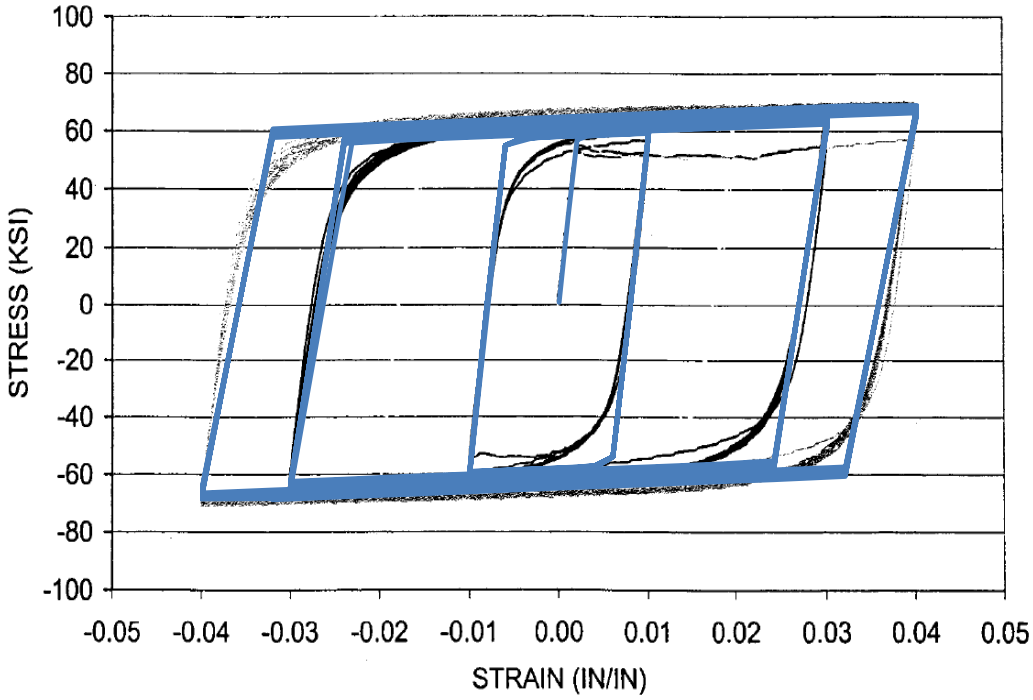

Figure 3-2. Material model calibration with A913 Grade 50 steel coupon (Kaufman et al. 2001).

3.4.3 Length, Boundary Conditions, and Loading Scheme

Exterior first story columns in moment resisting bays are potentially the most critical columns since they are likely to see some of the largest axial loads due to overturning moments during a seismic event. For this reason, the columns are either 3.05 m, 4.57m, or 6.10 m long to cover the range of typical first story column member heights used in the US West Coast. In addition, the boundary conditions of the finite element models are chosen to idealize those of a first story column. The bottom of the column is fixed while the top has some released degrees of freedom as shown in Figure 3-3. The top of the column is free to translate in the x and z directions. It is also free to rotate about the x-axis. This is meant to simulate the member having a moment

connection perpendicular to the strong axis and a shear tab connection parallel to the strong axis. Rigid plate caps are attached at either end to distribute the applied loads over the entire cross section without causing local deformation.

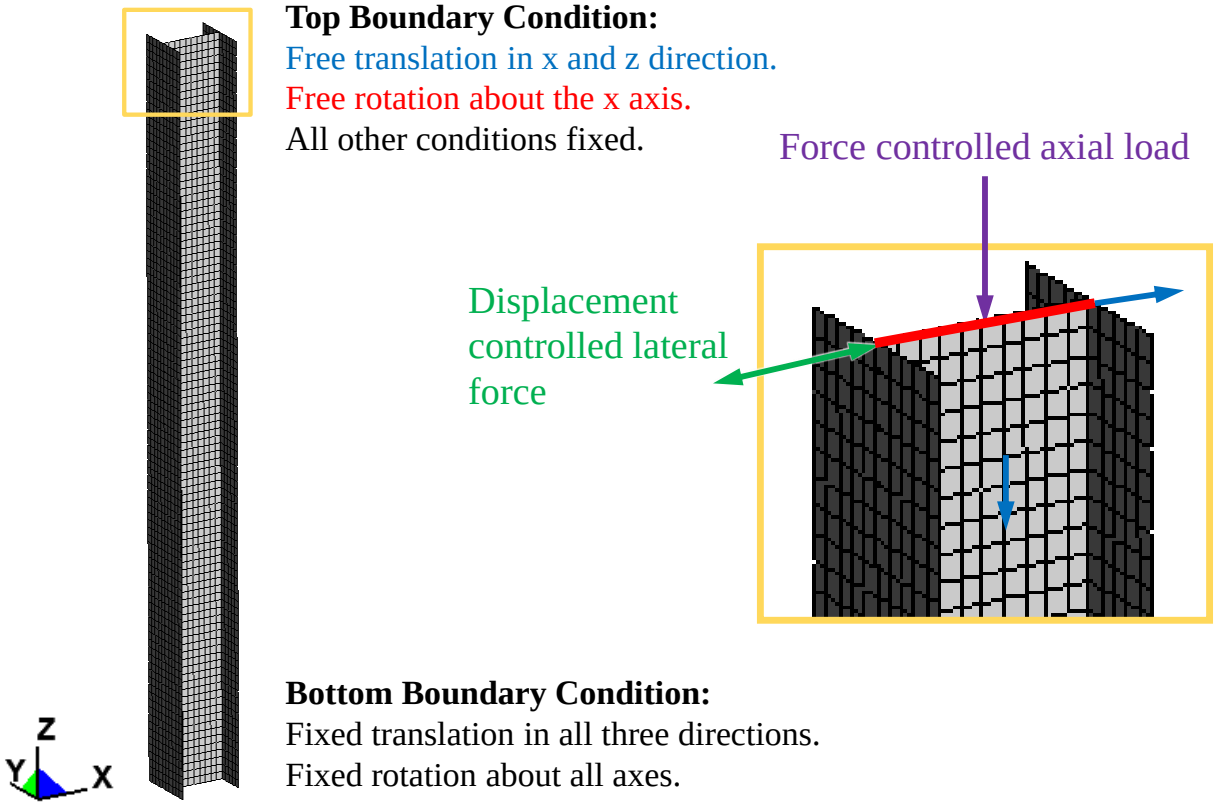

Figure 3-3. Finite element validation model showing mesh and boundary conditions.

The loading protocol entails application of a force controlled axial load in phase with a displacement controlled lateral load. The axial compressive load increases as the drift increases until the target load and drift are reached simultaneously. The displacement then reverses direction and the axial load is reversed (potentially going into tension) to represent the loading an actual column experiences during a seismic event. Members are investigated under maximum compression loads ranging from $0.2P_y$ to $0.9P_y$ ($P_y=F_yA$). The combined axial and cyclic loading scheme is shown in Figure 3-4 where the maximum compression load is $0.5P_y$ and the load

fluctuates about an average of $0.15P_y$ in compression to represent the gravity load on the column. Table 3-3 summarizes the story drift ratio and number of cycles for the loading scheme. This loading protocol is based on the basic loading history developed by Krawinkler et al. (2000) for moment frames and modified by Newell and Uang (2006) for braced frames. The loading rate of 0.46 m/s is selected through a trial and error process as a compromise to reduce computational run time while minimizing the dynamic effects associated with rapid loading.

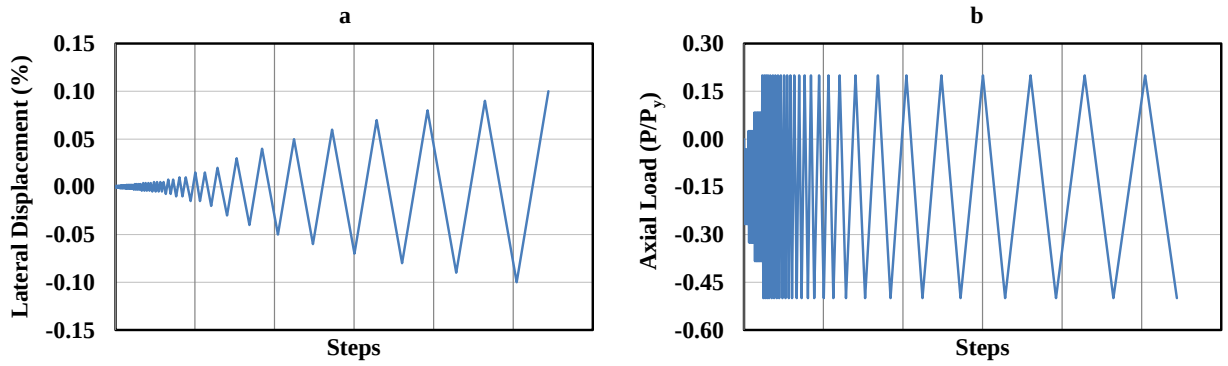

Figure 3-4. Loading protocol for a) lateral displacement and b) axial load.

Table 3-3. Loading sequence after initial axial gravity load is applied.

Story Drift Ratio	Number of Cycles	Story Drift Ratio	Number of Cycles
0.001	6	**0.02**	1
0.0015	6	**0.03**	1
0.002	6	**0.04**	1
0.003	4	**0.05**	1
0.004	4	**0.06**	1
0.005	4	**0.07**	1
0.0075	2	**0.08**	1
0.01	2	**0.09**	1
0.015	2	**0.10**	1

3.4.4 Failure Criterion

Three failure criteria are used to define failure of the member under this loading scheme: 1) 10% reduction in the lateral load, 2) 10% reduction in the moment at the base of the column, as

discussed next, and 3) complete loss in the ability to carry the applied axial load (collapse). The moment at the base of the column, *M*, is calculated as follows:

$$M = \frac{1}{2}(HL - P\Delta) \tag{3-1}$$

Where the axial load, *P*, is positive in tension, *H* is the lateral force on the column, *L* is the length of the column, and Δ is the lateral displacement at the top of the column.

The moment criterion has been used previously to define failure (Newell and Uang 2006). The lateral load criterion was used by Cheng et al. (2013) to investigate the structural behavior of the member due to second order moments ($M_2 = P\Delta$) by comparing the total moment, *M*, with the moment due to only first order effects ($M_1 = HL$). The axial failure criterion, or inability to carry the applied axial load, i.e. explicit collapse, is unique to this study and used due to its obvious physical meaning.

To illustrate use of the 3 failure criteria, consider a 4.57 m long column with a W36x487 section. As the load fluctuates between tension (positive force) and compression (negative force) in phase with the lateral drift oscillating from left (positive displacement) to right (negative displacement), the moment and lateral force begin to degrade as seen in Figure 3-5. Once the moment and lateral force drop 10% below their peak values as shown by the solid line in Figure 3-5(a) and (b), the furthest drift where this line intersects the moment or force-displacement diagram corresponds to the failure of the column. The axial failure criterion is obtained by determining the time step at which the axial force is unable to reach the target load as shown in Figure 3-6(b) and choosing the largest drift reached prior to that time step (Figure 3-6(a)). This criterion is obvious during the simulation as the column collapses suddenly as indicated in Figure

3-6(b) and 6(c). The results for this particular section for various levels of applied axial load are summarized in Table 3-4 and Figure 3-7.

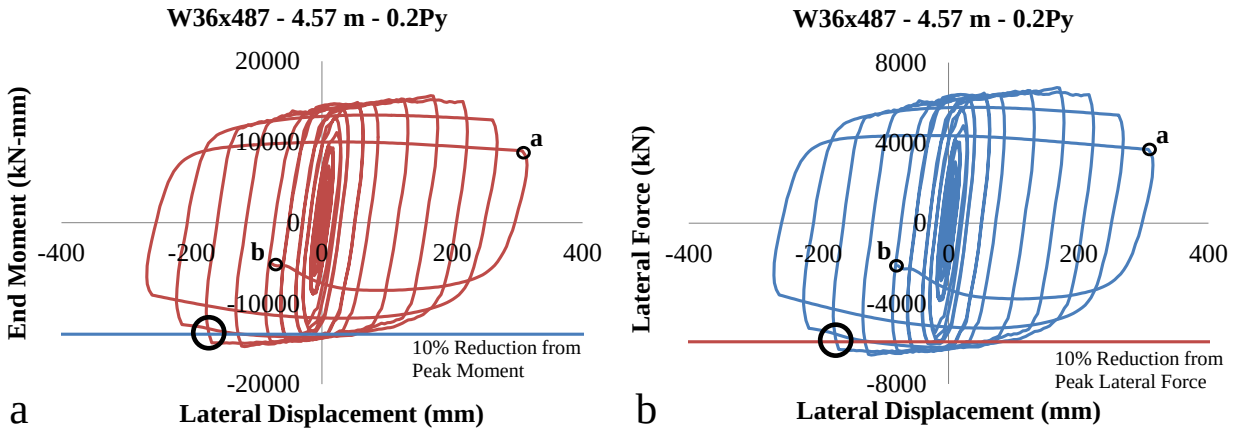

Figure 3-5. Failure criterion for 4.57 meter W36x487-0.2Py column based on a 10% reduction in a) moment and b) lateral force.

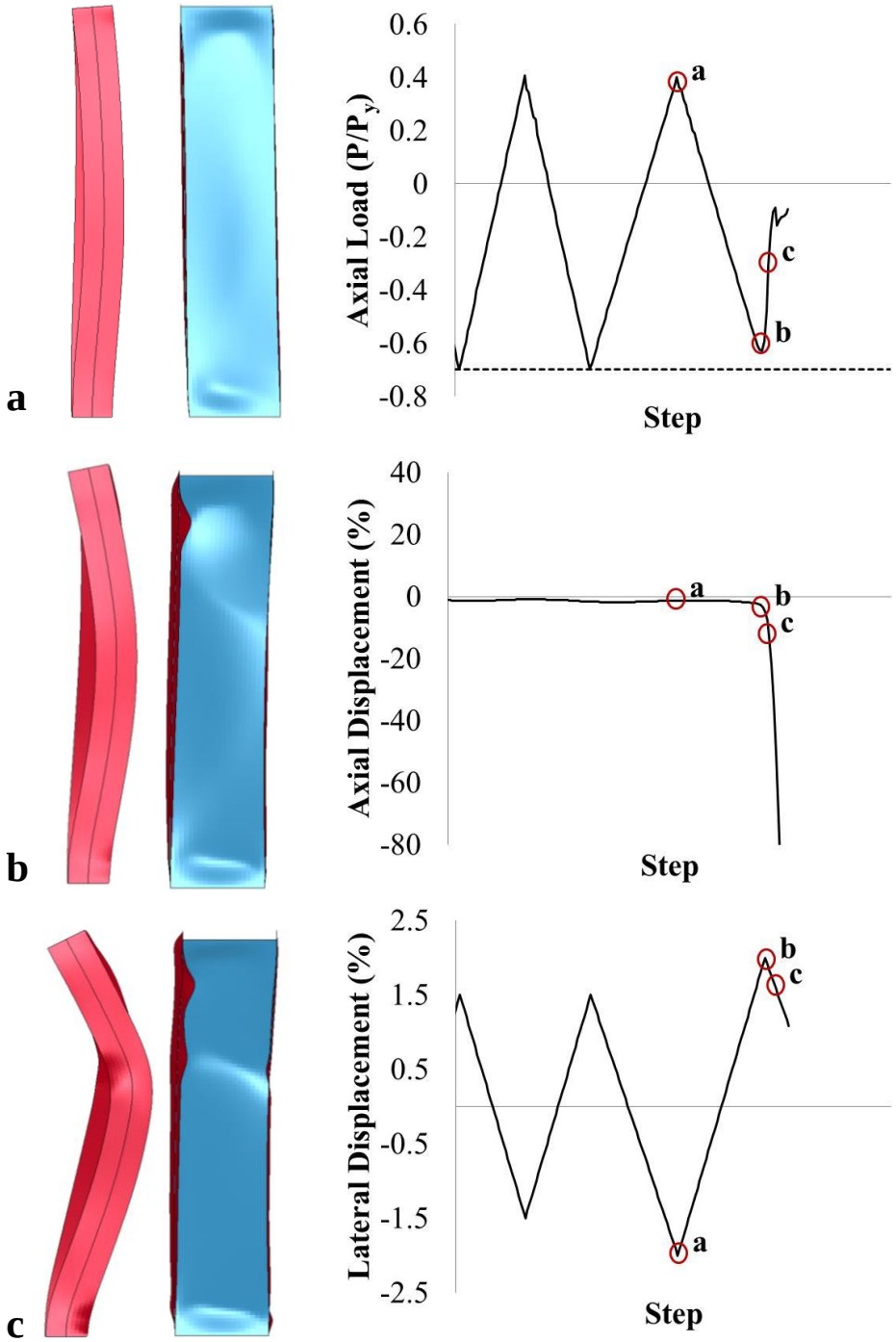

Figure 3-6. Progression of axial load failure for 4.57 meter W36x4987-0.7Py column as shown by a) last half-cycle able to reach target displacement under target axial load, b) inability to reach target axial load at target displacement, and c) sudden drop in axial load and increase in axial displacement.

Table 3-4. Summary of drift reached based on different failure criteria under various axial loads for a 4.57 m W36x487 column.

W36x487						
P/Py	10% Lateral Force Criterion		10% Moment Criterion		Axial Force Criterion	
	mm	%	mm	%	mm	%
0.2	174	3.80	183	4.00	320	7.00
0.3	137	3.00	165	3.60	274	6.00
0.4	110	2.40	128	2.80	274	6.00
0.5	82.3	1.80	86.9	1.90	229	5.00
0.6	54.7	1.20	54.4	1.30	137	3.00
0.7	22.8	0.40	32.0	0.70	91.4	2.00
0.8	22.8	0.40	22.8	0.40	68.6	1.50
0.9	9.09	0.20	9.09	0.20	22.9	0.50

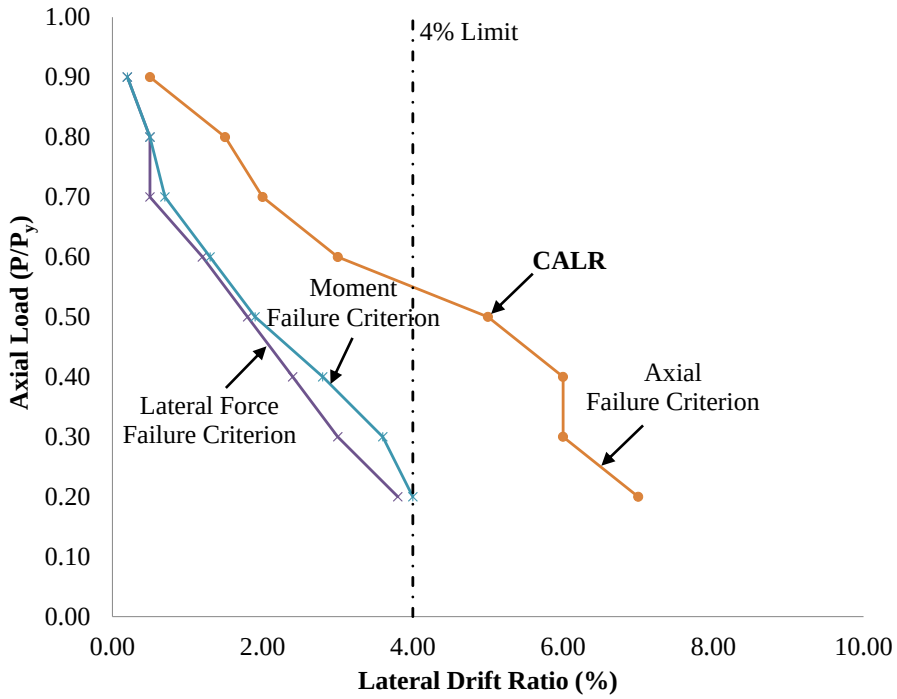

Figure 3-7. Summary of failure criterion for 4.57 m W36x487 column with CALR shown.

3.4.5 Measures of Performance

There is no clear consensus in the AISC Seismic Specifications (2010) regarding the use of total versus plastic deformations as a measure of structural performance. For example, while member performance is described as a function of plastic rotation, connection response is specified as a function of total drift in the AISC Seismic Specifications (2010). With emphasis on the axial load failure criterion in this work, separating elastic deformations from total deformation is not clear cut. The problem is geometrically nonlinear, and so elastic deformations are strongly dependent on the applied axial load history, which varies during the loading protocol. Also, in some cases, the failure point is low on the softening portion of the lateral load versus drift curve, making it unclear how to compute the elastic component of deformations. To avoid confusion, lateral drift, which is equivalent to total rotation for the column configurations used, is utilized instead of plastic rotation to gage structural performance in the AISC sense. As such, highly ductile columns are those that reach drifts of at least 0.04 radians. Other researchers, such as Newell and Uang (2006) and Fadden and McCormick (2014), have also used total rotations in their work.

The critical axial load ratio (CALR) is defined as the maximum axial load ratio that a member can sustain under the given loading scheme and reach 4% lateral drift. Determination of the appropriate P/P_y value for the CALR of W36x487 is shown in Figure 3-7 and is also bolded in Table 3-4. This table indicates that the top of the 4.57 m W36x487 column is able to move laterally 229 mm, or 5% of the column height, while carrying 15902 kN, or 50% of the section's squash load ($0.5P_y$), before failing based on the axial load failure criterion. If the load is increased to $0.6P_y$, the W36x487 is only able to reach 3% drift and therefore the 4.57 m

W36x487 should not be considered a highly ductile member under that loading. As such, the CALR of this member is $0.5P_y$.

3.5 FINITE ELEMENT MODEL VALIDATION

Model validation is conducted using the Newell and Uang (2006) experimental data, which focused on full-scale specimens meeting the ANSI/AISC 341-10 (2010) seismic compactness requirements subjected to a combined axial compression and flexure loading sequence.

3.5.1 Model Setup

Two detailed finite element models of the test setup are created and analyzed using the commercial code LS-Dyna (2005). The models consist of 4.57 m W14x132 and W14x176 columns subjected to various axial and lateral drift loads. To address the fact that the experimental setup is physically unable to achieve the ideal case of full fixity that is feasible in a finite element program, vertical springs are added at the ends of the columns (as shown in Figure 3-8) to match the stiffness seen in the experimental plots of end moment and lateral force versus lateral drift. As deployed, the springs, each with a stiffness of 8756 kN/mm, provide rotational flexibility to both column ends. The upper column end is allowed to translate vertically (z) and horizontally (x) as shown in Figure 3-8.

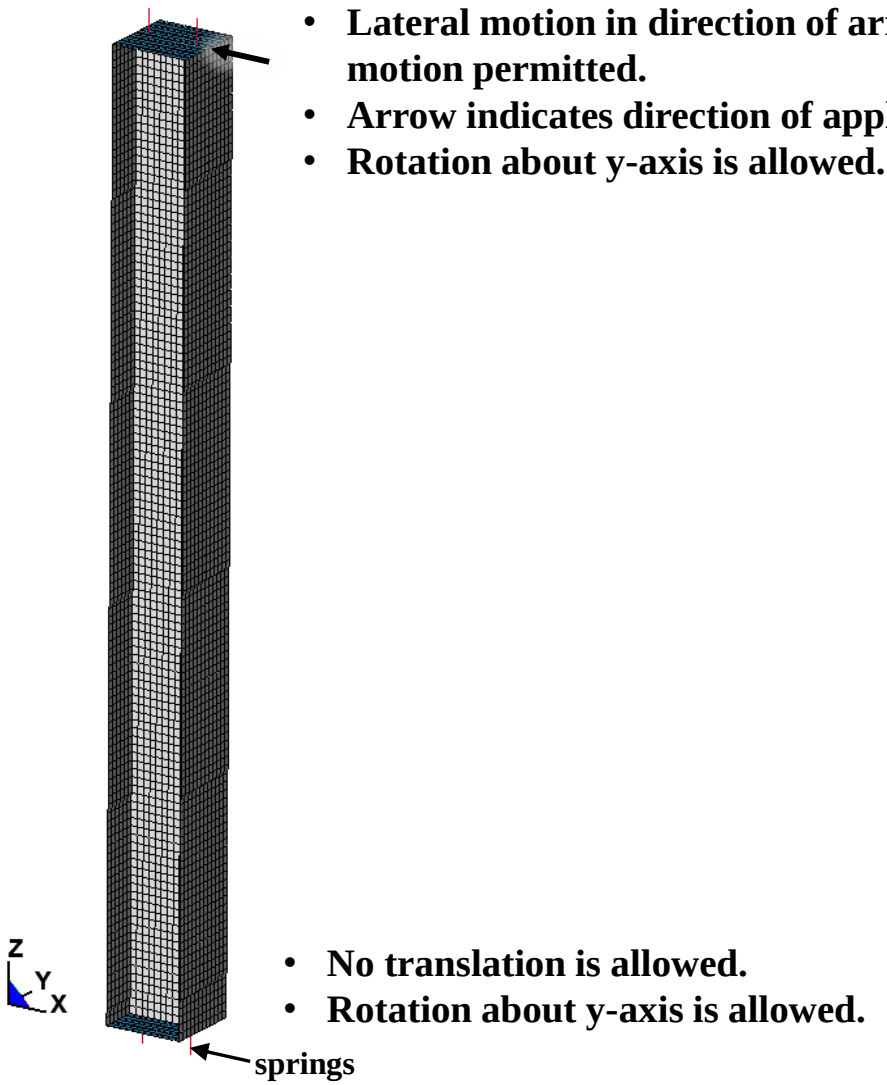

Figure 3-8. Finite element validation model showing mesh and boundary conditions.

The material properties from a cyclic coupon test performed at Lehigh University (Kaufman et al. 2001) are deemed an adequate representation per Newell and Uang, of the A992 steel member specimens used in their experimental work. Therefore, steel with a yield strength of 372 MPa, an ultimate strength of 796 MPa and an elongation of 36% are utlized for this validation study. Residual stresses are not included in the computational study because Newell and Uang (2006) showed through their work that the residual stresses have an insignificant impact on the behavior of the column under the combined loading case.

3.5.2 Loading Scheme

The loading scheme consists of applying a displacement controlled lateral load in phase with a force controlled axial load similar to that seen in Figure 3-4, which is consistent with the experimental techniques used by Newell and Uang (2006). While the experimental loading protocol is similar to that used in the finite element parametric study, the two loads are not actually applied simulataneously in phase due to limitations of the experimental setup. The physical loading scheme consisted of laterally displacing the column to the desired drift, then applying the the axial displacement until the target axial load was reached. This can be seen in Figure 3-9 where there are large vertical jumps in the lateral force and end moment at constant drift levels. This discrepancy in loading is replicated in the validation study by using a displacement controlled lateral load followed by a force controlled axial load applied after reaching the target drift ratio.

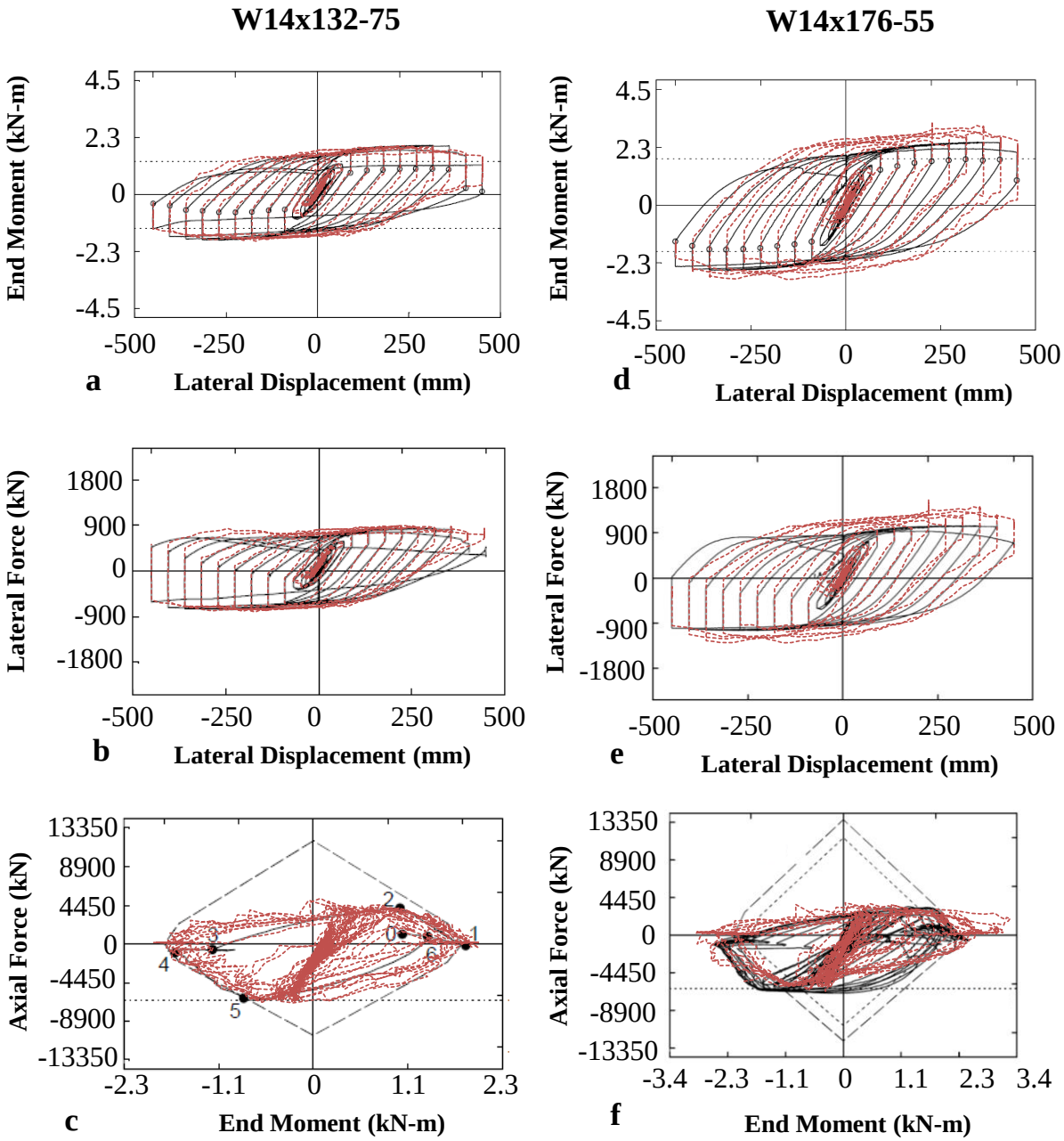

Figure 3-9. Comparison of a) moment versus lateral displacement, b) lateral force versus lateral displacement, and c) P-M interaction response between computational model (dashed lines) and experimental results (solid lines) for W14x132-75. Similar comparisons are shown in d-f for the W14x175-55.

3.5.3 Simulation Results

A W14x132 column with an applied axial load that is 75% of the column squash load (W14x132-75) and W14x176 column with an applied axial load that is 55% of the column squash load (W14x176-55) are investigated and comparison of the column responses are shown in Figure 3-9. A comparison of the deformed shapes at 10% lateral drift is shown in Figure 3-10. The different directions of the buckled flanges between the experimental setup and the finite element model is attributed to differences in initial imperfections. However, the location and length of local buckling is consistent with that seen in the experimental setup. As is seen in the plots of force-displacement, the interaction diagram, and general deformed behavior, the computational study matches well with the available experimental data and provides confidence that the current study using similar modeling techniques is providing reasonable behavior.

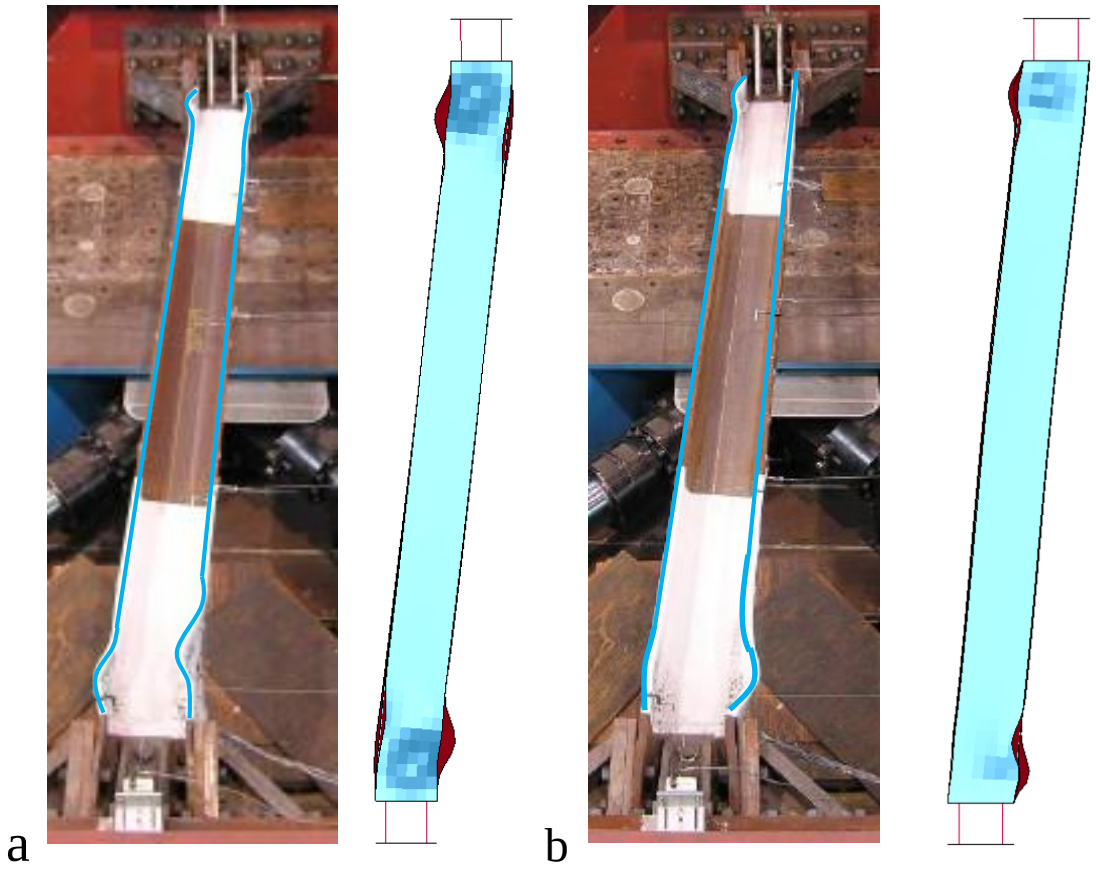

Figure 3-10. Comparison of deformed member at 10% drift for a) W14x132-75 and b) W14x176-55 (Newell and Uang 2006).

3.6 RESULTS OF PARAMETRIC STUDY

In total, 70 different members are used in this parametric study. Thirty different sections are selected and twenty of those sections are investigated at three different column lengths. Although there are exceptions, the general mode of failure for these deeper sections consists of local web and/or flange buckling leading to global failure through a combination of torsional and flexural behavior.

Nearly half of the columns in this study failed to achieve the plastic rotation of 0.04 radians that is expected of a highly ductile member under the lowest considered axial load (P/P_y = 0.20).

None of the sections in this study, including the compact W14 sections, are able to carry their maximum expected C_a value and reach the 4% lateral drift expected of a highly ductile member.

While some of these failures can be attributed to lack of compliance with current AISC guidelines, all of the members that do satisfy the requirements fail to reach the axial load levels specified as shown in Table 3-2 where the actual P/P_y value is the CALR recorded from the finite element simulations. A value of $P/P_y = NM\ (not\ measured)$ merely indicates that the member was unable to reach 4% drift under the lowest axial load ($P/P_y = 0.20$) investigated. To facilitate discussion of the behavior of the different section types hereon, a roman numeral following a section indicates the type of section as described previously (e.g. W18x211-I where W18x211 is TYPE I).

3.6.1 Flange Width-to-Thickness Ratio

There is a slight downward trend with a high amount of scatter between the CALR and flange web-to-thickness ratio for the sections studied as shown in Figure 3-11. In terms of the range of behavior seen at the extremes as circled in Figure 3-11(a), the (1) W18x86-I (b/t = 7.2, h/t_w = 33.3, L/r_y = 68.4) experiences significant local web and flange buckling leading to flexural-torsional buckling while the (2) W30x326-I (b/t = 3.75, h/t_w = 23.4, L/r_y = 66.7) is dominated by flexural-torsional buckling leading to local flange and web buckling. On the high CALR end, the (3) W14x132-I (b/t = 7.15, h/t_w = 17.7, L/r_y = 47.9) is dominated by local flange buckling, then local web buckling, and finally flexural-torsional buckling while the (4) W14x500-I (b/t = 2.43, h/t_w = 5.21, L/r_y = 40.7) is dominated by flexural buckling behavior and minor local flange buckling. The deformed shapes of these columns are shown just prior to axial load failure in

Figure 3-12. Columns with lower CALR tend to have higher values of L/r_y while the columns with higher CALR tend to have lower values of L/r_y.

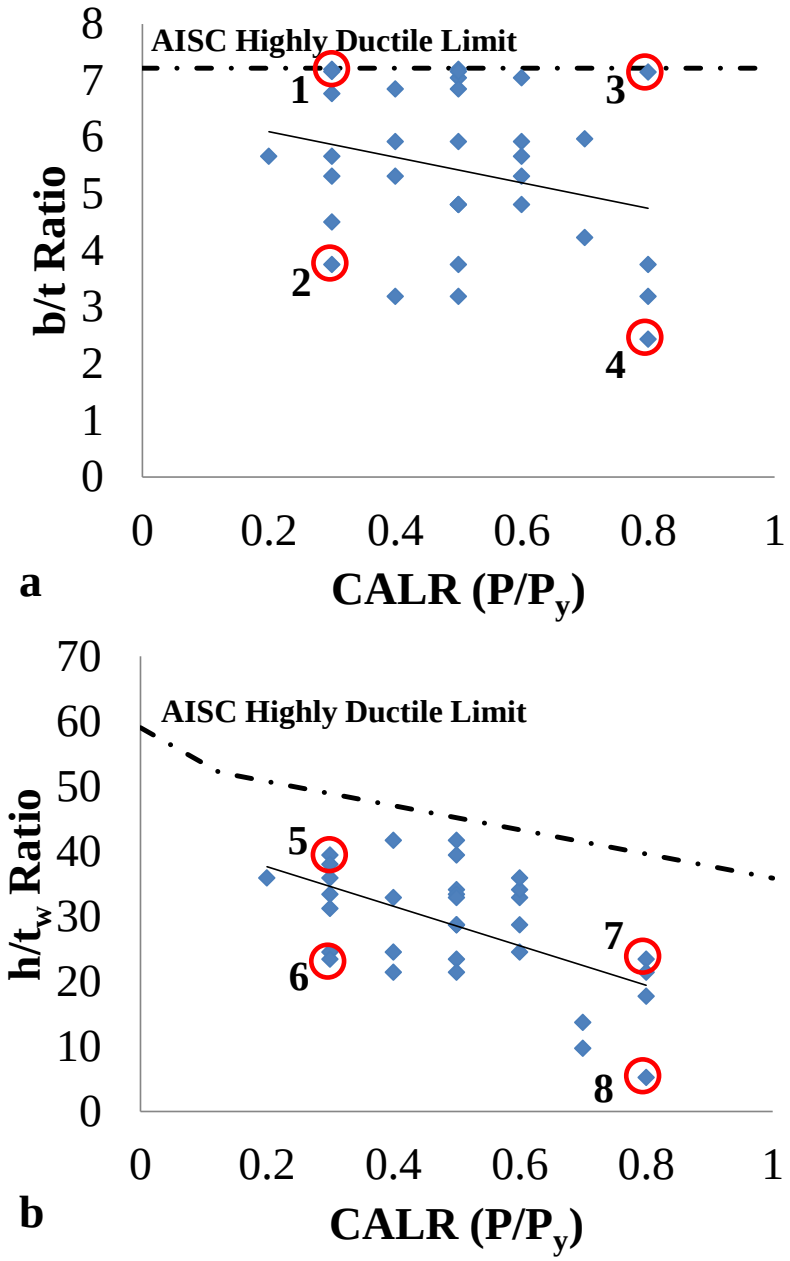

Figure 3-11. Capacity of columns with trends regarding a) flange width-to-thickness ratio and b) web width-to-thickness ratio for (1) W18x86 – 15ft, (2) W30x326 – 20ft, (3) W14x132 – 15ft, (4) W14x500 – 15 ft, (5) W27x146 – 15ft, (6) W18x119 – 20ft, (7) W30x326 – 10ft, and (8) W14x500 – 15ft.

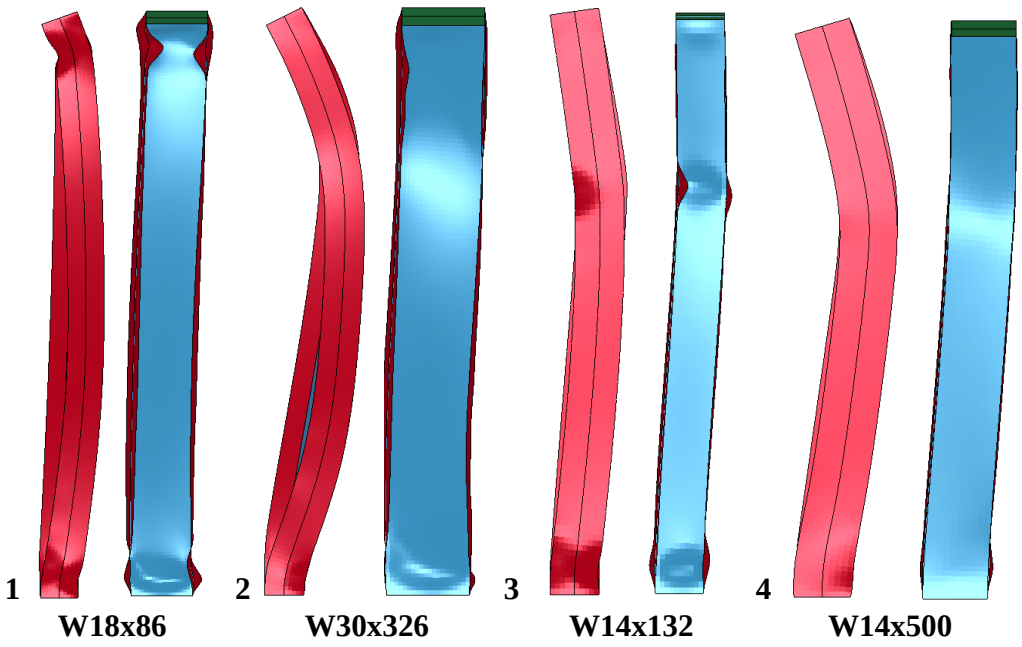

Figure 3-12. Displaced shape just prior to axial failure criterion for columns under $0.20P_y$ for extremes shown in Figure 3-11(a)

The W40x278-I (b/t = 3.31, h/t_w = 33.3, L/r_y = 71.4) initially experiences flange local buckling and subsequently web local buckling then eventually significant flexural torsional behavior. Compared with the W18x86-I (b/t = 7.2, h/t_w = 33.3, L/r_y = 68.4), which is similar in web width-to-thickness but different in flange width-to-thickness, the sequence of failure and global failure of the two columns is similar in terms of the general location of the largest out-of-plane displacement as seen in Figure 3-13(a).

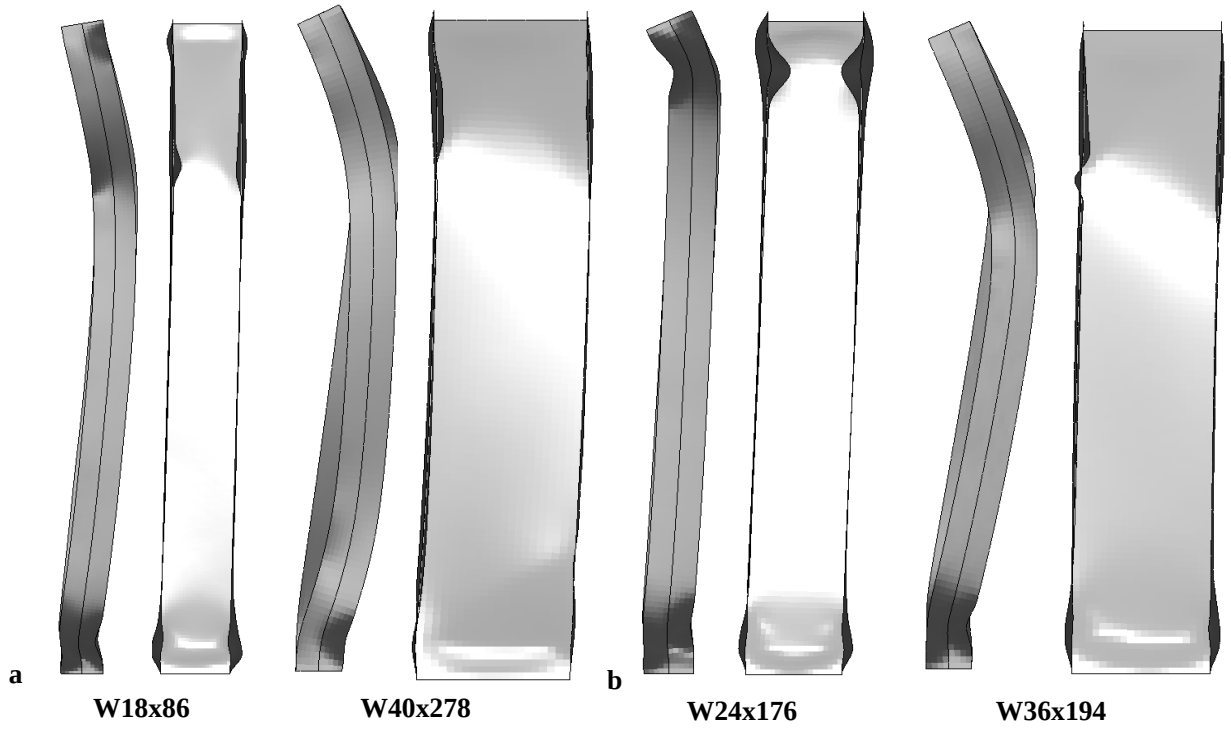

Figure 3-13. Displaced shape just prior to axial failure criterion for columns under $0.20P_y$ comparing a) different h/t_w (same b/t), and b) different b/t (similar h/t_w)

None of the members with b/t ratios greater than the highly ductile limit (TYPE III) are able to achieve a CALR of $0.2P_y$ or greater. Member W24x117-III (largest h/t_w for Type III) experiences local flange buckling followed by flexural-torsional buckling and web local buckling. The W21x48-III (highest b/t) experiences failure due to local flange buckling as well as flexural-torsional behavior. The W16x26-III (lowest h/t_w for TYPE III) experiences flange and web buckling followed by flexural buckling.

In addition to TYPE III members failing to maintain this low axial load up to 4% drift, there were also several members below this limit that failed to maintain the lowest axial load level (designated as triangles in Figure 3-1). While the conclusion can be drawn that members above this limit cannot be highly ductile, it does not hold true that members below this limit are necessarily highly ductile.

3.6.2 Web Width-to-Thickness Ratio

There is a clear negative correlation between the CALR and h/t_w as shown in Figure 3-11(b). This corresponds to the AISC Seismic Design guidelines approach, which limits h/t_w based on the expected axial load on the column. In terms of the range of behavior seen at the extremes as circled in Figure 3-11(b), the (5) W27x146-II (b/t = 7.16, h/t_w = 39.4, L/r_y = 56.1) experiences significant local web and flange buckling while the (6) W18x119-I (b/t = *5.31*, h/t_w = 24.5, L/r_y = 89.4*)* is dominated by flexural-torsional buckling followed by local web and flange buckling. The (7) W30x326-I (b/t = 3.75, h/t_w = 23.4, L/r_y = 33.4*)* experiences local flange and web buckling and finally flexural-torsional buckling while, as mentioned previously, the (8) W14x500-I (b/t = 2.43, h/t_w = 5.21, L/r_y = 40.7) is dominated by flexural buckling behavior and minor local flange buckling. The failure modes for these columns are shown in Figure 3-14. Columns with lower CALR tend to have higher values of L/r_y and b/t while the columns with higher CALR tend to have lower values of L/r_y and b/t.

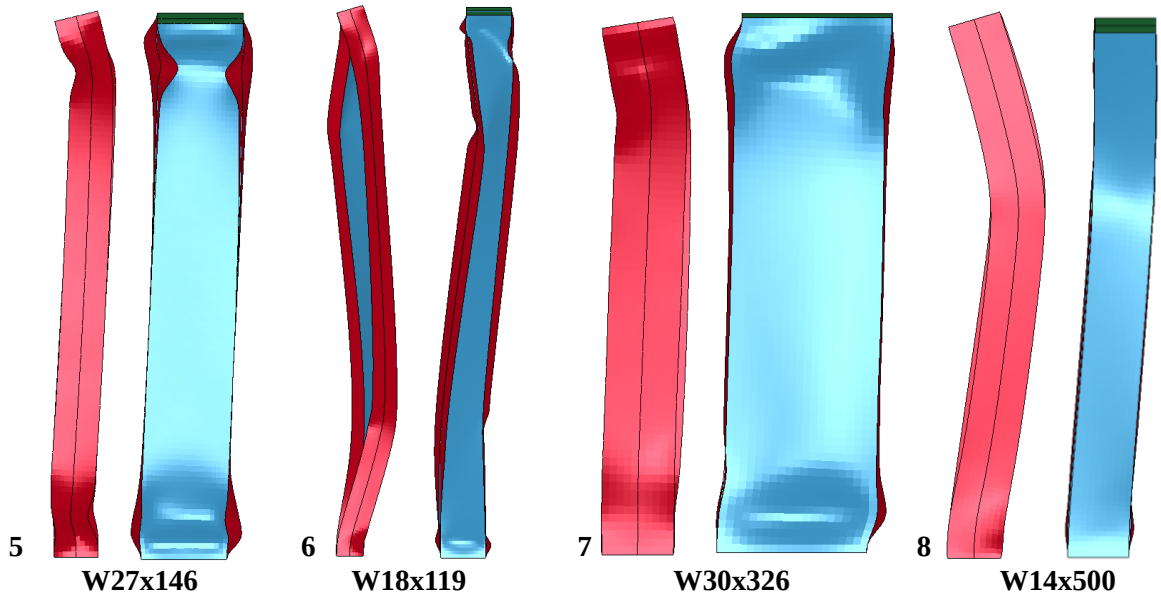

Figure 3-14. Displaced shape just prior to axial failure criterion for columns under 0.20P_y for extremes shown in Figure 3-11(b)

The web width-to-thickness ratio appears to influence the failure mode of the section as shown in Figure 3-13(b). The W24x176-I (b/t = 4.81, h/t_w = 28.7*)* is dominated by flange local buckling that leads to the formation of plastic hinges near the column ends while the W36x194-II (b/t = 4.81, h/t_w = 42.4*)* is dominated by web local buckling that leads to significant twisting and ultimately failure due to flexural-torsional buckling. Despite the fact that these sections have the same b/t ratio, the initiation and ultimate failure modes of these two sections are significantly different. For the sections studied, h/t_w appears to play a more dominant role in the strength of the columns than the b/t.

Nine of the members, as shown by the triangles in Figure 3-1, that satisfy the AISC guidelines for highly ductile members are incapable of reaching a 4% lateral drift when P/P_y = 0.20. The plate slenderness ratios of the sections alone are not a clear indication of the capacity of these sections under a combined loading scheme as seen by the fact that the W27x129-II (b/t = 4.55, h/t_w = 39.7*)* and W21x93-I (b/t = 4.53, h/t_w = 32.3*)* cannot carry P/P_y = 0.20 up to 4% lateral drift, while a W44x335-II (b/t = 4.50, h/t_w = 38.0*)*, which is very similar in terms of both ratios, is able to carry P/P_y = 0.30 up to 4% lateral drift. This suggests that other parameters are influential.

3.6.3 Unbraced Length

Unbraced lengths of 3.04 m, 4.57 m, and 6.10 m for several members are considered to investigate the effect of unbraced length on capacity. As shown in Figure 3-15, the same general trends previously observed are seen, i.e. there is a severe reduction in ductility with increasing axial load level. The effect appears to be accentuated as the column global slenderness increases, which is attributed to a shift in the failure mode. Local buckling is the dominant failure mode in

the shortest column, while lateral torsional buckling becomes more dominant as the length of the column increases.

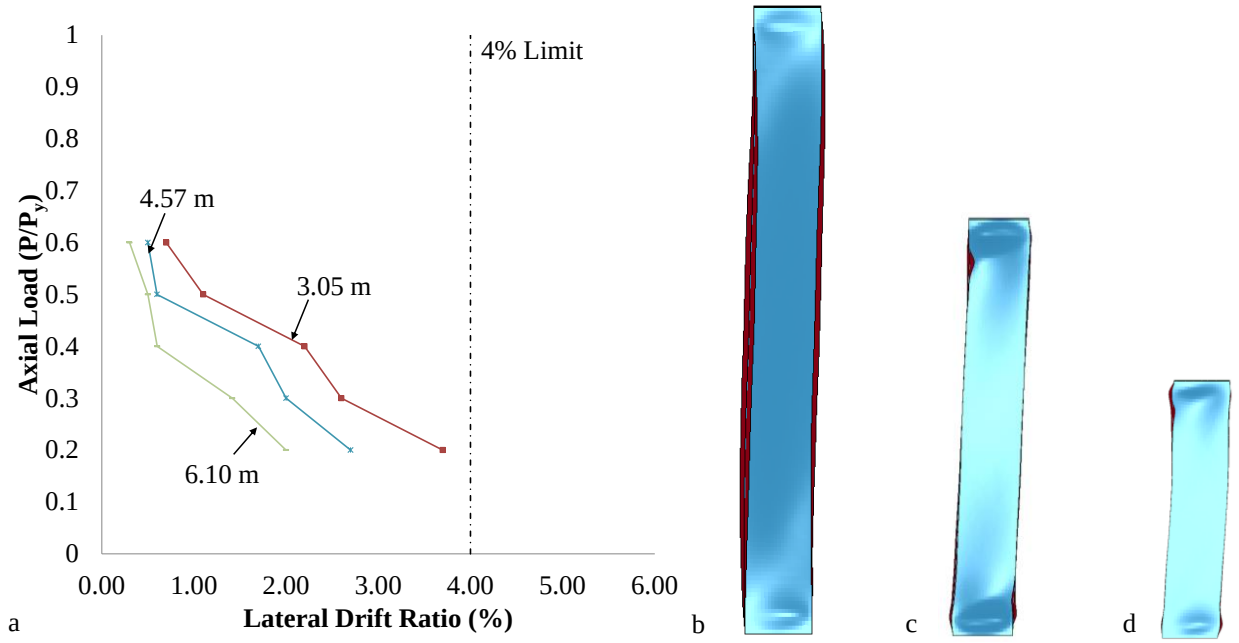

Figure 3-15. Axial load of W24x176 column versus (a) lateral drift ratio at moment failure criterion as well as column displaced shape (2x magnified) at moment failure for W24x176 with *P/Py* = 0.40 for unbraced lengths (b) 6.10 m, (c) 4.57 m, and (d) 3.04 m

3.6.4 Regression Analysis

Using the CALR for each section based on the axial load failure criterion a multivariable regression analysis is undertaken to determine which factors influence the amount of load a column section is able to carry up to 4% lateral drift. The data input into the regression model is shown in Table 3-2.

Since it is clear that the width-to-thickness ratios alone do not adequately predict the capacity of sections under this combined loading scheme, a linear regression model is used to evaluate the potentially important parameters based on the behavior seen in the parametric study. The first two parameters, h/t_w and b/t, are already accounted for in the current guidelines, but the

additional terms are included to assess their influence on the CALR. Since columns under this loading scheme seem to exhibit significant twisting behavior after local buckling has begun, several terms that are involved with global buckling, particularly torsional behavior, are investigated. The third term, L/r_y, is used for calculating the nominal compressive strength due to flexural buckling and is very similar to the ratio of unbraced length to effective radius of gyration, L_b/r_{ts}, which is used to calculate the nominal flexural strength due to lateral-torsional buckling. Variations of the fourth term, $\sqrt{JI_y}/L^2$, can be found in solutions for the critical load at which a simply-supported beam will buckle laterally (Gambhir 2004) where J is the torsional constant, I_y is the moment of inertia about the y-axis, and L is the length. The fifth term, JS_x/h_0, is also used to calculate the nominal flexural strength due to lateral-torsional buckling where S_x is the elastic section modulus about the x-axis and h_o is the distance between the flange centroids. The final term is the torsional elastic stress, F_{ez}, and is used in the calculation of nominal compressive strength based on a torsional buckling limit state. These terms account for different variations of geometric properties that contribute to a section's ability to resist lateral or torsional behavior and a combination of one or more of these parameters along with the two parameters that are related to local buckling behavior are expected to enable the prediction of the CALR.

To predict the response variable (RV), the general linear model used is:

$$RV = b_1 + b_2 \log(X_1) + b_3 \log(X_2) + \ldots + b_n log(X_{n-1}) \qquad 3\text{-}2$$

Where b_i are regression coefficients and X_i are predictor variables. Using the predictor variables in conjunction with the response variable, P/P_y, the regression model can be written as:

$$\frac{P}{P_y} = b_1 + b_2 \log\left(\frac{h}{t_w}\right) + b_3 \log\left(\frac{b}{t}\right) + b_4 \log\left(\frac{L}{r_y}\right) + b_5 \log\left(\frac{\sqrt{JI_y}}{G}\right) + b_6 \log\left(\frac{JS_x}{h_o}\right) + b_7 \log(F_{ez}) \quad 3\text{-}3$$

Using backward elimination (Chaterjee et al. 2000) with standard t-tests until all the parameters are statistically significant at the 5% level results in h/t_w and L/r_y being the main parameters influencing the critical axial load. Equation 3-3 is reduced to the proposed regression model:

$$\frac{P}{P_y} = 2.6224 - 0.2037 \log\left(\frac{h}{t_w}\right) - 0.3734 \log\left(\frac{L}{r_y}\right) \quad 3\text{-}4$$

The coefficient of multiple determination for the linear regression of the CALR on h/t_w and L/r_y is estimated to be 0.722, which means that these two geometric parameters jointly explain 72.2% of the variation in the critical axial load ratio. While *b/t* has been deemed critical in predicting the behavior in the past, it is unsurprising that it is statistically insignificant based on the high amount of scatter seen in Figure 3-11. As mentioned previously, the current flange width-to-thickness ratio can be used to identify sections that are not highly ductile. However, members that meet the highly ductile limit can be evaluated using Equation 3-4 and the design aid described below, which is based on it.

3.7 EVALUATION OF CURRENT SEISMIC DESIGN GUIDELINES

The parametric study described above suggests that the current AISC guidelines are potentially unconservative and can be improved. The simulations indicate that CALR can be reasonably predicted by h/t_w and L/r_y provided *b/t* meets current design guidelines for highly ductile members. Instead of having separate limits as shown in Table 3-1, limits on the two ratios are interrelated and can be plotted as a family of curves, each based on a given CALR. Figure 3-16

shows plots for CALRs ranging from 30 to 80% along with the scatter of sections that achieved the associated CALR based on the finite element analysis.

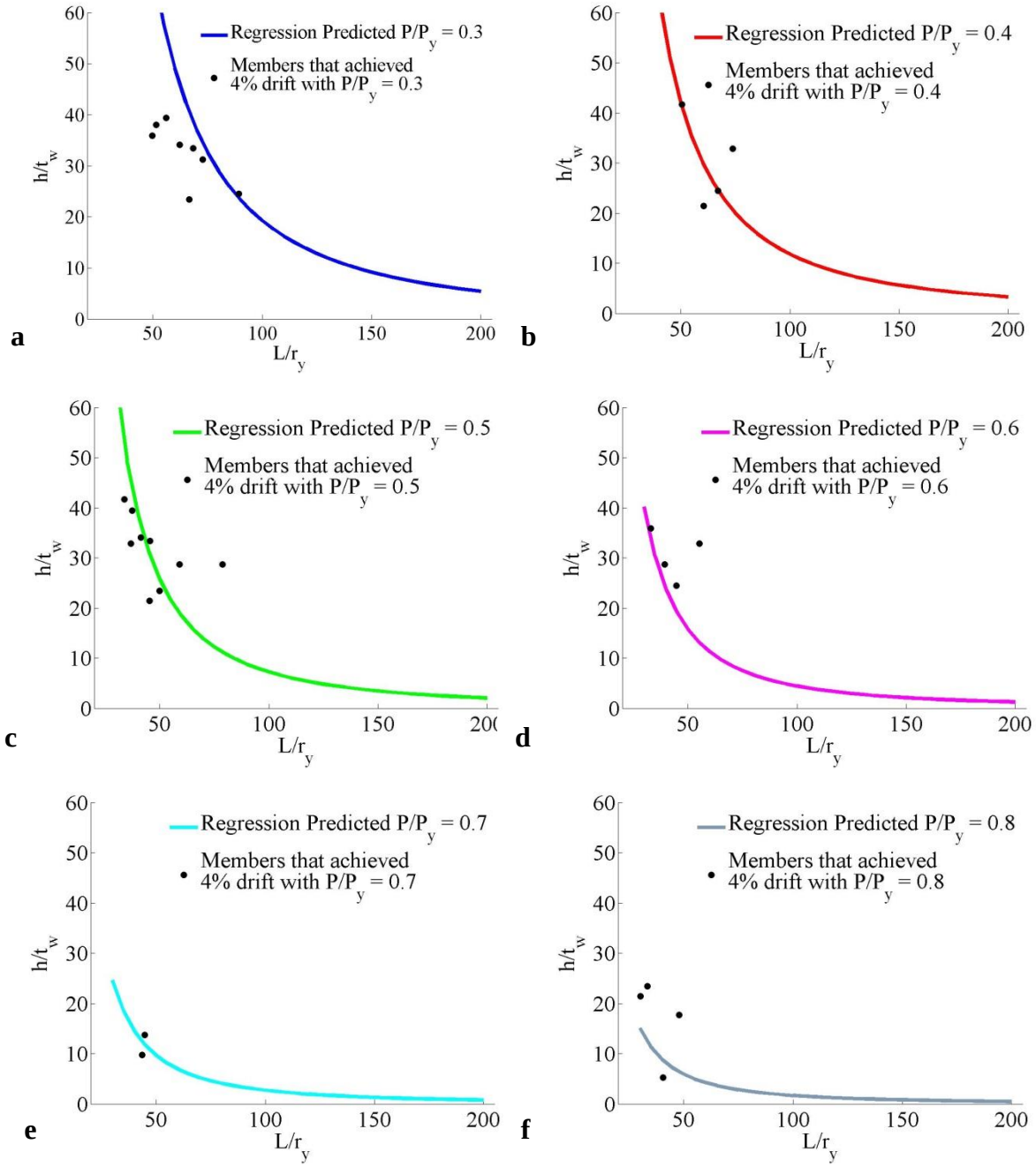

Figure 3-16. Solid curves for logarithmic expectation function plotted for a) P/P_y = 0.3, b) P/P_y = 0.4, c) P/P_y = 0.5, d) P/P_y = 0.6, e) P/P_y = 0.7, *f)* P/P_y = 0.8 along with corresponding critical axial loads for each section from finite element data.

The range for h/t_w is based on the maximum value of 57.5 (W30x90) for sections deeper than W16s and the range for L/r_y is based on columns ranging from 3.05 m to 6.10 m in length with radius of gyrations ranging from 28.4 mm (W16x26) to 104 mm (W36x652).

Sections that are unable to carry the lowest target axial load investigated up to a drift of 4% are also plotted in Figure 3-17. While these sections are not useful in performing the regression analysis, they are useful in evaluating the limit on the h/t_w as a function of L/r_y for sections that can serve as highly ductile members.

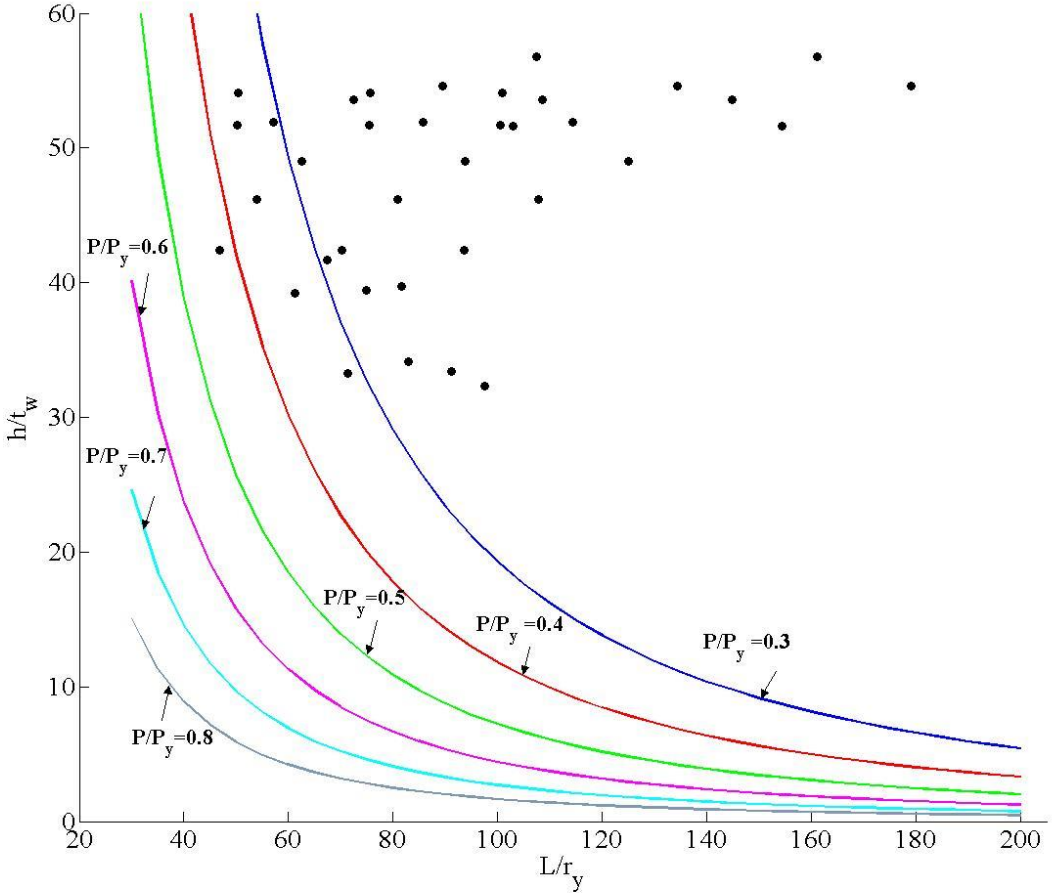

Figure 3-17. Comparison of members that could not sustain 0.2P_y up to 4% lateral drift (circles) with CALR prediction curves.

3.7.1 Design Aid

Figure 3-17 can also serve as a powerful design aid. A designer can enter the figure with their known h/t_w and L/r_y and determine up to what critical axial load ratio their column can be considered a highly ductile member. Based on the location of the section regarding the two geometric parameters, the closest line to the right should provide a reasonable approximation for the section's CALR.

To evaluate the usefulness of this guideline, six sections that are not used in the calibration of the model are analyzed using finite element models and compared to the expected values from the regression model. These findings are summarized in Table 3-5 and shown in Figure 3-18, where the selected sections are represented by solid squares with arrows pointing to the associated curve. In 4 of the 6 test sections, the equation provided the appropriate critical axial load ratio or a more conservative value compared to the finite element analysis. In two of these sections, the CALR was overestimated by $0.1P_{y.}$ This is unsurprising since the regression equation only accounts for approximately 70% of the variation in the CALR and there is clearly scatter in the data, which could possibly be considered within a probabilistic design frameworks. Regardless, the proposed process does provide a more reasonable estimate for the actual CALR and behavior of deeper sections than the current seismic member design guidelines as seen by the much smaller difference between the expected and actual critical axial loads when comparing Table 3-5 with Table 3-2.

Table 3-5. Evaluation of plotted regression using test sections.

Section	$\frac{h}{t_w}$	$\frac{L}{r_y}$	*Expected CALR* (*Figure* 14)	*Actual CALR* (*FE*)
TYPE I				
W18x211	15.1	63.8	0.5	0.5
W24x162	30.6	59.0	0.4	0.5
W36x652	16.3	43.9	0.6	0.5
W36x652	16.3	52.7	0.5	0.5
W40x324	34.2	50.3	0.4	0.3
TYPE II				
W30x148	41.6	79.0	NHD*	NM**

*Not Highly Ductile (NHD) member based on proposed design guide

**CALR is Not Measured (NM) since section did not reach 4% drift under $0.20P_y$

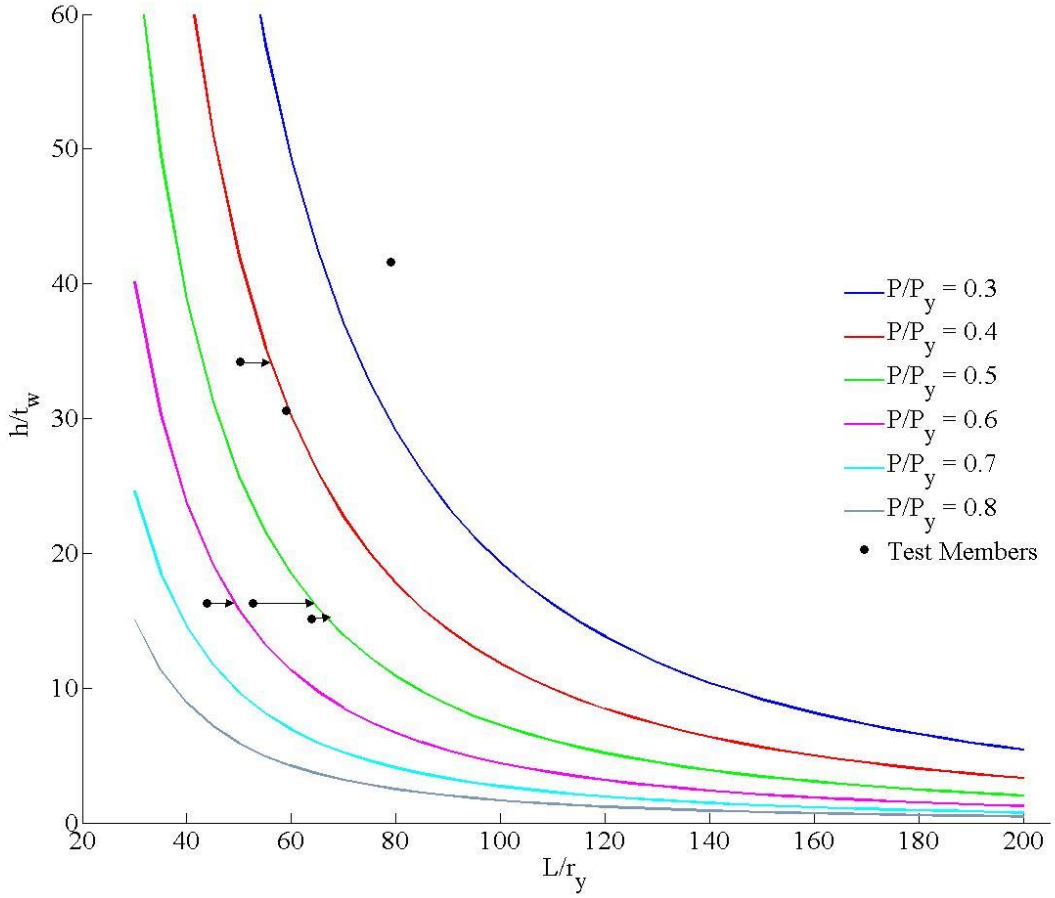

Figure 3-18. Plots of the test members with arrows indicating the predicated CALR based on the regression equation.

3.8 CONCLUSIONS

The behavior of steel wide flanged beam-columns is investigated under a combined axial and monotonic lateral loading scheme. Results from the parametric study indicate that local buckling and lateral torsional buckling are reducing the column strength significantly at lateral drift levels below 4% despite the fact that many of the columns studied can be classified as highly ductile members based on current AISC Seismic Design requirements. This is concerning since the overturning effects can easily magnify a gravity load of $0.15P_y$. Of the 57 members studied that can be considered highly ductile, only 32 of them were able to support a CALR of 0.20 or higher up to 4% drift. This value drops to 24 members when the CALR is 0.40 indicating that approximately half of the members that can be considered highly ductile based on current specifications cannot reach 4% lateral drift under axial loads ($0.20P_y$ to $0.40P_y$) that are feasible during a seismic event. The studied columns indicate that h/t_w has a more significant effect on the strength of the column under the combined loading scheme than b/t when the current AISC flange width-to-thickness ratio highly ductile limit is satisfied. L/r_y also plays a significant role in predicting the CALR and can be seen by changes in the failure mode of different length members. The dominant buckling mode shifts from local buckling to lateral torsional buckling with increasing unbraced length. An evaluation of the current AISC Seismic Design guidelines suggests that the provisions are potentially unconservative. It is suggested that improvements can be made to the guidelines based on the results of this study and a design aid is provided. Additional investigations concerning boundary conditions and additional cyclic loading protocols are necessary to ensure the design aid is adequate for predicting the behavior of all column members used in seismic force resisting systems.

CHAPTER 4

BEHAVIOR OF STEEL COLUMNS SUBJECTED TO COMBINED AXIAL AND MONOTONIC LATERAL LOADING

4.1 GENERAL

This chapter investigates the parameters influencing the amount of axial load a member can support up to different drift levels, under monotonic lateral loading, using analytical and computational methods. The Rayleigh-Ritz method is used to qualitatively address the influence of the amount of buckling along the length, the amount of buckling within the cross-section, as well as the influence of the web and flange width-to-thickness ratios. A regression analysis is performed on the results of computational members that have undergone monotonic lateral loading under target compressive forces to determine which parameters are statistically significant. Additionally, members are subjected to various initial axial loads, displaced to a specified drift and loaded until failure to determine the effect that initial axial load, axial shortening, and local buckling effects play in predicting the failure mode and axial resistance of the member.

4.2 ANALYTICAL MODELING

A variational approach is used to investigate the potentially important parameters that are affecting the amount of axial load a member can support up to different drift levels. The critical load of a cantilever column that has been damaged by lateral loading near the base of the member can be determined analytically using the Rayleigh-Ritz method with the following assumptions:

- Buckled (damaged) portions of the flanges are unable to support axial load and are removed from the cross-section.
- Damage (due to buckling) is symmetric about the web on the flange being compressed due to the lateral load.
- Damaged part does not affect the assumed deformed shape.
- Elastic behavior

4.2.1 Formulating the Problem

A prototype column is considered to be comprised of 2 segments of different lengths: 1) a damaged portion at one end, in which the buckled flanges are considered to be present or partially present, and 2) the remaining length which is considered an intact segment. This column is loaded as shown in Figure 4-1**Error! Reference source not found.** simultaneously with both an axial load, P_1, and a lateral load, P_2.

The damaged cross-section may no longer be bi-symmetric, but remains at least mono-symmetric and thus has an effective eccentricity, *e*, associated with the axial load. This shift in the section's centroid due to flange 'loss' is shown in Figure 4-2 where v_L, u_L, and β_L, are the lateral displacement in the y-axis, the lateral displacement along the x-axis, and the angle of twist about the z-axis respectively at the tip of the cantilever. The resulting end moment equations shown in Figure 4-2 are further clarified in Figure 4-3 by showing the displacements and applied force components along the original axes resulting from the deformed configuration.

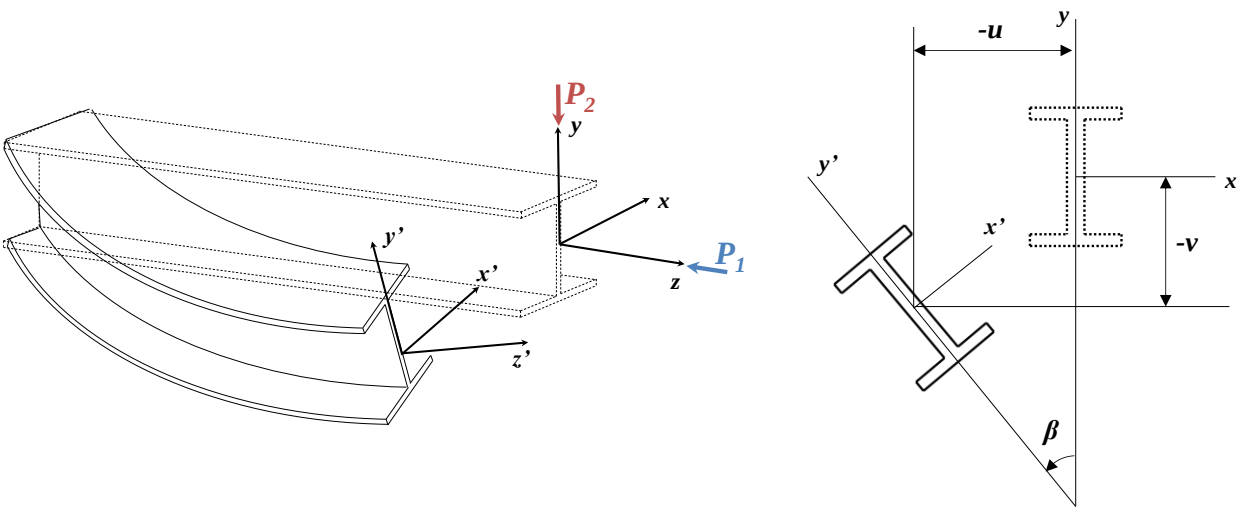

Figure 4-1. Deformation of member under combined loading scheme

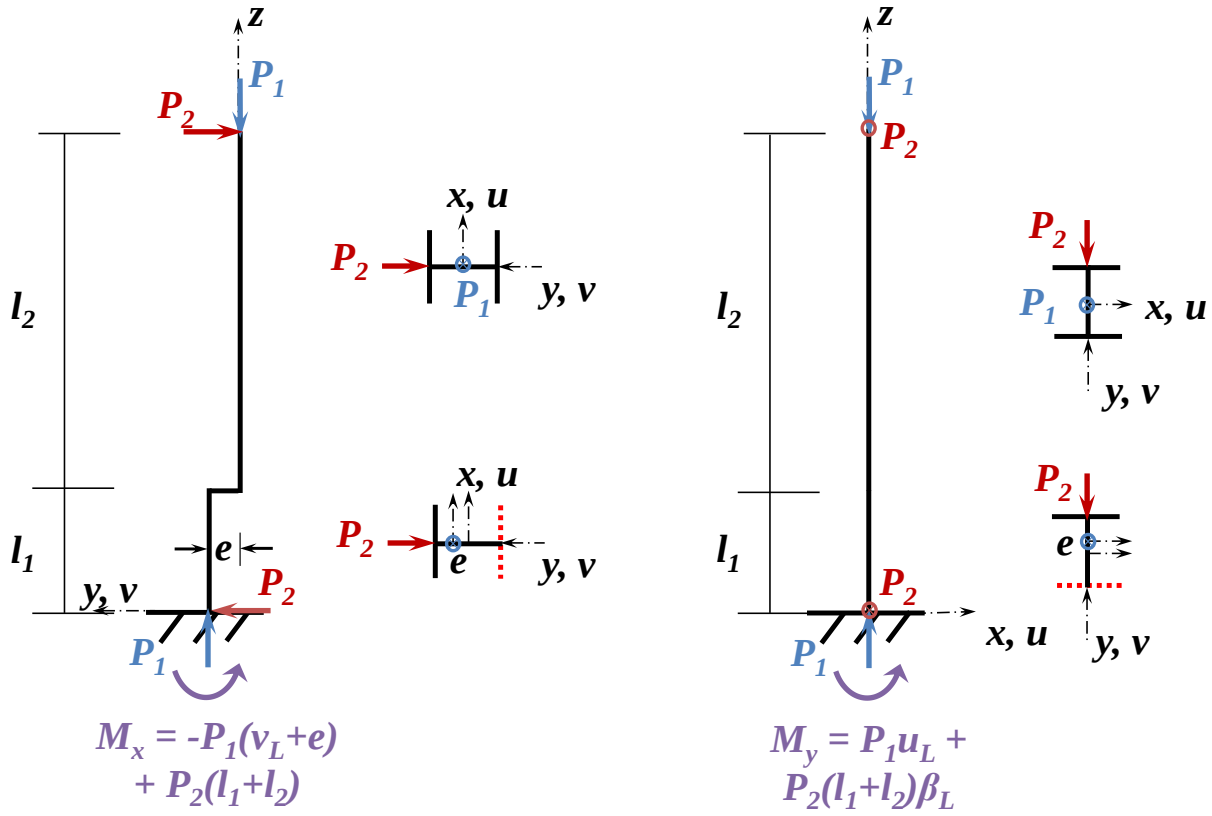

Figure 4-2. Centerline of column where the centroid of the bottom segment is shifted due to damage and cross-section illustrating section with damaged flange

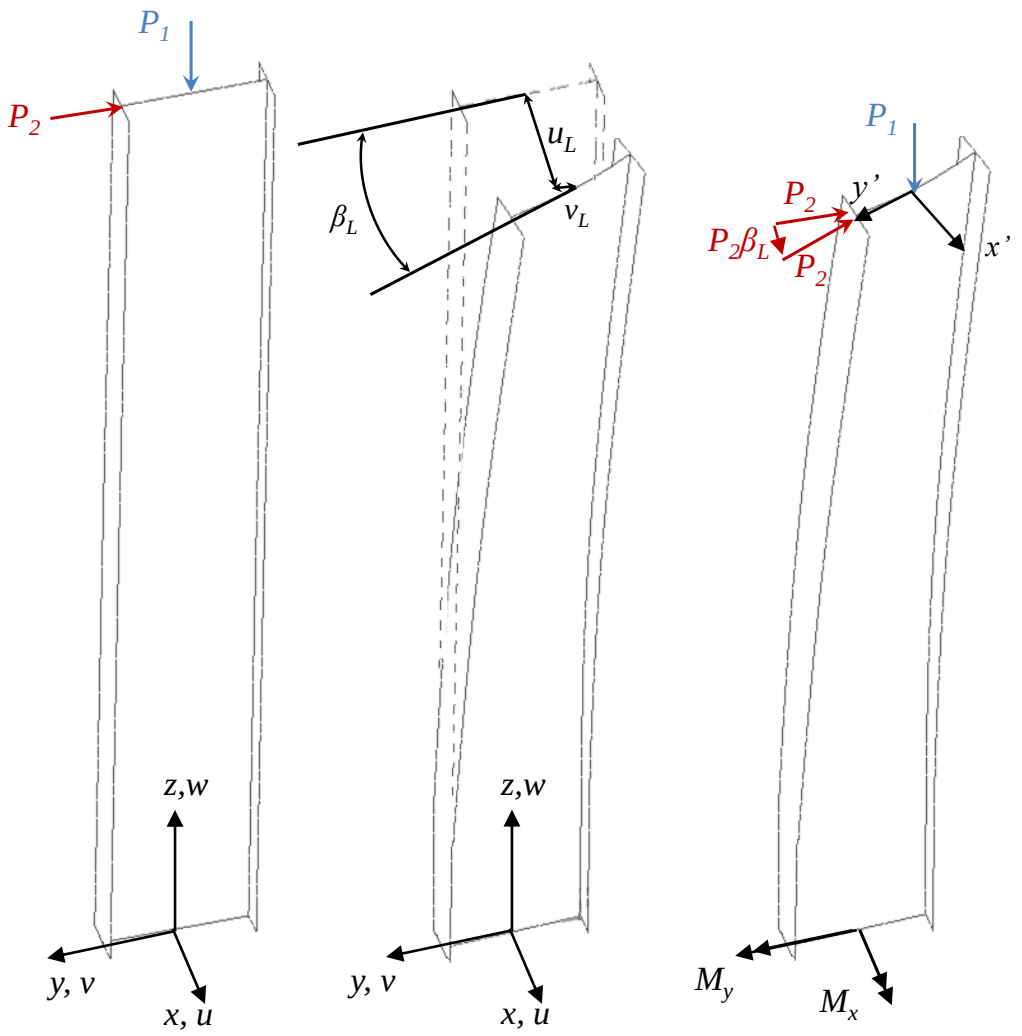

Figure 4-3. Buckled shape and resulting moments due to displacement (P_1) and rotation (P_2) of tip loads

A variational approach utilizing the Rayleigh-Ritz method is employed to identify the most influential parameters on the axial capacity of the steel column. Using the Rayleigh-Ritz (R-R) method, an energy functional, representing stored strain energy, for a column with total length L can be written as:

$$\Pi_p = \frac{1}{2}\int_0^L EAw_z^2 dz + \frac{1}{2}\int_0^L EI_y u_{zz}^2 dz + \frac{1}{2}\int_0^L EI_x v_{zz}^2 dz + \frac{1}{2}GJ\int_0^L \beta_z^2 dz + \frac{1}{2}EC_w\int_0^L \beta_{zz}^2 dz - P_2\int_0^L \beta(L-z)u_{zz}dz - P_1 \cdot w(L) - \frac{P_1}{2}\int_0^L (u_z^2 + v_z^2 + r_o^2\beta_z^2 - 2y_o v_z\beta_z + 2x_o u_z\beta_z)dz \quad \text{4-1}$$

Where L is the total member length, E is the modulus of elasticity, I_x and I_y are the moments of inertia, A is the cross-sectional area, w is the axial displacement, v is the lateral displacement in the y-direction, u is the lateral displacement in the x-direction, β is the angle of twist about the z-axis, x_o and y_o are the coordinates of the centroid of the section, r_o is the polar radius of gyration with respect to the shear center, P_1 is the applied axial load, P_2 is the applied lateral load, J and C_w are torsional variables, and a *subscript* on a displacement variable implies differentiation with respect to the subscript.

The potential energy functional consists of the following terms: 1) axial strain energy, 2) bending strain energy about the y-axis, 3) bending strain energy about the x-axis, 4) strain energy due to St. Venant torsion, 5) strain energy due to warping, 6) external work from the lateral load, 7) external work from axial shortening due to the axial load, and 8) external work from lateral displacement and rotation due to the axial load.

Thus, the equation to describe the damaged column shown in Figure 4-2, where the total length is divided into two lengths, l_1 *and* l_2, and the subscript *d* refers to damaged section properties, can be written as:

$$\Pi_p = \frac{1}{2}\int_0^{l_1} EA_d w_z^2 dz + \frac{1}{2}\int_{l_1}^{L} EA w_z^2 dz + \frac{1}{2}\int_0^{l_1} EI_{yd} u_{zz}^2 dz$$
$$+ \frac{1}{2}\int_{l_1}^{L} EI_y u_{zz}^2 dz + \frac{1}{2}\int_0^{l_1} EI_{xd} v_{zz}^2 dz + \frac{1}{2}\int_{l_1}^{L} EI_x v_{zz}^2 dz$$
$$+ \frac{1}{2} GJ_d \int_0^{l_1} \beta_z^2 dz + \frac{1}{2} GJ \int_{l_1}^{L} \beta_z^2 dz + \frac{1}{2} EC_{wd} \int_0^{l_1} \beta_{zz}^2 dz$$
$$+ \frac{1}{2} EC_w \int_{l_1}^{L} \beta_{zz}^2 dz - P_2 \int_0^{L} \beta(L-z) u_{zz} dz - P_1 \cdot w(L) \qquad \text{4-2}$$
$$- \frac{P_1}{2}\int_0^{l_1} (u_z^2 + v_z^2 + r_{od}^2 \beta_z^2 - 2y_{od} v_z \beta_z + 2x_{od} u_z \beta_z) dz$$
$$- \frac{P_1}{2}\int_{l_1}^{L} (u_z^2 + v_z^2 + r_o^2 \beta_z^2 - 2y_o v_z \beta_z + 2x_o u_z \beta_z) dz$$

4.2.2 Solving the Problem

Since this specific loading case is not available in the literature, simpler loading cases are evaluated using this equation to determine if the equation can produce reasonable values. To this end, the lateral buckling load of a cantilever, flexural buckling load of a cantilever, and the lateral buckling moment for a simply supported beam under pure bending are all investigated. The well-known and "correct" solutions found in Chajes (1974) and Chen and Lui (1987) were obtained using Equation 4-2 for these simplified cases indicating that this method is providing meaningful results.

An additional set of coordinate axes *x', y',* and *z'*, which are relative to the deformed shape of the member, are introduced to account for the various moments that result from the applied loading in the deformed configuration. The angle relations between the deformed axes (*x',y',z'*) and the original axes (*x,y,z*) are shown in Figure 4-4. The moments $M_{x'}$, $M_{y'}$, and $M_{z'}$ are the components of the moment resulting from the applied lateral and axial loads about the *x', y',* and *z'* axes.

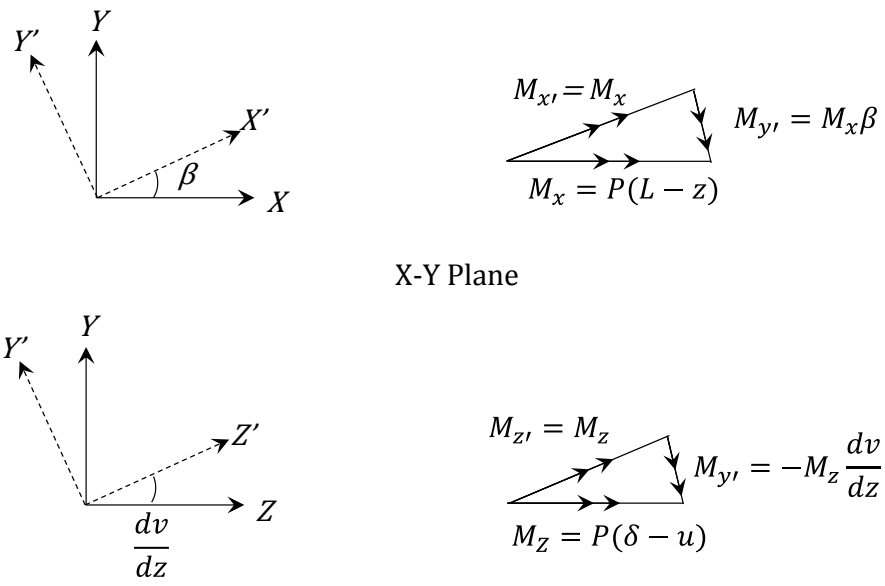

Figure 4-4. Moment Components in X-Y and Y-Z planes

Chen and Lui (1987) made the following simplifying assumption with respect to $M_{y'}$ in the case of a cantilever with a lateral load that allowed them to express the strain energy in terms of only one variable, β, :

$$M_{y'} = \beta P(L-z) - \frac{dv}{dz}P(\delta - u) \qquad 4\text{-}3$$

$$M_{y'} \approx \beta P(L-z) \qquad 4\text{-}4$$

Since this moment can also be expressed as:

$$M_{y'} = EI_y\frac{d^2u}{dz^2} \qquad 4\text{-}5$$

Equations 4-4 and 4-5 can be equated to obtain an expression for the second derivative of the lateral displacement, *u*:

$$\frac{d^2u}{dz^2} = \frac{\beta P}{EI_y}(L - z) \tag{4-6}$$

However, this simplification is not feasible in the combined case due to the inclusion of higher order derivatives of the lateral displacement, *u*, from the work done by the axial load in the strain energy functional. Therefore, approximations for both *u* and β must be determined that satisfy the kinematic boundary conditions and provide a reasonable critical buckling load.

For the cantilever, the essential boundary conditions for the variables consist of the following:

$$\beta|_{z=0} = 0 \text{ and } \frac{d\beta}{dz}|_{z=L} = 0 \tag{4-7}$$

$$u|_{z=0} = 0 \text{ and } \frac{d^2u}{dz^2}|_{z=0} = 0 \tag{4-8}$$

$$v|_{z=0} = 0 \text{ and } \frac{d^2v}{dz^2}|_{z=0} = 0 \tag{4-9}$$

$$w|_{z=0} = 0 \tag{4-10}$$

Where $z = 0$ is the fixed end where no rotation or displacement occurs and the constraint on $z = L$ in Equation 4-7 implies that the St. Venant torsion is not present at the free end.

The combinations of approximations listed in Table 4-1 were investigated in the lateral load buckling case and compared with the critical load coefficient of 4.183 obtained by Chen and Lui (1987) with their simplifying assumption. Based on the obtained critical loads, it is clear that the solution is very sensitive to the approximate shapes. While an answer similar to the one obtained by Chen and Lui (1987) can be found with unrelated approximations for *u* and *β,* it requires excessive calculation for minimal gain. Since the concern is to understand what role the key variables play in affecting the capacity of the damaged column, a simpler approximation is

considered reasonable enough and allows for more easily attainable results. While the polynomial approximation in trial 3 yields a slightly better value than the sinusoidal curve in trial 2, the sinusoidal curve is selected due to the fact that it obtains the exact solution in the flexural buckling load case for the cantilever.

Table 4-1. Deflected shape functions.

Trial	β approximation	u approximation	Critical Load Coefficient
1	$\frac{A}{L^2}(2Lz - z^2)$	$Bsin\left(\frac{\pi z}{2L}\right)$	5.19
2	$\frac{A}{L^2}(2Lz - z^2)$	$B\left(1 - cos\left(\frac{\pi z}{2L}\right)\right)$	4.67
3	$\frac{A}{L^2}(2Lz - z^2)$	Bz^2	4.62
4	$\frac{A}{L^2}(2Lz - z^2)$	$Bz^2 + Cz^3$	4.58
5	$\frac{A}{L^2}(2Lz - z^2)$	$Bz^2 + Cz^3 + Dz^4$	4.19
6	$\frac{A}{L^2}(2Lz - z^2)$	$Bz^2 + Cz^3 + Dz^4 + Ez^5$	4.18
7	$\frac{A}{L^2}(2Lz - z^2)$	$Bz^2 + Cz^3 + Dz^4 + Ez^5 + Fz^6$	4.18
8	$\frac{A}{L^2}(2Lz - z^2)$	$Bz^3 + Cz^4$	4.51
9	$\frac{A}{L^2}(2Lz - z^2) + Bz^3$	$Cz^2 + Dz^3$	4.67

Given Equation 4-2 and the chosen approximations for the deflected shape shown in Equations 4-11 through 4-14, the desired critical load occurs when the functional has a stationary value.

$$\beta = \frac{A}{L^2}(2Lz - z^2) \tag{4-11}$$

$$u = B(1 - cos\left(\frac{\pi z}{2L}\right) \tag{4-12}$$

$$v = C(1 - cos\left(\frac{\pi z}{2L}\right) \tag{4-13}$$

$$w = Dz \tag{4-14}$$

Since this occurs when the partial derivatives of the functional with respect to these four variables vanish, a set of linear homogenous equations can be obtained by setting these derivatives equal to zero. A nontrivial solution for a relation between the axial and lateral critical loads can be found, but does not provide a relation between the axial load and lateral displacement.

4.2.3 Obtaining Load Deflection Curves

To obtain a load deflection curve in the same manner as was done in the non-torsional case in Chapter 2, an initial imperfection through a change in geometry or small load needs to be included. The second term is recast as follows.

$$\frac{1}{2}\int_0^L EI_x v_{zz}^2 dz = \frac{1}{2}\int_0^L \frac{{M_x}^2}{EI_x} dz = \frac{1}{2}\int_0^L \frac{(P \cdot v)^2}{EI_x} dz \tag{4-15}$$

This is not only a simpler representation, but also takes advantage of the fact that utilizing a function instead of a derivative of the function generally results in a smaller error (Chen and Lui 1987). This also allows for the direct incorporation of the eccentricity, *e:*

$$\frac{1}{2}\int_0^L \frac{(P \cdot (v + e))^2}{EI_x} dz \tag{4-16}$$

Since the flexural behavior about the strong axis is uncoupled from the lateral buckling action in small displacement analysis, an additional load is added to the potential energy function to

initiate deflection in the weak axis and twisting about the longitudinal axis. Equation 4-1 can be modified to account for these issues so that:

$$\begin{aligned}\Pi_p = \frac{1}{2}\int_0^L EAw_z^2 dz + \frac{1}{2}\int_0^L EI_y u_{zz}^2 dz + \frac{1}{2}\int_0^L \frac{(P_1 v)^2}{EI_x} dz + \frac{1}{2}GJ\int_0^L \beta_z^2 dz \\ + \frac{1}{2}EC_w\int_0^L \beta_{zz}^2 dz - P_2\int_0^L \beta(L-z)u_{zz} dz - P_1 w(L) \\ - \frac{P_1}{2}\int_0^L (u_z^2 + v_z^2 + r_o^2\beta_z^2 - 2y_o v_z\beta_z + 2x_o u_z\beta_z) dz - P_I\, u(L)\end{aligned} \quad 4\text{-}17$$

Where P_I is the load in the direction of *x*-axis (lateral displacement *u*) and is taken as a small value ($P_I < 1$).

Splitting this equation as was done in Equation 4-2 and setting the derivatives with respect to each Rayleigh variable equal to zero allows for a nontrivial solution of the Rayleigh variables.

Substituting these values into the assumed approximations for the lateral displacements and twisting of the section produces a plot of the critical load as a function of the lateral displacement The case is simplified to the lateral load and axial load only solutions to check with available solutions in the literature and the plots below are given for a W14x120 column.

Setting $P_1 = 0$ and solving for P_2 once the values for the Rayleigh variables, *A* and *B*, have been substituted back into Equation 4-11 and 4-12 gives the plot in Figure 4-5 where the asymptote is given in Equation 4-18. This is the lateral buckling load for a cantilever with a transverse tip load and no axial load.

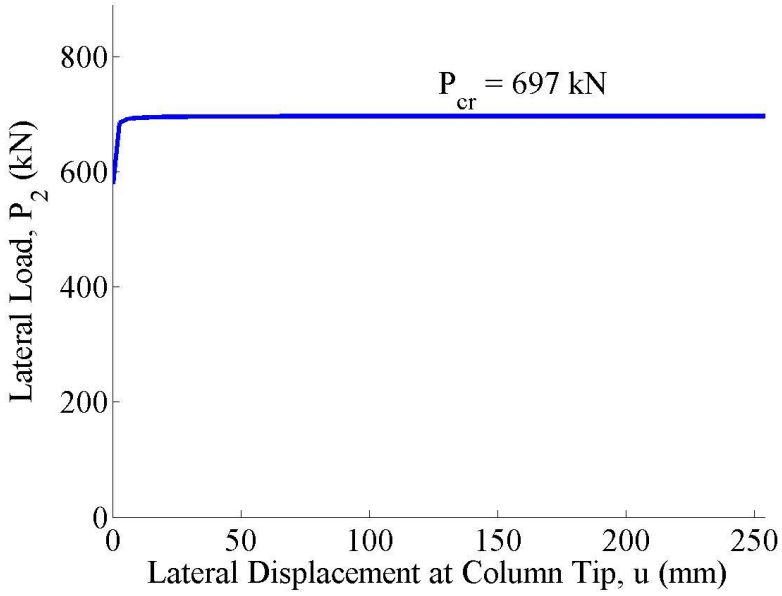

Figure 4-5. Lateral load P_2, versus lateral displacement, u. Asymptote at Equation 4-18.

$$P_{cr} = \frac{4.67\sqrt{EI_y(GJL^2 + 3EC_w)}}{L^3} \qquad 4\text{-}18$$

The asymptotes for the axial load versus the lateral deflection, v, when $P_2 = 0$ are shown for the pure flexural buckling loads and pure torsional buckling load in Figures 4-6, 4-7, and 4-8 respectively, given by the following equations. These are the solutions for an axially compressed cantilever with no transverse tip load.

$$P_{cr} = P_y = \frac{\pi^2 EI_y}{4L^2} \qquad 4\text{-}19$$

$$P_{cr} = P_x = \frac{\pi^2 EI_x}{4L^2} \qquad 4\text{-}20$$

$$P_{cr} = P_\phi = \frac{1}{r_o}(GJ + \frac{3EC_w}{L^2}) \qquad 4\text{-}21$$

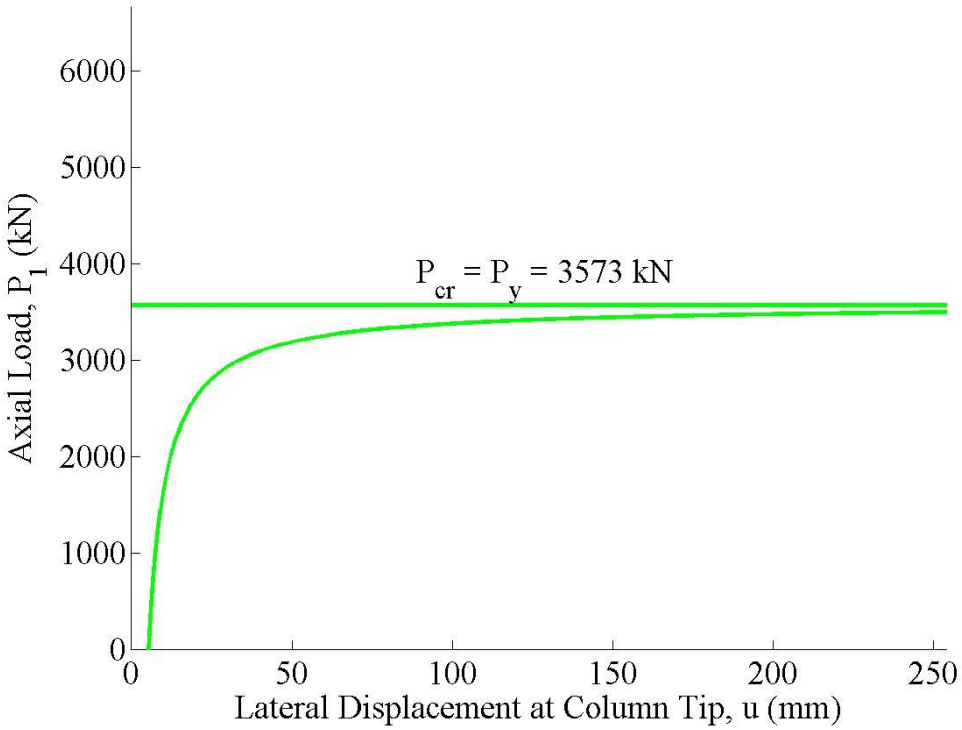

Figure 4-6. Axial load, P_1, versus lateral displacement, u. Asymptote at $P_{cr} = P_y$.

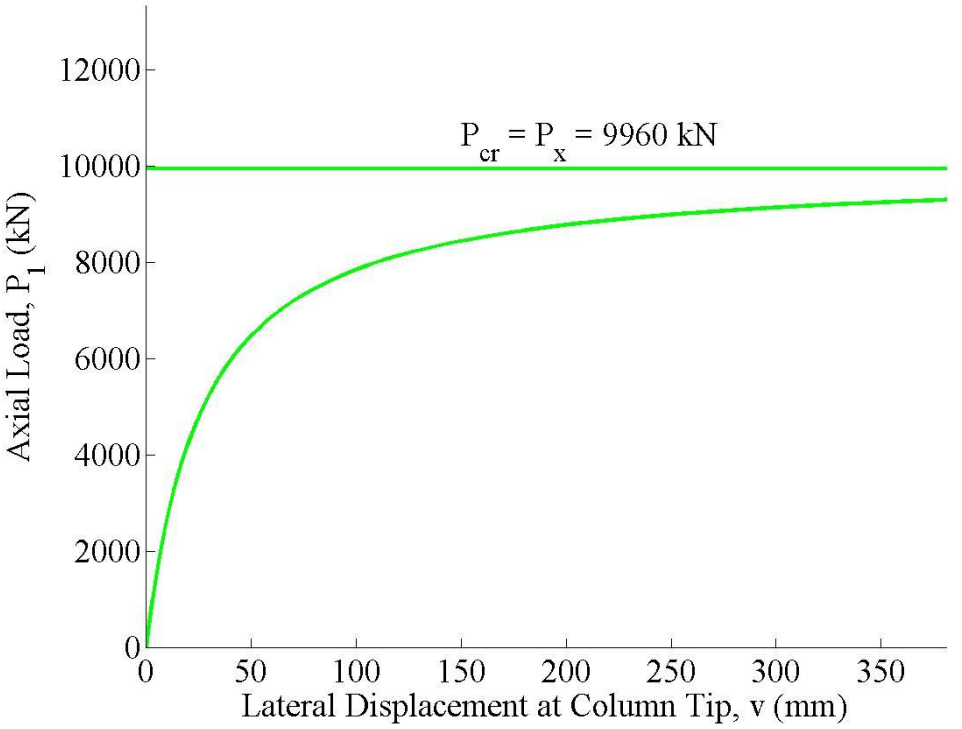

Figure 4-7. Axial load, P_1, versus lateral displacement, v. Asymptote at $P_{cr} = P_x$.

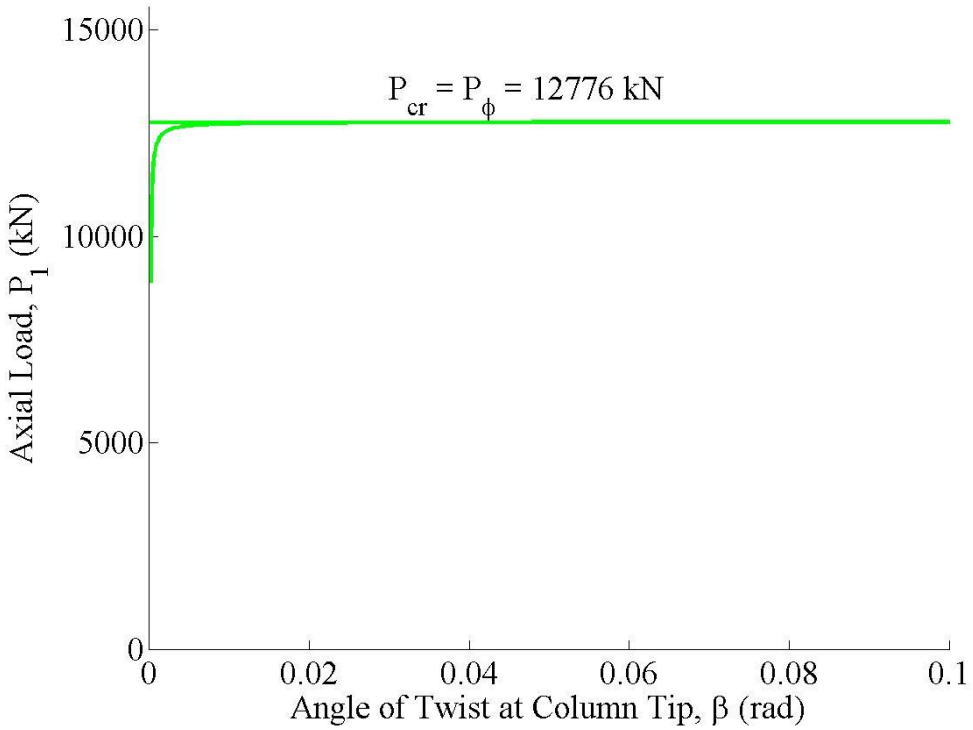

Figure 4-8. Axial load, P_1, versus angle of twist, β. Asymptote at $P_{cr} = P_{\varphi}$

4.2.4 Strength Curve

The previous derivations pertain to elastic stability only and do not account for the inelastic behavior of the column. Using simple plastic analysis and enforcing the AISC-LRFD (2013) moment versus axial load interaction relationship in (4-22), the relation between applied axial load, P_1, and the variables used to describe the displaced shape is derived as shown in (4-25), where v_0 and u_0 are the initial column imperfections and M_{pxd} and M_{pyd} are the plastic moment capacities of the end (damaged) segment.

$$\frac{P_1}{A_d f_y} + \frac{8}{9}\left(\frac{M_x}{M_{pxd}} + \frac{M_y}{M_{pyd}}\right) = 1.0 \qquad 4\text{-}22$$

$$M_x = -P_1 * (v + e + v_0) + P_2 L \qquad 4\text{-}23$$

$$M_y = P_1 * (u + u_0) + P_2 L\beta \tag{4-24}$$

$$P_1 = -\frac{A_d f_y (M_{pyd}(9M_{pxd} + 8P_2 L) + 8M_{pxd} P_2 L\beta)}{9M_{pxd} M_{pyd} + 8(A_d f_y M_{pyd}(v + e + v_0) + M_{pxd}(u_o + u))} \tag{4-25}$$

Equation 4-25 is plotted in Figure 4-9 for a 5.3 m W30x124 column with 33% of the flange removed. Assuming no interaction between elastic stability response and inelastic behavior, the intersection of the strength and stability curves is an approximation for the capacity of the column. The strength curve for the lateral displacement in the y-direction, *v*, is plotted assuming the lateral displacement in the x-direction, *u*, and rotation, β, are zero while *v* and β are assumed zero for plots of the lateral displacement, *u*.

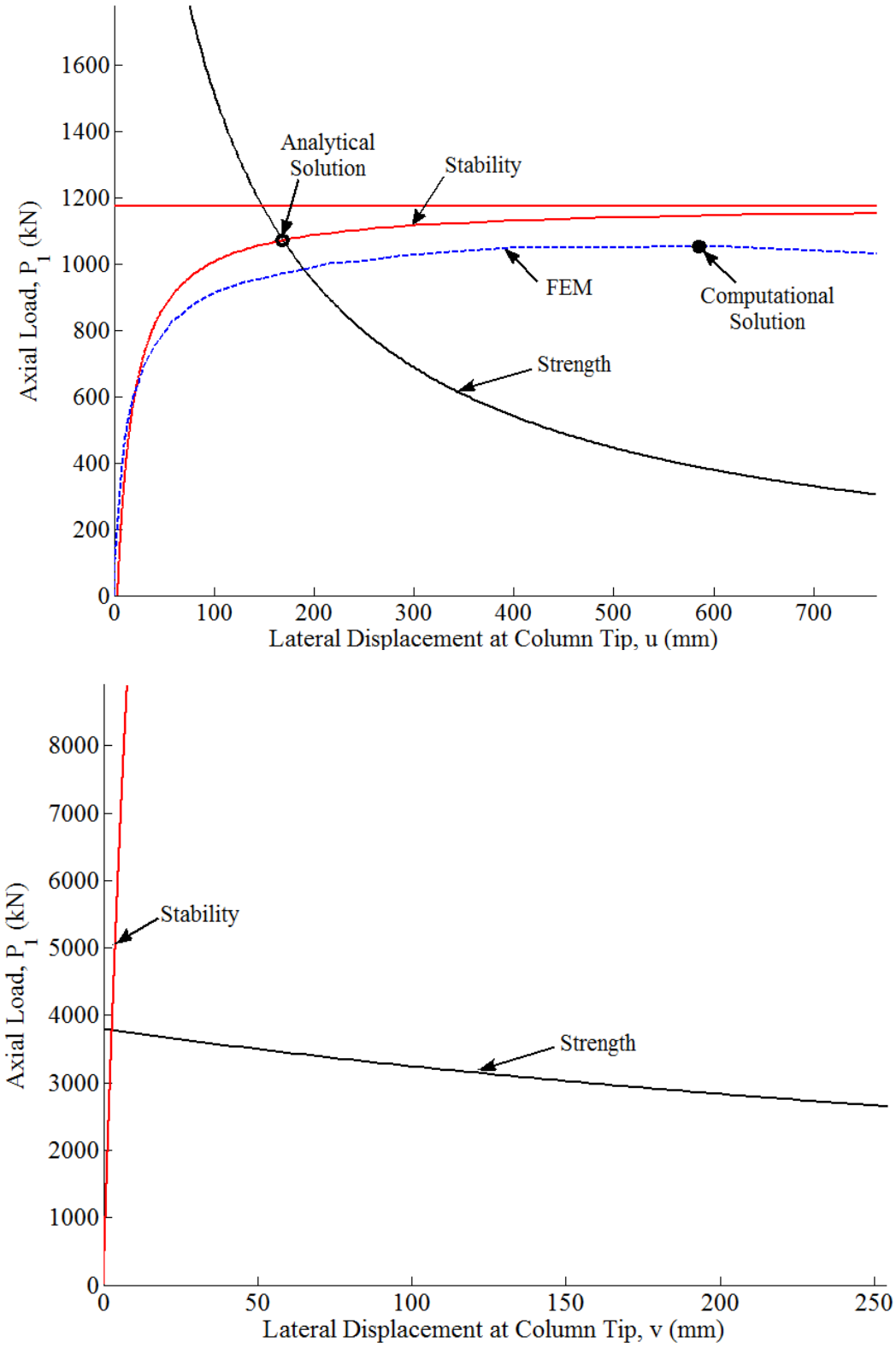

Figure 4-9. Strength and stability curves for W30x124-W33

While the rotation of the member is included in the strength equation through (4-24), the magnitude of the rotation is very small relative to the lateral displacements. The rotation is also highly dependent on their values since it is only triggered once the member has laterally displaced (i.e. setting *v* and *u* equal to zero does not yield meaningful results). Therefore, the role of flexural-torsional effects will be investigated through finite element studies.

While the torsional behavior may play a significant role, the asymptotes calculated using Equations 4-19 through 4-21 yield $P_{cr} = P_y$ as the lowest critical value for all cases, indicating the intersection of the strength and stability curves for P_1 versus the lateral displacement in the x-direction, *u*, will likely govern the capacity of the member.

4.2.5 Parametric Study

A W14x132 ($b/2t_f = 7.15$, $h/t_w = 17.7$, *and* $L/r_y = 55.9$), W18x119 ($b/2t_f = 5.31$, $h/t_w = 24.5$, and $L/r_y = 78.1$), and W30x124 ($b/2t_f = 5.65$, $h/t_w = 46.2$, *and* $L/r_y = 94.2$) were studied using this analytical model to determine the effect of various parameters on the capacity of the member. Parameters of interest include the amount of damage within the cross-section, the amount of damage along the length, and the plate slenderness ratios. In order to plot the stability and strength curves to determine the critical axial load, a lateral load (P_2) must be specified since the axial load (P_1) is a function of P_2 as is evident in Equation 4-25. A family of curves for the same damage and slenderness ratios is plotted below for lateral load values of 4.45 kN, 44.5 kN, and 90.0 kN to show the influence of the lateral load on the axial capacity of the member.

Since the concern is on the trends of the capacity due to the different parameters as opposed to the absolute magnitude, the capacity for each parameter has been normalized to the highest capacity of the member for that particular scenario. For the effect of damage within the cross-

section and damage along the length, the highest capacity occurs in the undamaged section when the lateral load is at its lowest (P_2 = 4.45 kN). When investigating the effect of flange and width thickness ratios, the most severe damage within the cross-section case was used throughout, so these capacities are normalized to the capacity of the section that looks like a T-beam for the lowest lateral load and original cross-section geometry. These particular highest capacities are referred to as P_{1u} for the intersection of the curves in the plots of P_1 versus u ($v=0$) and P_{1v} for the intersection of the curves in the plots of P_1 versus v ($u=0$).

4.2.5.1 Effect of Damage within Cross-section

The effect of monotonic loading is assumed to cause a significant portion of the flange in the damaged segment to buckle out of plane. Assuming these buckled flanges are unable to continue supporting any of the load, they are removed from the cross-section effectively creating a reduced flange width, b_f, to the point where the section may resemble a T-shape member as shown in Figure 4-10. Geometric properties based on various versions of this alteration to the cross-section are calculated and used for the member properties in the damaged segment for both the elastic stability and strength curves.

Damage occurring within the cross-section has a significant effect on the axial capacity as shown in Figure 4-10 and Figure 4-11. All three sections exhibit similar trends to that shown in Figure 4-10 for flexural buckling about the strong axis. The trends seen in Figure 4-11 show that the W14x132 is affected more by loss of the flange than the deeper sections. The strength curve drops more significantly for the compact section due to a more significant reduction in damaged segment cross-sectional area, A_d, and plastic section modulus, Z_{xd}. However, the W14x132 is less likely to see significant flange buckling due to the compact nature of its plate elements.

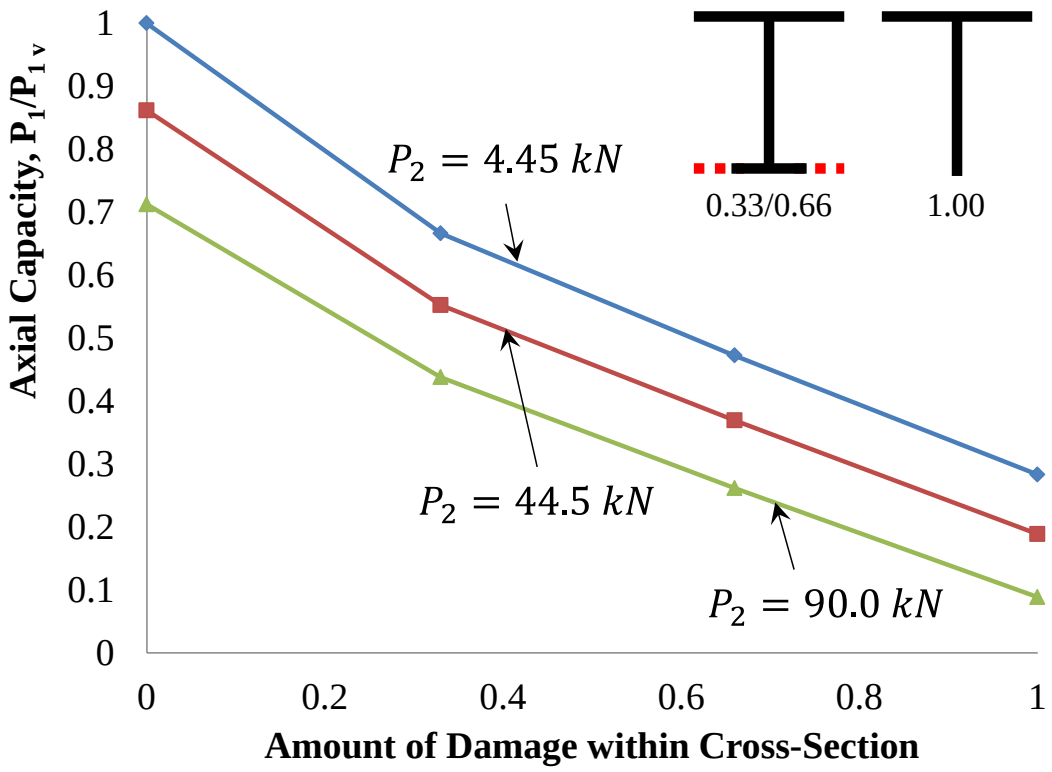

Figure 4-10. Axial capacity versus lateral displacement, *v*, for W18x119 under different lateral forces P_2 = 4.45 kN (diamonds), 44.5 kN (squares), and 90.0 kN (triangles) with damage length *d*

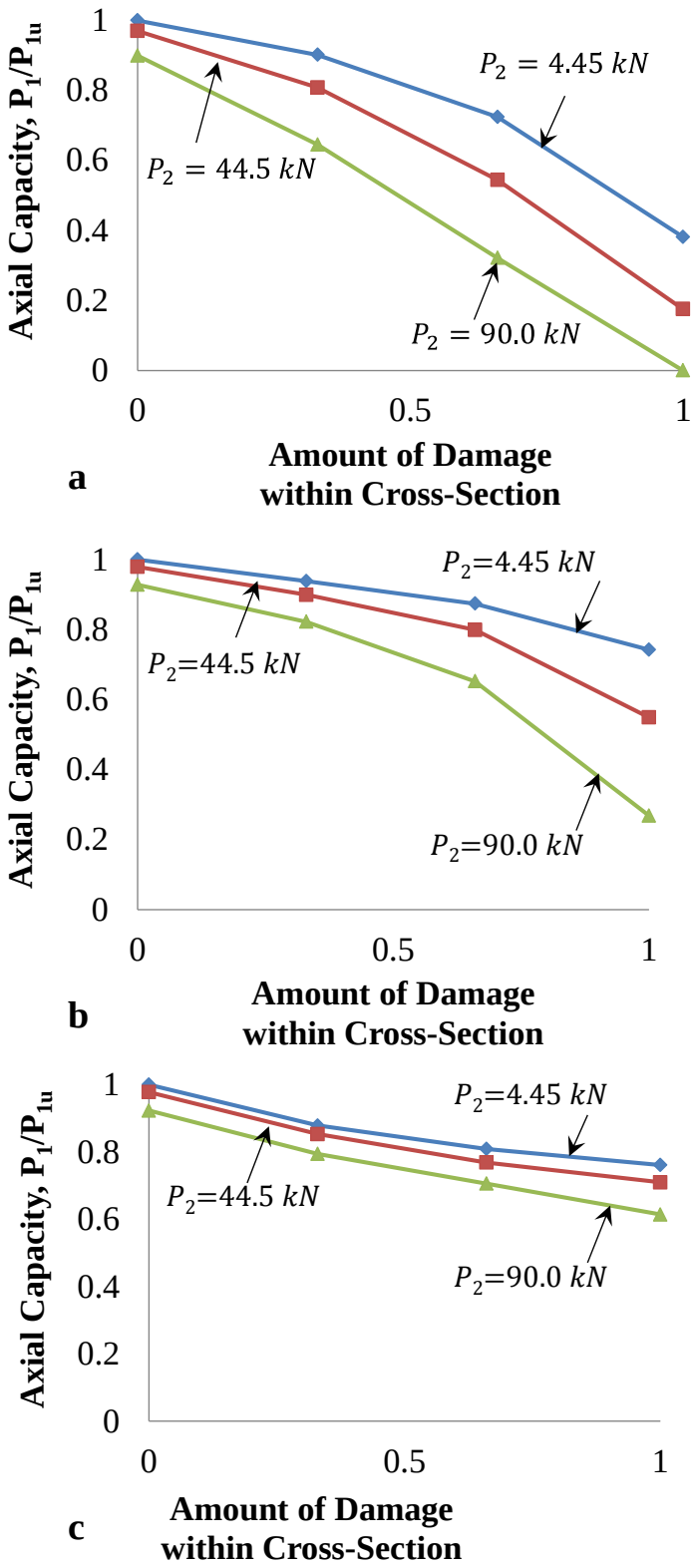

Figure 4-11. Axial capacity versus lateral displacement, *u*, for a) W14x132, b) W18x119, and c) W30x124 under different lateral forces P_2 = 4.45 kN (diamonds), 44.5 kN (squares), and 90.0 kN (triangles) with damage length *d*

4.2.5.2 Effect of Damage along Length

The length of the column over which local buckling is assumed to occur was varied from one-half to twice the depth of the member. This is based on recordings of the plastic hinge length for a combined axial and cyclic loading scheme as reported by Elkady and Lignos (2015). For all three sections, there was insignificant change in the amount of capacity due to changes in the length of the damaged segment. As shown in Figure 4-11, the difference is so slight that the points for the three different damage lengths overlap significantly for all the different cases of damage within the cross-section. Slight differences were observed for the weak-axis flexural buckling capacity, with the W30x124 experiencing the most significant difference as shown in Figure 4-12 where multiple capacities due to different damage lengths can be noted at each case of damage within the cross-section. This is consistent with the findings in Chapter 2 where the amount of damage along the length had little effect once any damage had occurred.

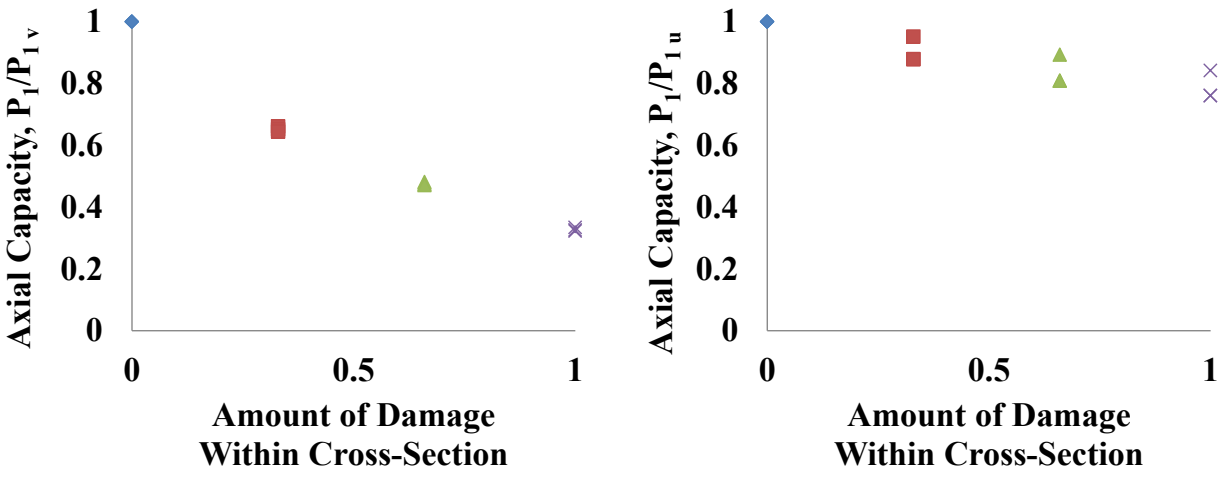

Figure 4-12. Effect of amount of damage along length for W30x124

4.2.5.3 Effect of Flange and Web Thickness

Since current seismic design guidelines are based on the flange and web width-to-thickness ratios, the flange and web thicknesses were halved and doubled to assess their effect on the axial

capacity of the member. Increasing the thickness of the plate elements increases the flexural capacity of the member in both directions as shown in Table 4-2. The flange thickness had a more significant impact on the weak axis buckling capacity for the two deep sections than the web thickness. Altering the flange thickness had the most significant impact on the W30x124 for both strong and weak-axis buckling. Altering the web thickness has a greater impact on the axial capacity for all three members than altering the flange thickness implying the web thickness is the more significant parameter. Several members are listed as having no axial capacity because the strength curve dropped so significantly due to the large lateral load and damaged section properties that there was no intersection with the elastic stability curve to record.

Table 4-2. Strong and weak axis capacities for different flange and web thicknesses

W14x132						
Lateral Load (kN)	4.45	44.5	90.0	4.45	44.5	90.0
Plate Thickness	Axial Capacity, P_1/P_{1v}			Axial Capacity, P_1/P_{1u}		
$1/2t_f$	0.79	0.35	0.00*	0.80	0.33	0.00*
t_f	1.00	0.44	0.00*	1.00	0.46	0.00*
$2t_f$	1.13	0.51	0.00*	1.21	0.53	0.00*
$1/2t_w$	0.52	0.00	0.00*	0.57	0.00	0.00*
t_w	1.00	0.44	0.00*	1.00	0.46	0.00*
$2t_w$	1.59	1.15	0.66	1.60	1.17	0.65

W18x119						
Lateral Load (kN)	4.45	44.5	90.0	4.45	44.5	90.0
Plate Thickness	Axial Capacity, P_1/P_{1v}			Axial Capacity, P_1/P_{1u}		
$1/2t_f$	0.78	0.51	0.17	0.78	0.53	0.20
t_f	1.00	0.68	0.32	1.00	0.74	0.36
$2t_f$	1.23	0.85	0.39	1.21	0.94	0.46
$1/2t_w$	0.34	0.00	0.00*	0.43	0.00	0.00*
t_w	1.00	0.68	0.32	1.00	0.74	0.36
$2t_w$	1.59	1.30	0.97	1.17	1.08	0.91

W30x124						
Lateral Load (kN)	4.45	44.5	90.0	4.45	44.5	90.0
Plate Thickness	Axial Capacity, P_1/P_{1v}			Axial Capacity, P_1/P_{1u}		
$1/2t_f$	0.80	0.64	0.48	0.88	0.78	0.63
t_f	1.00	0.86	0.67	1.00	0.93	0.81
$2t_f$	1.29	1.12	0.91	1.27	1.22	1.12
$1/2t_w$	0.62	0.45	0.26	0.93	0.73	0.44
t_w	1.00	0.86	0.67	1.00	0.93	0.81
$2t_w$	1.58	1.44	1.27	1.16	1.13	1.06

*No intersection of strength and stability curves.

4.2.6 Limitations of Analytical Model

The analytical model is limited due to the assumed displaced shapes as well as the altered geometry of the damaged segment. Since all the damage is assumed to be concentrated in the flange in this model, this does not account for buckling in the web. Plots of the strength curves also assume the lateral displacements are uncoupled to enable the approximation of an axial capacity. The lack of ability to plot a meaningful strength curve based on the rotation also severely limits the usefulness of the analytical model. Despite these limitations, qualitative value can be extracted from the parametric study to guide further investigation.

4.2.7 Influential Parameters

Based on the results of the analytical study, the amount of damage that occurs within the cross-section due to local buckling has a significant impact on the residual axial capacity. While the length over which the local buckling occurs is of interest conceptually, the length itself does not appear to have a significant effect on the axial resistance of the member. Both the web and the flange thickness which are related to the plate slenderness ratios can potentially play a major role in estimating the residual capacity of members under this combined loading scheme. Therefore,

further consideration of the effect of plate slenderness parameters as well as quantifying the effect local buckling has on interrupting the load path will be explored in the finite element studies discussed next.

4.3 FINITE ELEMENT MODELING

To investigate the collapse behavior of steel columns and the current AISC seismic design guidelines, a number of carefully selected wide flange column members are subjected to a combined axial and monotonic lateral loading protocol using finite element simulations. Members were chosen from among those investigated during the cyclic study (Chapter 3) and are meant to represent sections that satisfy current AISC seismic requirements to various degrees.

4.3.1 Model Setup

Detailed finite element models of the cross-sections listed in Table 4-3 are created in the same manner described in Section 3.5. The same boundary conditions and reasoning used in Chapter 3 are used for this monotonic study. Due to changes in the slenderness parameters, an additional type of member to those discussed in Chapter 3 is identified (TYPE IV) as columns that satisfy the flange width-to-thickness ratio, but not the web width-to-thickness ratio for highly ductile members.

Table 4-3. Column data used for regression analysis and comparison with expected axial load

Section	$\frac{h}{t_w}$	$\frac{b}{t}$	$\frac{L}{r_y}$	$\frac{JS_x}{h_o}$	$\frac{\sqrt{JI_y}}{G}$	F_{ez}	CALR (FE)	Maximum Expected P/P_y (AISC Guidelines)
TYPE I								
W14x176	13.7	5.99	44.5	0.0067	0.0046	218.8	0.8	0.87
W14 - ½ web	27.4	5.99	42.2	0.0063	0.0059	215.9	0.8	0.88
W14 - 2 web	6.90	5.99	48.6	0.0103	0.0015	269.8	0.8	0.84
W14 - 2 flange	10.5	3.00	41.7	0.0341	0.0175	537.6	0.8	0.88
W27 - 2 web	19.7	7.16	64.7	0.0019	0.0032	139.3	0.5	0.74
W36x487	21.4	3.19	45.5	0.0039	0.0235	251.9	0.8	0.86
W36 - 2 web	10.7	3.19	52.1	0.0069	0.0340	25.56	0.7	0.82
W36 - ½ flange	23.1	6.38	53.8	0.0016	0.0086	33.06	0.6	0.81
W36 - 2 flange	17.8	1.60	40.5	0.0184	0.0873	781.6	0.8	0.89
W36 - 4 web	5.30	3.19	58.0	0.0284	0.0849	1456	0.7	0.78
TYPE II								
W27x146	39.4	7.16	56.3	0.0010	0.0022	133.8	0.6	0.76
W24 - 2 flange	36.2	3.76	54.8	0.0039	0.0049	175.2	0.6	0.89
W27 - 2 flange	36.2	3.59	50.0	0.0040	0.0078	199.0	0.7	0.82
W36 - ½ web	42.7	3.19	41.2	0.0036	0.0218	257.4	0.8	0.63
TYPE III								
W14 - ½ flange	15.3	12.0	49.6	0.0023	0.0730	153.4	0.7	NHD*
W24x117	39.2	7.53	61.2	0.0010	0.0014	114.1	0.5	NHD*
W24 - ½ web	78.5	7.53	55.2	0.0009	0.0012	118.5	0.5	NHD*
W24 - 2 web	19.6	7.53	71.0	0.0020	0.0021	122.9	0.4	NHD*
W24 - ½ flange	40.8	15.1	71.9	0.0005	0.0005	91.38	0.4	NHD*
W27 - ½ flange	41.1	14.4	65.6	0.0005	0.0008	107.9	0.5	NHD*
TYPE IV								
W27 - ½ web	78.9	7.16	50.4	0.0009	0.0009	139.9	0.6	NHD*
W36 - ¼ web	85.4	3.19	38.9	0.0037	0.0216	87.81	0.5	NHD*

*Not Highly Ductile (NHD) member based on current design guidelines

4.3.2 Loading Schemes

Two loading protocols are used to investigate the behavior of these members under a combined axial and monotonic lateral loading scheme. The first protocol involves applying a force-

controlled constant axial load ranging from $0.20P_y$ to $0.90P_y$ then applying a displacement-controlled lateral force up to 10% drift. This loading protocol, hereafter called load-then-drift (LTD) protocol, is similar to that used in the cyclic study and is used to determine a critical axial load ratio (CALR) as defined in Chapter 3.

The second protocol involves applying an initial force-controlled axial load ranging from 0Py to 0.75Py, then a displacement-controlled lateral force to drifts of 2%, 4%, and 6%, and is finished by a force-controlled axial load to failure at the final drift level. This protocol, termed drift-then-load (DTL), is employed to determine how the initial axial load affects the failure mode and enables the ability to predict the residual capacity based on the expected failure mode.

Twelve different sections are studied using the detailed finite element models. All twelve sections are studied under the DTL protocol while a subset consisting of four sections is studied under the LTD protocol. Only four sections were selected for the LTD protocol because each section is modified to include different flange and web thicknesses leading to a total of 20 members studied (4 altered thicknesses and the original geometry for each section selected).

4.4 RESULTS OF LOAD THEN DRIFT PROTOCOL

To address the important parameters used in the current seismic design guidelines as well as those seen in the cyclic loading analysis, four sections representing the various types shown in Figure 4-13 were selected and their web and flange thicknesses were varied to determine the influence of these parameters while other section properties remained constant.

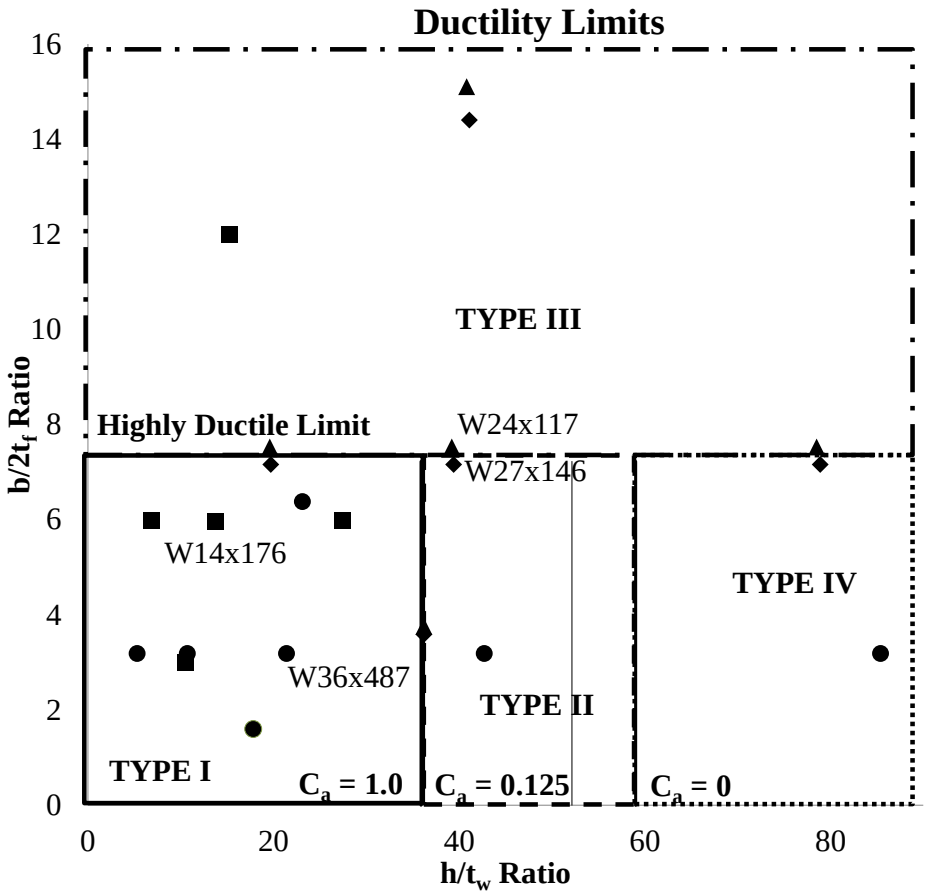

Figure 4-13. Selected columns' slenderness ratios with respect to seismic design guideline limits. Variations of the flange and web thickness of each section are represented by the shape of the original labeled section – W36x487 (circles), W14x176 (squares), W27x146 (diamonds), W24x117 (triangles).

4.4.1 Flange Width-to-Thickness Ratio

For all four sections studied, the best performing section was the member with a doubled flange thickness and the worst performing section was the member with a halved flange thickness. The CALR either remained the same as the original section or increased slightly when the flange thickness was doubled. The CALR decreased for all four sections when the flange thickness was halved supporting the idea that once a threshold *b/t* ratio is achieved, increasing it further has little effect on the axial load the section can carry up to 4% drift. This is consistent with the

findings in Chapter 3 that once the *b/t* limit is satisfied, this parameter does not significantly influence the prediction of the CALR.

4.4.2 Web Width-to-Thickness Ratio

For deeper sections, a decrease in the web thickness can lead to better behavior than the original section while an increase can lead to worse behavior. For the W24x117, W27x146, and W36x487, the halved web performed as well as the original section while the doubled web performed worse. The web thickness was quartered and quadrupled in the case of the W36x487 to test the limits of this trend. The quadrupled web section performed similarly to the doubled web, but the quartered web performed much worse than the original and halved webs.

This odd behavior can be explained by the fact that the unbraced length to radius of gyration increases when the web thickness increases despite keeping other parameters the same. From the previous work, there was a strong correlation between lower h/t_w and lower L/r_y values and high CALR. Therefore, when the web is halved, a lower CALR is expected since h/t_w is higher, but L/r_y is also being lowered at the same time which should result in a higher CALR. This would indicate that the L/r_y ratio plays a more significant role in predicting the CALR than the h/t_w ratio. This is seen in the deformed shapes of Figure 4-14 where local buckling controls for the thinner web thickness while lateral-torsional behavior dominates the thicker web sections. The fact that the quartered web does not perform according to this trend indicates there is a limit on how high the h/t_w ratio can be before the decrease in L/r_y does not compensate for the thinner web. This is consistent with the trend seen in the cyclic data where sections exceeding a certain h/t_w were unable to reach 4% drift under the lowest axial load considered.

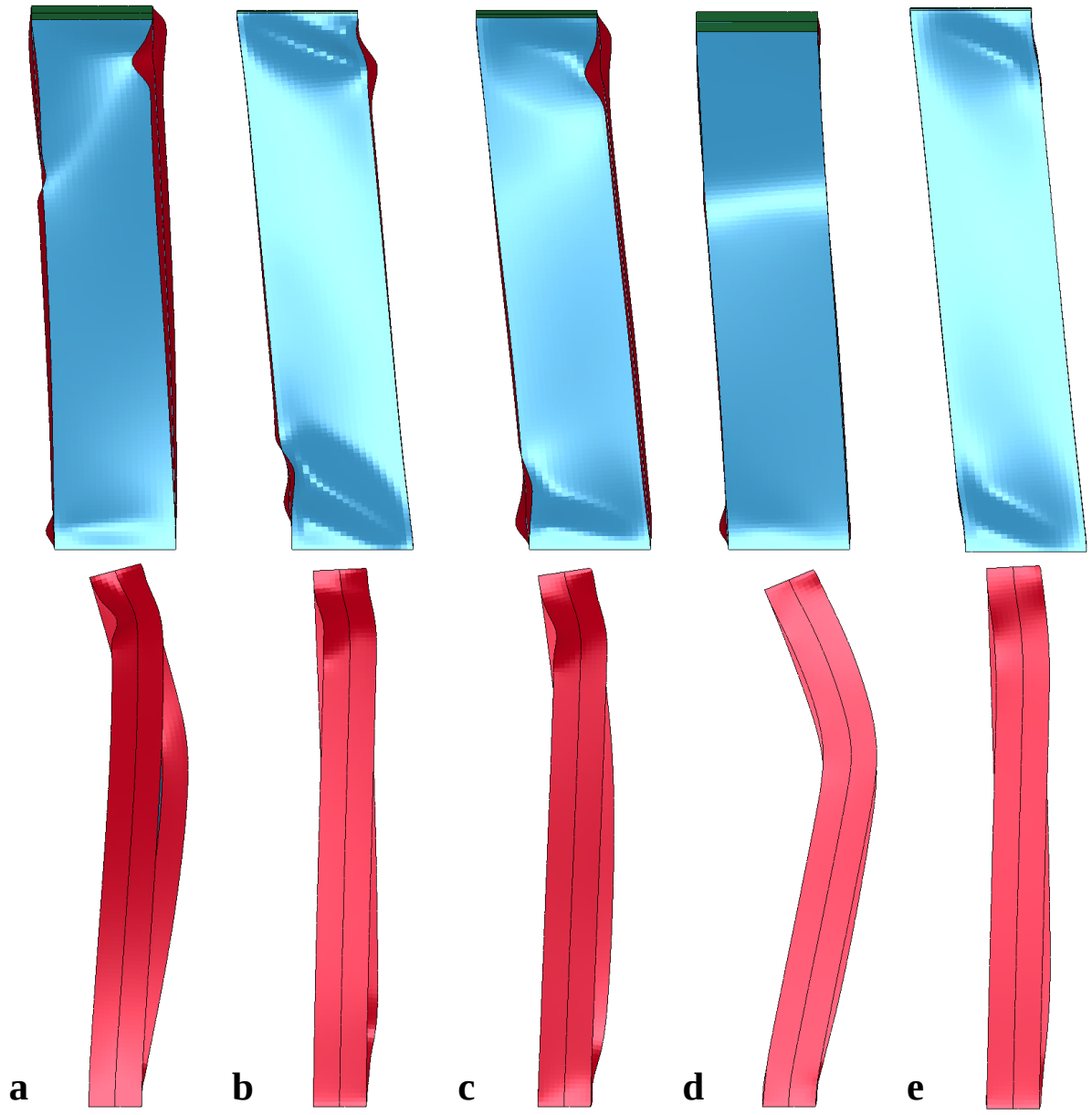

Figure 4-14. Failure modes for a W36x487 with a a) halved flange, b) halved web, c) original properties, d) doubled web, and e) doubled flange under $0.60P_y$

4.4.3 Regression Analysis

Using the CALR, P/P_y, for each section based on the axial load failure criterion, discussed in Chapter 3, a multivariable regression analysis is undertaken to determine which factors influence

the amount of load a column section is able to carry up to 4% lateral drift. The parameters included are the same as those used previously (Chapter 3).

To predict the response variable (RV), the general linear model used is:

$$RV = b_1 + b_2\, log(X_1) + b_3\, log(X_2) + \ldots + b_n log(X_{n-1}) \quad \text{4-26}$$

Where b_i are regression coefficients and X_i are predictor variables. Using the predictor variables from the cyclic analysis in conjunction with the response variable, P/P_y, the regression model can be written as:

$$\frac{P}{P_y} = b_1 + b_2\, log\left(\frac{h}{t_w}\right) + b_3\, log\left(\frac{b}{t}\right) + b_4\, log\left(\frac{L}{r_y}\right) + b_5\, log\left(\frac{\sqrt{JI_y}}{G}\right) + b_6\, log\left(\frac{JS_x}{h_o}\right) + b_7 log(F_{ez}) \quad \text{4-27}$$

Using backward elimination (Chaterjee et al. 2000) with standard t-tests until all the parameters are statistically significant at the 5% level results in the web width-to-thickness ratio and ratio of the unbraced length to radius of gyration of the weak axis being the main parameters influencing the critical axial load. Equation 4-27 is reduced to the proposed regression model:

$$\frac{P}{P_y} = 3.1939 - 0.0889\, log\left(\frac{h}{t_w}\right) - 0.5743\, log\left(\frac{L}{r_y}\right) \quad \text{4-28}$$

The coefficient of multiple determination for the linear regression of the critical axial load ratio on the web width-to-thickness ratio and the unbraced length to radius of gyration ratio is estimated to be 0.82, which means that these two geometric parameters jointly explain 82% of the variation in the critical axial load ratio. The magnitudes of the standardized regression coefficients both exceed one indicating that each parameter has a strong relationship with the CALR. The magnitude of the standardized coefficient associated with the unbraced length over

radius of gyration is much larger than that associated with the web width-to-thickness ratio indicating the former parameter has more influence in predicting the CALR. This corresponds to the behavior seen in the deeper sections where larger h/t_w ratios and smaller L/r_y ratios out performed those with smaller h/t_w and larger L/r_y ratios. Changes in L/r_y were less significant in the W14x176 than the deeper sections when the web and flange thickness were changed. This explains why the variations on that section did not follow the same web trend, but followed the flange trend for the CALR.

While the *b/t* ratio showed some influence on the CALR in section 4.4.1, this parameter does not contribute to the proposed regression model. As mentioned previously, the CALR is reduced every time the *b/t* ratio is halved, but tends to remain the same or increase slightly when the *b/t* ratio is doubled for the members studied. This implies that once a minimum threshold *b/t* ratio is reached, increasing that ratio does not improve the capacity of the member under this loading protocol. Therefore, the *b/t* ratio does not significantly improve the ability to predict the CALR and does not appear as a statistically significant parameter in the regression model used to estimate the CALR.

4.5 RESULTS OF DRIFT THEN LOAD PROTOCOL

Twelve sections as listed in Table 4-4 are investigated under initial axial loads ranging from $0P_y$ to $0.75P_y$ and loaded until failure after being laterally displaced to 2%, 4%, or 6% drift. Being able to predict the failure mode and capacity of the section given the initial axial load and column slenderness parameters will lead to a better understanding of these sections under a combined axial and lateral loading scheme and ultimately improved design guidelines. Various types of failure modes as labeled in Table 4-4 were exhibited by the range of sections. A "Global" failure mode indicates that the member did not experience significant local buckling

and failed in a global lateral torsional or flexural buckling mode. A failure mode leading with "Local" indicates that significant local buckling near the column ends was observed prior to failure. While "Local – Global (L – G)" columns ultimately failed in a global lateral torsional or flexural buckling mode, those just labeled "Local" experienced a localized failure near the column top while the rest of the member essentially remained elastic. Members labeled "Local-Transition (L – T)" also experienced significant local buckling and appeared to begin failing in a "Local" mode, but then experienced significant twisting as shown in Figure 4-15 (b). The post-failure shapes are shown in Figure 4-14 for the different "Local" failure modes where the column is shown both at failure and a few time steps following failure.

Table 4-4. Sections investigated using DTL scheme.

2% Lateral Drift										
Initial Load			$0P_y$		$0.25P_y$		$0.50P_y$		$0.75P_y$	
Section	L/r_y	P_n**/P_y (%)	P/P_y (%)	Failure Mode	P/P_y (%)	Failure Mode	P/P_y (%)	Failure Mode	P/P_y (%)	Failure Mode
W24x104	61.9	0.83	0.78	Global	0.70	Global	0.53	Global	-*	
W24x117	61.2	0.85	0.80	Global	0.77	Global	0.59	Global	-*	
W24x131	60.6	0.88	0.82	Global	0.77	Global	0.62	Global	-*	
W27x146	56.3	0.85	0.85	Global	0.82	L - G	0.72	L - G	-*	
W27x178	55.4	0.90	0.90	Global	0.85	Global	0.78	L - G	-*	
W27x194	54.	0.90	0.90	Global	0.86	Global	0.79	Global	-*	
W30x191	52.0	0.88	0.89	Global	0.86	Global	0.76	Global	-*	
W30x211	51.6	0.91	0.91	Global	0.88	Global	0.80	Global	0.79	L - G
W30x326	50.0	0.91	0.95	Global	0.91	Global	0.83	Local	0.80	Global
W36x247	48.1	0.87	0.90	Global	0.86	Global	0.75	Global	-*	
W36x282	47.4	0.90	0.90	Global	0.90	Global	0.79	Global	0.77	L - G
W36x487	45.5	0.93	0.98	Global	0.96	Global	0.89	Global	0.87	Global

4% Lateral Drift										
Initial Load			$0P_y$		$0.25P_y$		$0.50P_y$		$0.75P_y$	
Section	L/r_y	P_n**/P_y (%)	P/P_y (%)	Failure Mode	P/P_y (%)	Failure Mode	P/P_y (%)	Failure Mode	P/P_y (%)	Failure Mode
W24x104	61.9	0.83	0.75	Global	0.67	Global	0.53	L - G	-*	
W24x117	61.2	0.85	0.79	Global	0.74	Global	0.59	L - G	-*	
W24x131	60.6	0.88	0.82	Global	0.74	Global	0.62	Global	-*	
W27x146	56.3	0.85	0.84	Global	0.75	Local	0.72	L - G	-*	
W27x178	55.4	0.90	0.88	Global	0.81	L - G	0.78	L - G	-*	
W27x194	54.	0.90	0.88	Global	0.81	Global	0.79	L - G	-*	
W30x191	52.0	0.88	0.88	Global	0.80	L - T	0.76	L - T	-*	
W30x211	51.6	0.91	0.90	Global	0.82	L - T	0.80	L - T	-*	
W30x326	50.0	0.91	0.94	Global	0.86	Global	0.83	Global	-*	
W36x247	48.1	0.87	0.90	Global	0.77	Local	0.75	Local	-*	
W36x282	47.4	0.90	0.90	Global	0.82	Local	0.79	Local	-*	
W36x487	45.5	0.93	0.97	Global	0.93	Global	0.89	Global	0.76	Global

6% Lateral Drift										
Initial Load			$0P_y$		$0.25P_y$		$0.50P_y$		$0.75P_y$	
Section	L/r_y	P_n**/P_y (%)	P/P_y (%)	Failure Mode	P/P_y (%)	Failure Mode	P/P_y (%)	Failure Mode	P/P_y (%)	Failure Mode
W24x104	61.9	0.83	0.74	Global	0.64	L - G	-*		-*	
W24x117	61.2	0.85	0.79	Global	0.74	L - G	-*		-*	
W24x131	60.6	0.88	0.82	L - T	0.72	Global	0.53	Global	-*	
W27x146	56.3	0.85	0.73	Global	0.72	L - T	0.68	L - T	-*	
W27x178	55.4	0.90	0.86	Global	0.74	L - T	0.72	L - T	-*	
W27x194	54.	0.90	0.86	Global	0.78	L - G	0.74	L - T	-*	
W30x191	52.0	0.88	0.86	Global	0.74	L - T	0.70	L - T	-*	
W30x211	51.6	0.91	0.87	Global	0.75	L - T	0.74	L - T	-*	
W30x326	50.0	0.91	0.92	Global	0.80	Global	0.76	L - G	-*	
W36x247	48.1	0.87	0.86	Global	0.71	Local	0.70	Local	-*	
W36x282	47.4	0.90	0.89	Global	0.76	Local	0.72	Local	-*	
W36x487	45.5	0.93	0.97	Global	0.92	Global	0.82	L - G	-*	

*A dash indicates the member was unable to maintain the initial axial load up to the lateral drift specified.

** Nominal capacity calculated using K_y =0.7 and AISC (2010) Chapter E

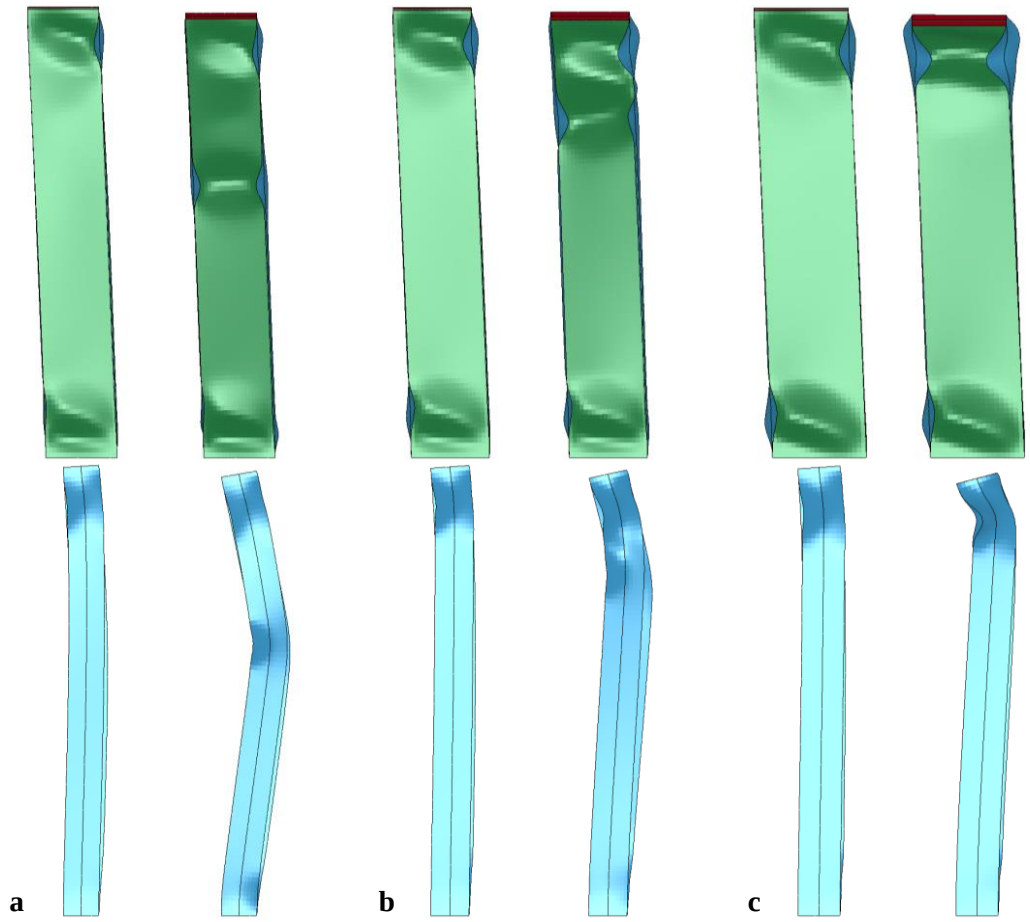

Figure 4-15. Deformed shape at failure and shortly after failure under initial load $0.50P_y$ for a) W27x194 (Local - Global), b) W30x191 (Local - Transition), and c) W36x282 (Local)

4.5.1 Initial Axial Load

As shown in 4-16, increasing the initial axial load leads to a decrease in the final axial load capacity of the section with respect to all the slenderness ratios at a drift of 4%. Similar behavior is exhibited at different lateral drift ratios and will be discussed further in the following section. The majority of the sections did not experience significant local buckling under an initial load of $0P_y$ as shown by the dominant "Global" failure mode in Table 4-4. When the axial capacity is increased from $0P_y$ to $0.25P_y$, the sections that continued to experience global failure only saw a decrease in final axial capacity of 5-8% except for the three W24 sections which saw a decrease

in axial capacity of 10% compared to their final axial capacity at $0P_y$. The sections that experienced significant local buckling at the column ends saw a decrease in final axial capacity ranging from 9-15% with the failure mode "Local" being on the high end and "Local – Global" being on the low end with "Local – Transition" in between. When the initial axial load was increased to $0.50P_y$, once again the sections that experienced "Local" failure modes had the largest decreases in axial capacity whereas the sections that experienced a "Global" failure mode had the smallest decreases excluding the three W24 sections. The W24 sections saw significant decreases in axial capacity due to the large L/r_y values leading to global lateral-torsional buckling prior to significant local buckling.

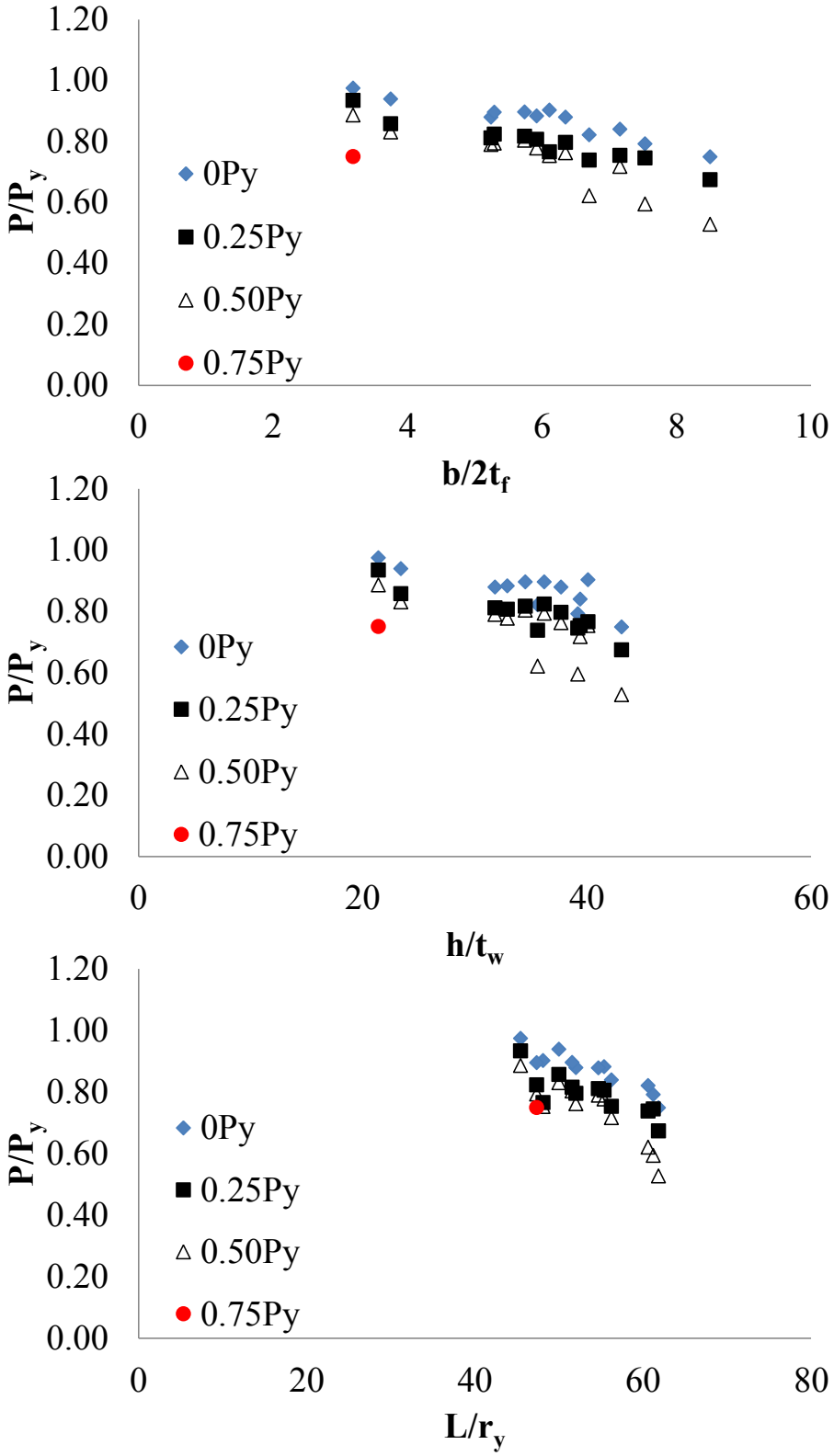

Figure 4-16. Relationship between axial capacity at 4% drift with respect to slenderness ratios for different initial axial loads

4.5.2 Lateral Drift

Drift levels of 2%, 4% and 6% were investigated under the various axial load ratios. As was expected, sections experienced more extensive local buckling and instances of local failure at higher lateral drift ratios as shown in Table 4-5. From this table it can also be noted that as significant local buckling increases due to an increase in lateral drift, the failure mode shifts from "Global" to "Local – Global" to "Local – Transition" and finally to "Local" if the local buckling becomes significant enough. In addition to increased local buckling, increasing the lateral displacement also lowers the final axial resistance of the member as shown in 4-17 and Table 4-6. Slender sections performed the worst with the two lighter W24 sections unable to reach 6% drift under $0.50P_y$ and the heaviest W24 section only achieving a final axial capacity of $0.53P_y$. After these members, the least compact sections of the W27, W30, and W36 sections investigated performed the worst. When subjected to 6% lateral drift with an initial axial load of $0.50P_y$, the final axial capacities of each of these sections were 20% below their flexural compressive strengths calculated using AISC Chapter E (2010) with $K_y=0.7$ as shown in Table 4-4. While increasing the lateral drift ratio increases local buckling and shifts the failure mode, the reduction in axial capacity is relatively minor. This implies that columns are still able to carry significant axial load in the face of local buckling and drift.

Table 4-5. Failure modes for different levels of lateral displacement under an initial axial load of $0.25P_y$

Section	Lateral Displacement		
	2%	4%	6%
W24x104	Global	Global	Local - Global
W24x117	Global	Global	Local - Global
W24x131	Global	Global	Global
W27x146	Local - Global	Local - Transition	Local - Transition
W27x178	Global	Local - Global	Local - Transition
W27x194	Global	Global	Local - Global
W30x191	Global	Local - Transition	Local
W30x211	Global	Local - Transition	Local - Transition
W30x326	Global	Global	Global
W36x247	Global	Local	Local
W36x282	Global	Local	Local
W36x487	Global	Global	Global

Table 4-6. Final axial load for different levels of initial axial load at each drift level.

Section	Initial Axial Load											
	$0P_y$			$0.25P_y$			$0.50P_y$			$0.75P_y$		
Drift Level (%)	2	4	6	2	4	6	2	4	6	2	4	6
W24x104	0.78	0.75	0.74	0.70	0.67	0.64	0.63	0.53	-	-	-	-
W24x117	0.80	0.79	0.79	0.77	0.74	0.74	0.69	0.59	-	-	-	-
W24x131	0.82	0.82	0.82	0.77	0.74	0.72	0.74	0.62	0.53	-	-	-
W27x146	0.85	0.84	0.73	0.82	0.75	0.72	0.80	0.72	0.68	-	-	-
W27x178	0.90	0.88	0.86	0.85	0.81	0.74	0.78	0.78	0.72	-	-	-
W27x194	0.90	0.88	0.86	0.86	0.81	0.78	0.81	0.79	0.74	-	-	-
W30x191	0.89	0.88	0.86	0.86	0.80	0.74	0.84	0.76	0.70	-	-	-
W30x211	0.91	0.90	0.87	0.88	0.82	0.75	0.84	0.80	0.74	0.79	-	-
W30x326	0.95	0.94	0.92	0.91	0.86	0.80	0.89	0.83	0.76	0.80	-	-
W36x247	0.90	0.90	0.86	0.86	0.77	0.71	0.82	0.75	0.70	-	-	-
W36x282	0.90	0.90	0.89	0.90	0.82	0.76	0.87	0.79	0.72	0.77	-	-
W36x487	0.98	0.97	0.97	0.96	0.93	0.92	0.94	0.89	0.82	0.87	0.76	-

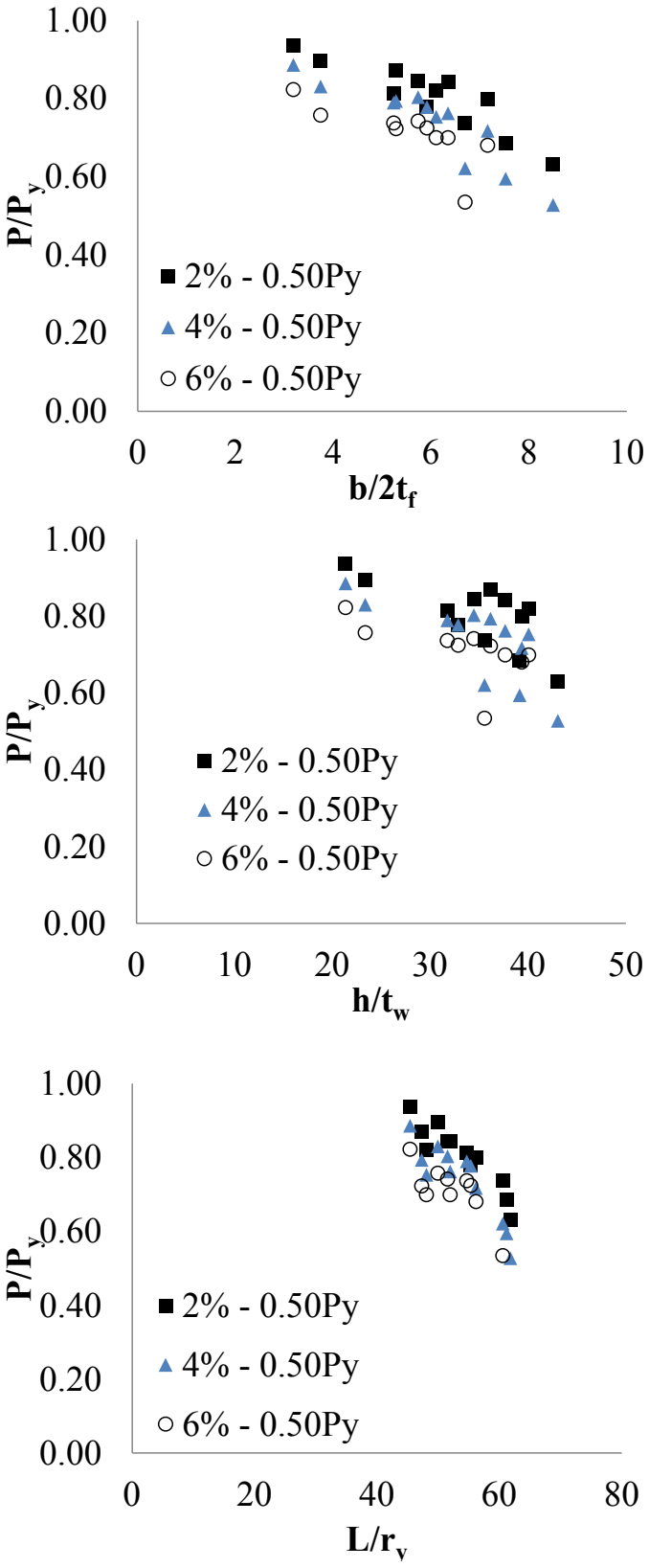

Figure 4-17. Relationship between axial capacity at each drift level with respect to slenderness ratios for an initial axial load of 0.50P_y.

4.5.3 Interruption in Load Path

Based on behavior presented in Figure 4-15, it is clear that significant local buckling is occurring under this loading scheme. However, as seen in Figures 4-16 and 4-174-17, this local buckling does not correspond to as severe of a drop in axial capacity as expected based on the analytical model.

In Chapter 2, it was shown that any interruption of the load path could significantly reduce the axial resistance of a steel column. However, this was with complete removal of elements in the flange and was extrapolated to assume that local buckling presented a similar load path interruption. That is to say, it was assumed that local buckling of the flange and web rendered the elements completely unable to transfer the load as is commonly assumed in cold formed steel sections with the effective width method (Ziemian 2010). It is clear from this study that this assumption is inaccurate for hot rolled sections. Despite large amounts of local buckling, the sections are still able to maintain a significant portion of the squash load. Even if the elements are still able to maintain load, it would be expected that their resistance would drop in proportion to the angle, θ, they maintain with the original geometry as shown in Figure 4-18. A similar angle can be calculated for the web buckle.

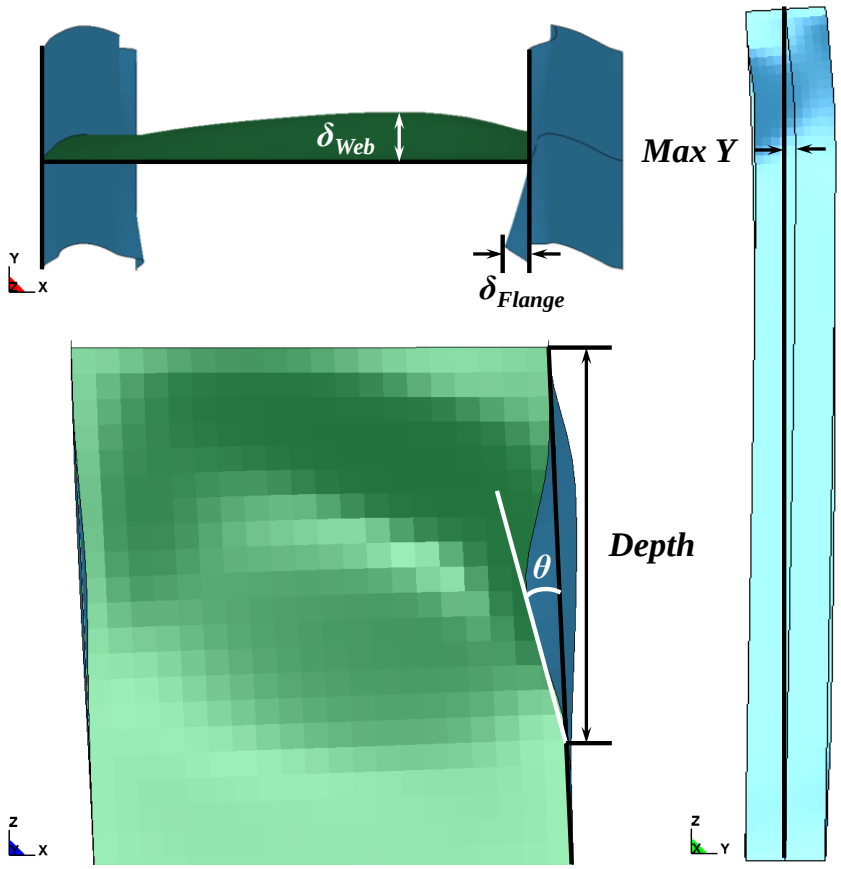

Figure 4-18. Local buckling seen in W36x282 at 4% drift at point of failure

With this in mind, several parameters outlined in Table 4-7 were recorded in an attempt to quantify the local and global behavior seen under this combined loading scheme based on geometric properties. The largest out of plane displacement of the web (δ_{Web}) and flange (δ_{Flange}) are recorded to determine the angle, θ, and quantify the amount of local buckling. The largest out of plane displacement of the web along the weak axis (*Max Y*) is also recorded to quantify the amount of twisting present at failure (θ). The depth over which the local buckling occurred was consistently within 5% of the depth, *d*, of the section. The amount of axial shortening also shows a clear trend of increasing as local buckling increases, which as stated previously increases as the lateral drift increases. These trends are evident in Figure 4-19. The implication of these trends is that local buckling is the reason axial shortening has occurred. Therefore if you control local

buckling through compactness criteria, axial shortening will not be an issue. This is consistent with the experimental findings of Uang et al. (2015) and their statement that "most of the column specimens showed significant shortening *after* severe local buckling or global buckling occurred."

Table 4-7. Parameters used to measure local and global behavior at 4% drift under $0.25P_y$

Section	*Depth/d* (%)	δ_{Web}/d (%)	δ_{Flange}/d (%)	*Shortening/L* (%)	*Max Y* (mm)	θ (rad)	P/P_y (%)
W24x104	-	-	-	0.89	89.9	0.30	0.67
W24x117	-	-	-	0.92	84.3	0.28	0.74
W24x131	-	-	-	0.83	91.4	0.30	0.74
W27x146	94.9	12.0	12.4	1.07	50.6	0.15	0.75
W27x178	101	9.02	7.81	0.92	61.9	0.18	0.81
W27x194	-	-	-	0.67	93.6	0.27	0.81
W30x191	91.3	5.90	10.6	0.98	43.0	0.11	0.80
W30x211	97.2	5.20	8.48	1.00	42.5	0.11	0.82
W30x326	-	-	-	0.85	63.4	0.15	0.86
W36x247	84.5	10.8	10.3	1.18	43.3	0.09	0.77
W36x282	88.8	10.0	6.63	0.96	48.5	0.10	0.82
W36x487	-	-	-	0.91	52.3	0.11	0.93

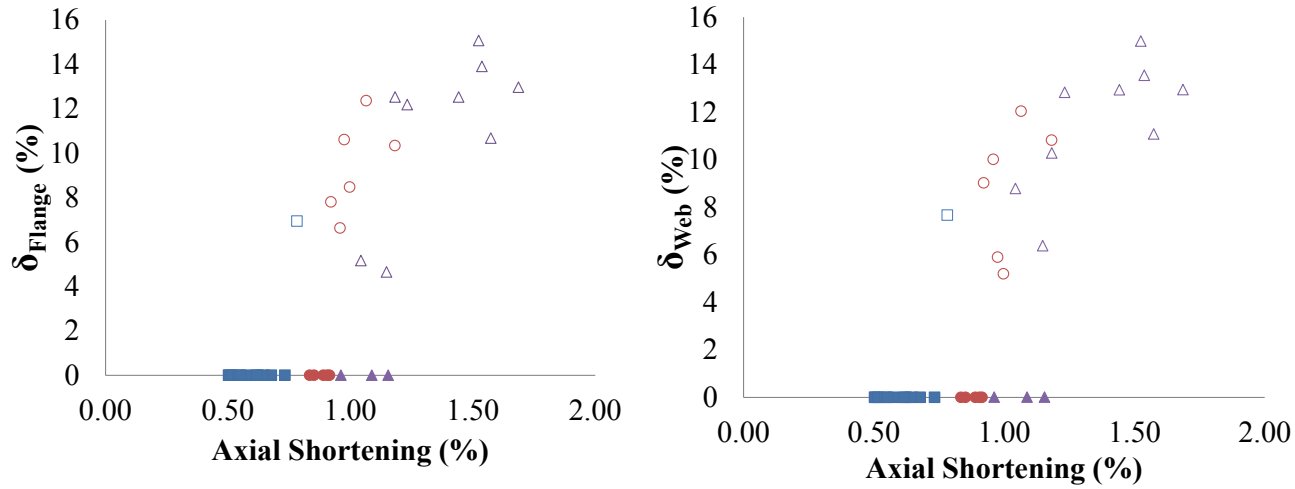

Figure 4-19. Relationship between axial shortening and amount of local buckling in flange and web under 0.25Py for 2% (square), 4% (circle), and 6% (triangle) lateral drifts for columns that experienced either a global failure mode (solid) or significant local buckling (unfilled) prior to global failure.

Based on the length, d, and the measured maximum displacement in the web and flange shown in Table 4-7, the angle, θ, ranges from 7 to 17 degrees for all the columns studied. Taking the cosine of these angles to determine the magnitude of the vertically transferred load through these buckled elements, the worst case scenario is a 5% reduction in load transfer. This severe angle is also only present at the extreme fiber of the flange and quickly returns to insignificant values closer to the intersection with the web. For the web, this severe angle is present over the majority of the depth indicating the web buckle is likely causing a more significant reduction in the capacity than the flange buckle. These observations are illustrated in Figure 4-20 by a cross-section in the locally buckled region for a W36x282 that has an initial axial load of 0.25Py and is laterally displaced to 4% drift. The solid elements are fully yielded and the unfilled elements have varying stress magnitudes less than the yield stress at the time of failure. The average stresses in each element over the course of the loading history are shown in the plots adjacent to the cross-section.

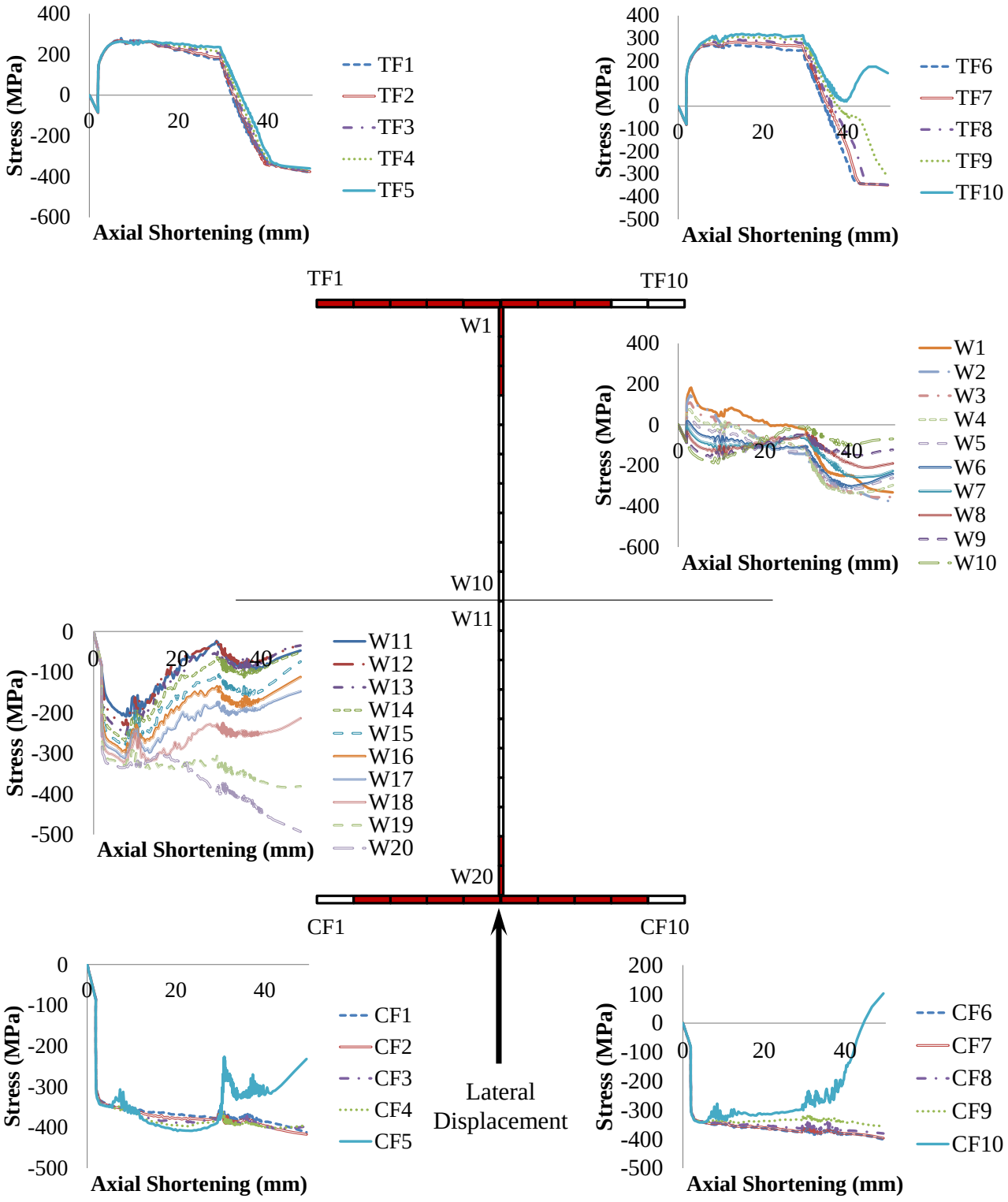

Figure 4-20. Stresses in cross-section over time with cross-section indicating elements that have yielded at failure (solid)

While the majority of the web elements are not yielding, they are still carrying stresses ranging from 39 to 240 MPa with elements closer to the intersection of the plate elements supporting more of the load as shown in the distribution of average stress over the cross-section for various points in the loading protocol as shown in Figure 4-21.

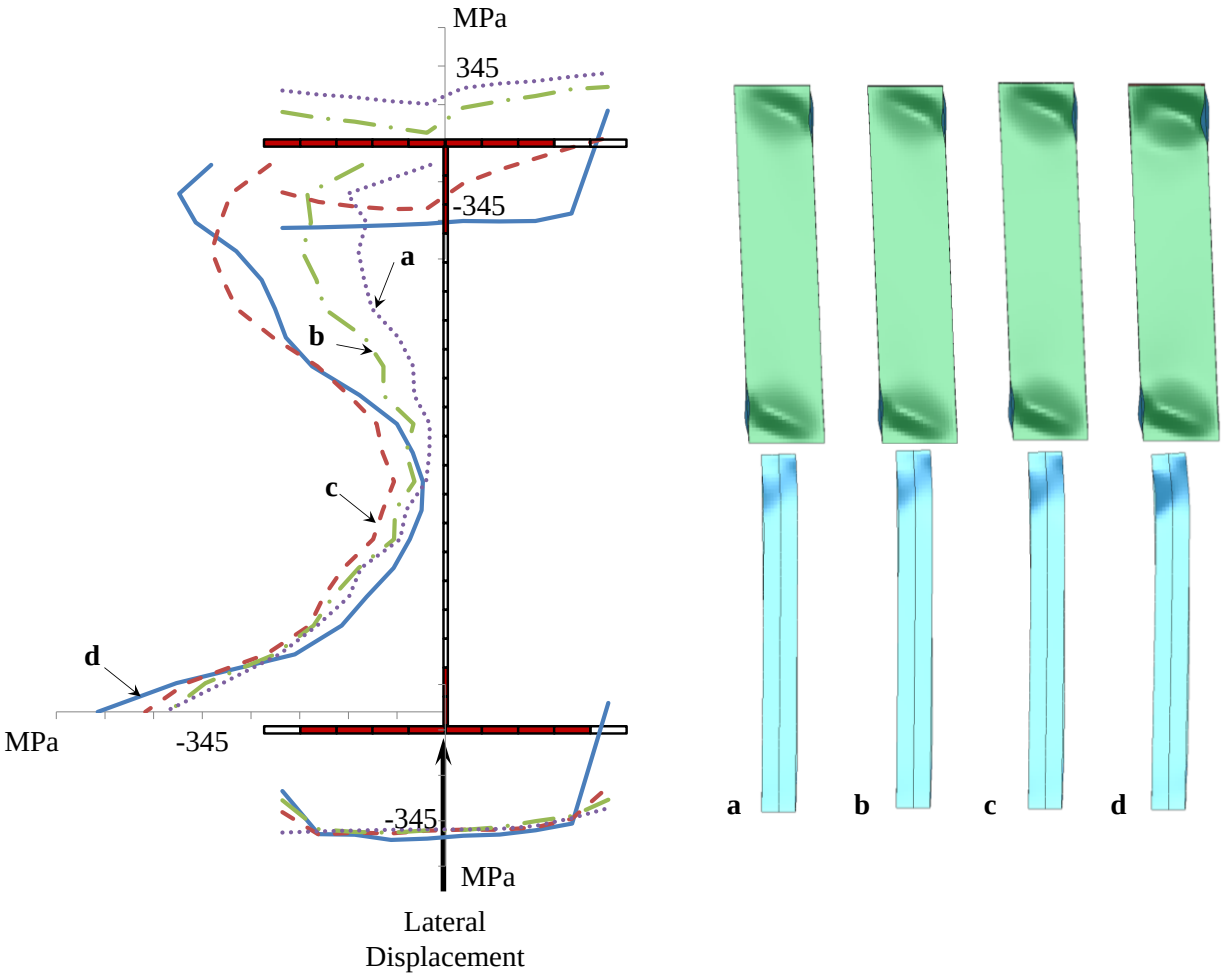

Figure 4-21. Stress distribution over cross section at a) end of drift – 4% drift, 0.25P_y (dotted line), b) 4% drift, 0.36P_y (dash-dotted line), c) 4% drift, 0.74P_y (dashed line), and d) failure – 4% drift, 0.82P_y (solid line)

As the axial load increases to the point of failure, the compression flange tips and the elements near the center of the web lose some of their ability to support the load. These regions are the locations of the most severe angle of flange and web buckling. The flange that initially began in

tension because of the drift protocol has picked up the load being shed by the severely buckled regions and essentially fully yields except for an exterior element that fluctuates into tension as the member buckles about the weak-axis. The reduction in the ability of the distorted elements to transfer the load does not entirely account for the reduced capacity in the member indicating that other behavior is influencing the capacity.

4.5.4 Effective Length Factor

Both the initial axial load and lateral drift trends indicate that increased local buckling leads to the potential for a "local" failure mode which corresponds to the most severe drop in axial resistance. However, interruption of the load path due to local buckling does not appear to sufficiently account for this drop in capacity.

The impact of local buckling near the column ends not only interrupts the load path, but also results in changing boundary conditions that affect the effective length of the column. The local buckling and associated yielding reduce the constraints at the column ends which increase the effective length factors, K_y and K_z. The effective length factor for weak-axis flexural buckling, K_y, is calculated since it is the predominant mode of global failure seen in the members. This value is determined by using the equations from AISC Chapter E (2010) assuming the nominal compressive strength, P_n, is the recorded axial capacity from the FE models. While significant twisting behavior is evident in the majority of the members, the effective length factor for torsional buckling, K_z, is closely related to and exhibits similar trends to those seen for K_y, but provides a more difficult physical meaning to grasp. As shown in Figure 4-22, as the initial axial load increases, the effective length factor increases in a nearly linear manner. This is consistent with an increase in local buckling seen in columns with higher initial axial loads and thus a

decrease in their axial capacity. The W24x131 section shown in Figure 4-23 is representative of how changing the lateral drift alters the effective length factor. Increasing the lateral drift increases the effective length, decreasing the axial capacity. This increase is exacerbated as the initial axial load level increases, which is consistent with more local buckling occurring under both higher drift levels and larger axial loads.

Figure 4-22. Relationship between initial axial load and the effective length factor for 4% lateral drift

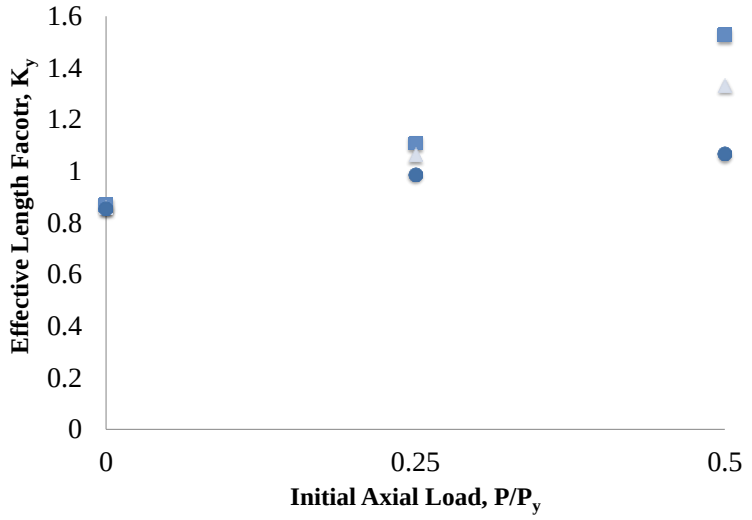

Figure 4-23. Relationship between 2% (circle), 4% (triangle), and 6% (square) drift levels and the effective length factor

Based on the trends seen for the various failure modes, conservative estimates of an effective length factor, K_y, for different axial load levels are shown in Table 4-8. This effective length factor can be used to estimate the capacity of the section, P/P_y, using the equations found in AISC Chapter E (2010) for flexural buckling and accounts for the various parameters studied herein. An effective length factor is not provided for cases that experienced the "Local" failure mode since K_y is associated with a global buckling mode. A method of predicting the capacity of members that experience "Local" failure will require further study as a clear trend is not apparent from the three members that exhibited this behavior.

Table 4-8. Predicted K_y value based on geometric properties.

Slenderness Parameters			Failure Mode	K_y
$0.25P_y$				
$L/r_y > 60$			Global or L-G	1.1
$60 > L/r_y > 50$			Global, L-T, L-G	1.1
$L/r_y < 50$	$h/t_w > 35$	$b/t > 5$	Local	NR*
	$h/t_w < 35$	$b/t < 5$	Global	1.0
$0.50P_y$				
$L/r_y > 60$			Global, L-G	1.4
$60 > L/r_y > 50$			Global, L-T, L-G	1.2
$L/r_y < 50$	$h/t_w > 35$	$b/t > 5$	Local	NR*
	$h/t_w < 35$	$b/t < 5$	Global	1.1
$0.75P_y$				
$L/r_y < 60$	$h/t_w > 35$	$b/t > 5$	L-G	1.2
	$h/t_w < 35$	$b/t < 5$	Global	1.1

*No recommendation (NR)

A comparison of the axial capacity predicted by using the modified effective length factors from Table 4-8 and the values obtained from the finite element models are shown in Table 4-9 for the case of 4% lateral drift. This modified factor provides a reasonably conservative estimate of the nominal capacity of the various sections. Absolute percent errors in capacity between the FE

model and the modified K_y calculation range from 1.5 to 7.7% with the modified K_y value being conservative for all sections except for the W24x104.

Table 4-9. Predicted axial capacities using proposed modified effective length factor for 4% lateral drift.

Section	P/P_y (%)						
		Initial Load $0.25P_y$			Initial Load $0.50P_y$		
	$K_y = 0.7$	FE	Modified K_y	% Error	FE	Modified K_y	% Error
W24x104	0.83	0.67	0.68	-1.49	0.53	0.56	-5.66
W24x117	0.85	0.74	0.70	5.41	0.59	0.57	3.39
W24x131	0.88	0.74	0.72	2.70	0.62	0.59	4.84
W27x146	0.85	0.75	0.73	2.67	0.72	0.69	4.17
W27x178	0.90	0.81	0.76	6.17	0.78	0.72	7.69
W27x194	0.90	0.81	0.77	4.94	0.79	0.73	7.59
W30x191	0.88	0.80	0.76	5.00	0.76	0.73	3.95
W30x211	0.91	0.82	0.79	3.66	0.80	0.76	5.00
W30x326	0.91	0.86	0.80	6.98	0.83	0.77	7.23
W36x247	0.87	0.77	*NR	-	0.75	*NR	-
W36x282	0.90	0.82	*NR	-	0.79	*NR	-
W36x487	0.93	0.93	0.86	7.53	0.89	0.83	6.74

4.6 CONCLUSIONS

The analytical model developed in this chapter indicates that the amount of damage within the cross-section has a much more significant impact on the axial capacity of the section than the amount of damage along the length. However, it was shown in the finite element models that local buckling in the flange and web is not equivalent to complete removal of the elements and that the elements in the buckled region can still support a significant amount of the load.

A statistical regression on models run in a similar fashion to the cyclic study performed in Chapter 3 indicates that while L/r_y and h/t_w are the most important parameters in predicting the

residual capacity, L/r_y has a more significant impact, especially for deeper sections. This is evident from the way the deeper members behave in comparison to the compact W14s when their web thickness is changed.

The final loading scheme illustrates the importance of the initial axial load prior to additional load being applied through the overturning moment. Both larger drifts and larger initial axial loads lead to significant local buckling. While axial shortening has been proposed as a concern, it is clear that shortening is the result of local buckling and can therefore be controlled by compactness limits that reduce local buckling issues. An increase in local buckling not only interrupts the load path, but also weakens and then alters the boundary conditions. While the interruption due to local buckling alone is insignificant, the additional alteration of the boundary conditions can lead to lower axial capacities than expected. Based on the sections studied, the expected failure mode and a modified effective length factor can be predicted based on geometric properties of the member. This contradicts the current practice of "conservatively" using K_y =1 as proposed in the commentary of the AISC Seismic Design Guidelines Chapter D (2010) based on the W14 study performed by Newell and Uang (2006). Using the CALR ratios from the cyclic studies in Chapter 3 yields higher K_y values, implying that this effective length factor will likely be increased under a cyclic loading scheme due an increased amount of local buckling near the column ends. This will need to be further studied under a comparable cyclic loading protocol to the DTL protocol.

CHAPTER 5

VISUALIZATION OF COMPLEX SPATIAL ARRANGEMENTS IN VIRTUAL REALITY

5.1 GENERAL

This chapter provides an introduction and the motivation behind the educational research objective. Current virtual reality (VR) technology is described and new virtual reality tools addressing structural engineering concepts are presented. The deployment of these models to the undergraduate steel design course is then discussed and situated in relevant educational studies, indicating where it can improve educators understanding of how students learn. Quantitative and qualitative evaluation of the impact of these models on improving student understanding of buckled shapes is also presented.

5.2 INTRODUCTION AND MOTIVATION

In the field of structural engineering, complex three-dimensional arrangements of structural elements are used to resist gravity, wind, earthquakes, and a multitude of other loading effects. Understanding how these arrangements deform and respond to loads is necessary for the successful design of structures (Wai et al. 2009). Traditionally, drawings and static pictures are used to convey the complexity of these spatial arrangements and their deformation modes. Depicting these three-dimensional objects in a two-dimensional manner requires students to build a mental picture of the structural member or assembly of several members with limited information and experience.

While visualizing complex spatial arrangements may be challenging for some people, the deformation or motion of these arrangements under various loading scenarios or other external stimuli only increases the difficulty of visual comprehension. Past research indicates that the general population has a wide range of spatial abilities and that these abilities are related to visualization comprehension (Velez et al. 2005). Due to this range of spatial ability, meaning a person's innate aptitude to visualize before any formal training has occurred (Sorby 1999), some students may struggle to understand three dimensional concepts represented in a traditional classroom setting. In attempts to clarify these complex arrangements, educators have resorted to physical models. While anecdotally more efficient in conveying the desired information than 2D projections, the types of phenomena capable of being explored with physical models are severely limited by cost and safety concerns, particularly at full-scale. Educators in the structural engineering field struggling with this problem have resorted to physical models. Figure 5-1a shows a steel sculpture promoted by the American Institute of Steel Construction and built on more than 100 colleges and universities across the United States (http://www.aisc.org/content.aspx?id=704). It is intended to show students how steel structural members intersect and are connected together using structural fasteners. Anecdotal evidence accumulated over many years suggests that students do gain good appreciation for the spatial nature of steel connections. They do so by walking around the sculpture, examining it and even touching its members. However, the sculpture is static and covers only a limited number of configurations. Such models can be replaced by simulation models as shown in Figure 5-1b allowing students to explore it on demand and with the instructor.

Figure 5-1. AISC Steel Sculpture as a a) physical model (www.aisc.org) and b) proposed virtual reality model.

The overarching goal of this mixed methods study is to evaluate the impact of newly developed virtual reality (VR) tools with respect to student learning through comparison with the standard lecture. Ideally, these VR models will provide an interactive, exciting way for students to improve their understanding of complex spatial arrangements and encourage them to pursue a career in civil engineering. An evaluation of these tools will provide an understanding of what is difficult for students to grasp about complex spatial arrangements and how the VR tools are addressing those difficulties. An understanding of student and faculty perception of the impact of these new VR methods for teaching concepts previously taught using traditional lecture methods will also be achieved. The research questions for this study include:

Q1: Do virtual reality models improve student understanding of complex spatial arrangements?

Q2: How do these models affect a student's ability to visualize or identify structural behavior and limit states?

Q3: How are these tools perceived by both the students and instructor in terms of their impact on student learning?

5.3 VIRTUAL REALITY MODELS

Virtual reality (VR) is a rich environment for comprehension and analysis of complex three-dimensional arrangements and is well-developed (Lee and El-Tawil 2008). It is an immersive environment, where users wearing the proper equipment can 'climb' up a model, 'squeeze' through an opening, or 'fly' up and around for an overview, thereby, experiencing the size and extent of important features in a natural and intelligible way (Figure 5-2). It is also an interactive environment, where a user can manipulate or manuever around the model being displayed.

Figure 5-2 shows a user in a CAVE-like environment that deploys VR (Cruz-Neira et al. 1992). The particular CAVE-like system used in this study consists of a 3 x 3 x 3 m room with life-size stereoscopic projections that fill the user's field of vision. A user wears a head mounted device to tell the system where s/he is looking and can use a variety of input devices or gestures to transmit commands as shown in Figure 5-3.

The idea behind this system is to achieve the illusion of complete immersion and interaction. For optimal portability, non-immersive VR that simply uses the screen of a desktop or laptop computer can be deployed as well (Figure 5-4). In this system, the user employs a head mounted device, such as the Oculus Rift (Luckey 2012), and hand system to provide the same type of input as in the CAVE-like system, but does not need to physically move around the environment. The portable device is more practical for most situations since the initial cost of the device is

several orders of magnitude lower than constructing the CAVE-like system. The CAVE-like systems that employ VR are also limited to one user at a time, so the use of portable devices is more practical for deploying this technology to a larger audience. Code was written to allow multiple users of the Oculus Rift to view the same model at one time. The primary user navigates the VR environment with a hand system while the additional users are carried along with the primary user's navigation. To avoid motion sickness of the non-primary users, each users' perspective is unique and is still controlled by motion tracking of their individual head set despite their global motion being controlled by the primary user.

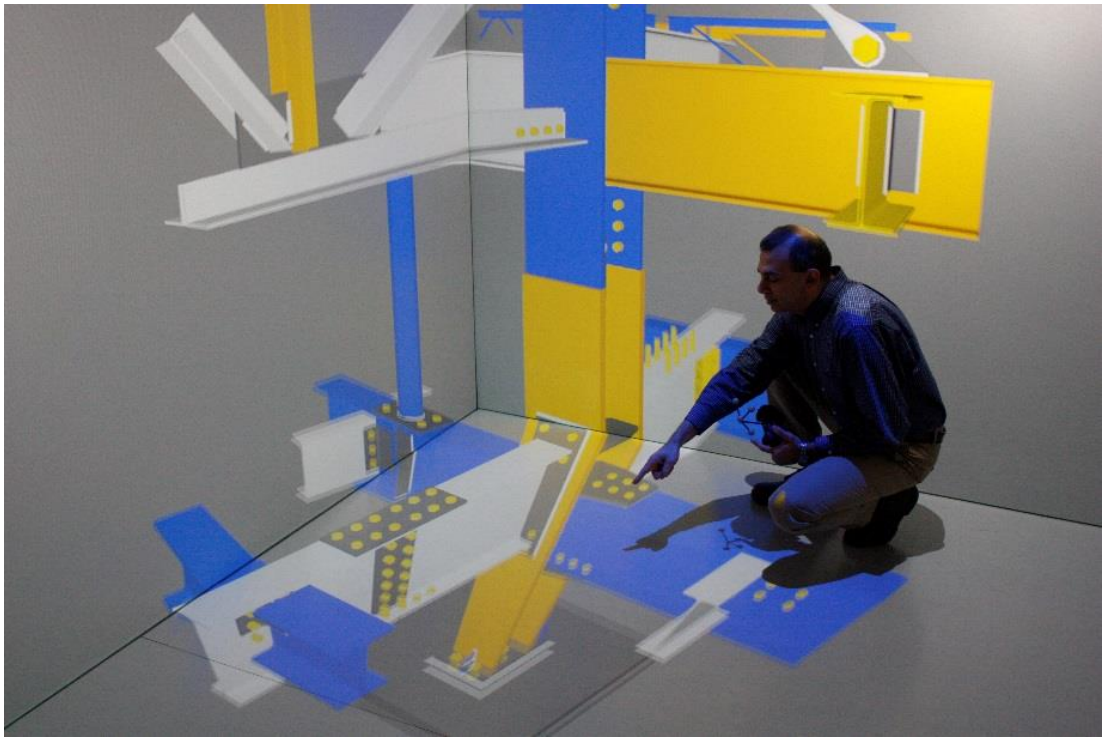

Figure 5-2. User in the CAVE-like environment used in this study.

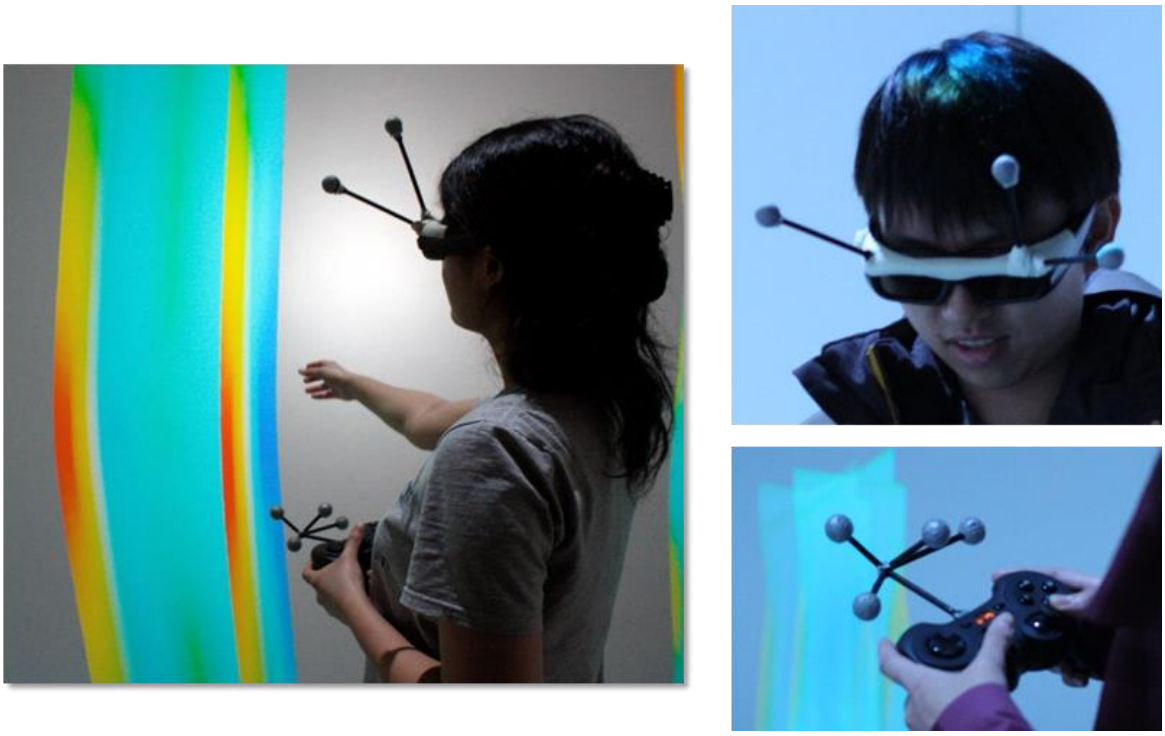

Figure 5-3. Users in the UM-MIDEN with the headset and hand tracking devices.

Figure 5-4. Several participants using a Portable VR System (Oculus Rift).

5.3.1 New Virtual Reality Tools

Several models have been created and displayed in the MIDEN for enhanced visualization. These models can be built on several platforms and converted to the virtual markup language (VRML) for viewing in a 3D manner.

5.3.1.1 Static Models

The AISC Steel Sculpture as shown in 5-5 is an example of a model that provides useful spatial information without any dynamic loading or animation. This model was created in AutoCAD, modified to include bolts and welds in AutoCAD Inventor, and directly exported to VRML using AutoCAD 3ds Max. Using the University of Michigan virtual reality software, Jugular 3.0, the VRML file of the static model can be directly loaded into the MIDEN for an immersive virtual reality experience. This capability allows for any full scale building created in AutoCAD to be quickly deployed for users to explore and investigate connection detailing and member spacing. Figures 5-5, 5-6, and 5-7 show various aspects of the model, clearly depicting the level of realism that can be achieved.

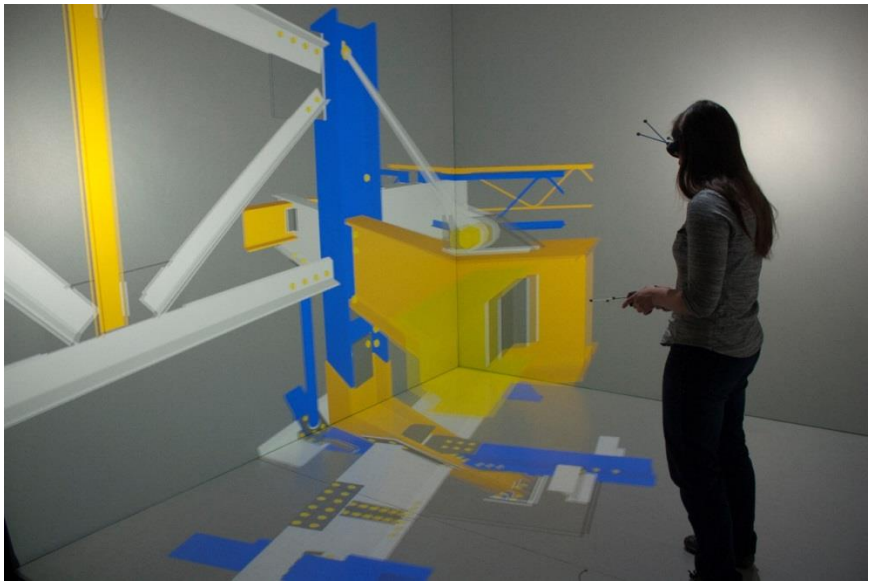

Figure 5-5. Static model of the AISC Steel Sculpture in the UM-MIDEN

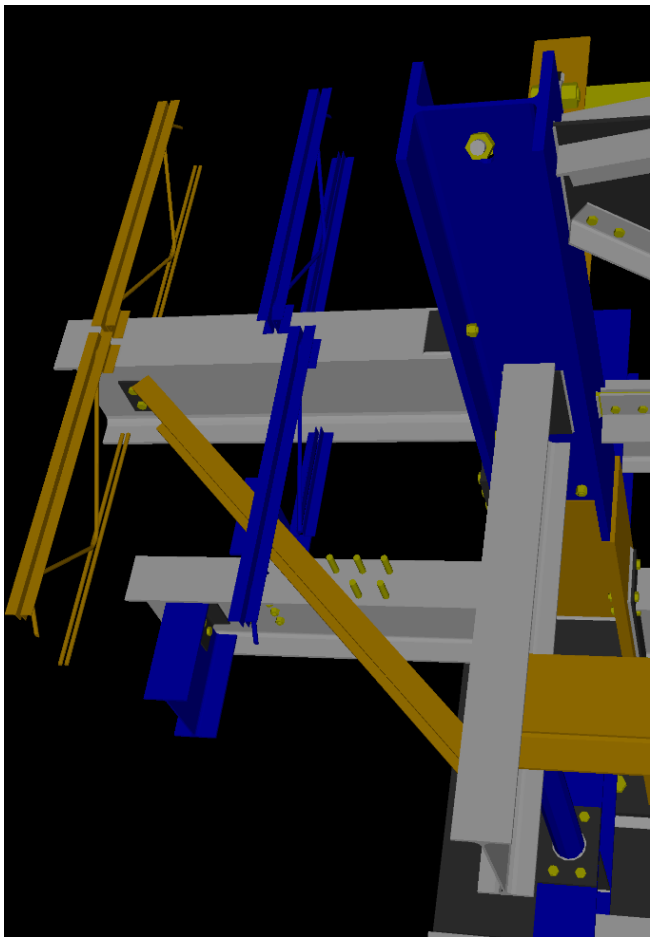

Figure 5-6. View 'floating' above the sculpture.

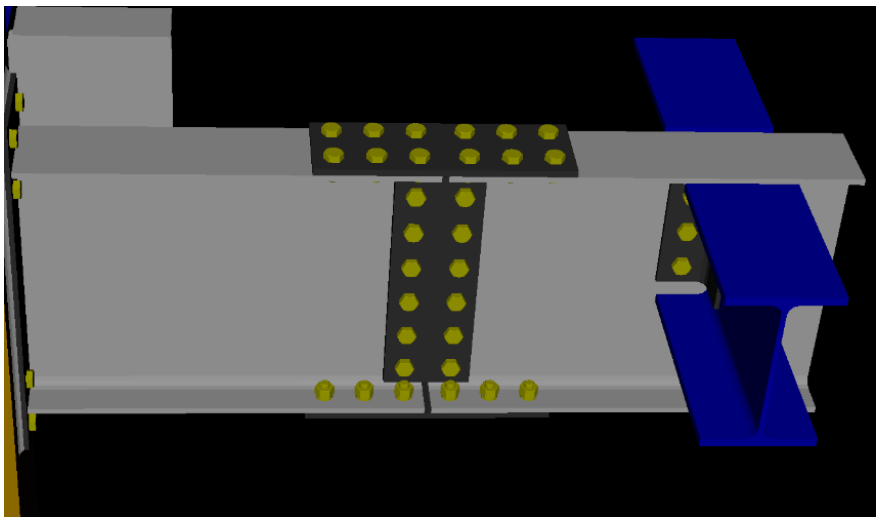

Figure 5-7. View 'peering' in on a connection.

In addition to the general user abilities, the code was modified to allow the user to remove parts for a clearer viewing experience. When a user points (using a laser-pointer-like model) at a particular member and presses a button, the member becomes translucent, in essence allowing the user to deconstruct the structure. The member remains translucent so that when a user wants to re-add the part back to the model, they merely need to point at it and press the same button. The code also allow for the user to press a different button to re-add all the parts at once if multiple members have been removed as shown in .

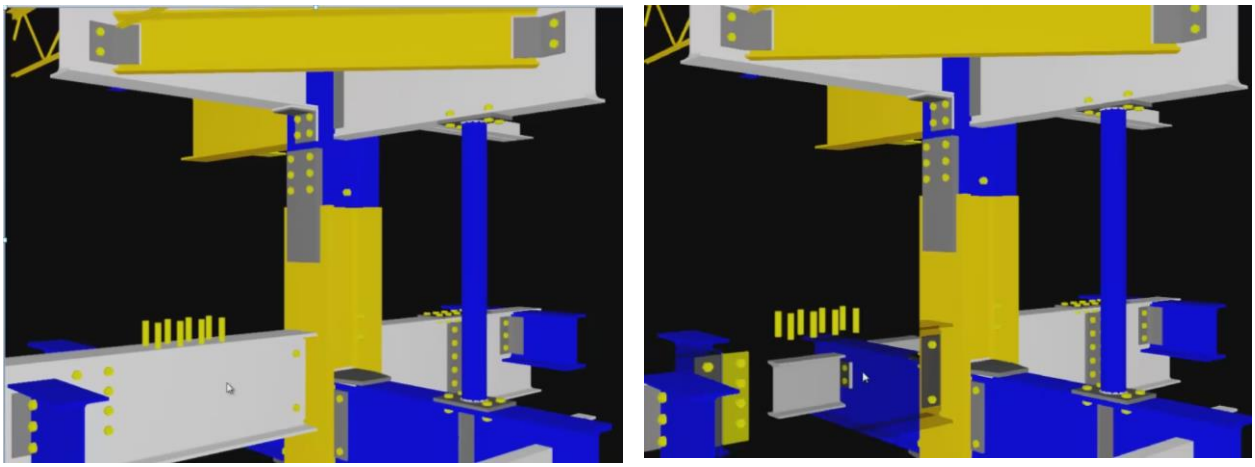

Figure 5-8. Translucence of the model is illustrated by the bottom left white beam

5.3.1.2 Dynamic Models

Another common complex spatial concept taught in undergraduate and graduate steel design courses is the buckling of beam and column members. Several models illustrating local and global buckling were created in the commerically available software, Hypermesh (2011) and analyzed using the LS-Dyna (2005) platform. Code was written to allow data obtained from the structural analysis software to be implemented in the MIDEN, so that users be immersed in a computer-generated environment to explore animations of local buckling, global buckling and the sequence of how one occurs and potentially leads to another.

Users have the same capabilites that were present in the static models, but can now also pause and control the speed of the animation. Currently, five column models have been developed to illustrate weak-axis flexural, strong-axis flexural, torsional, local flange, and local web buckling as shown in Figures 5-9 and 5-10.Users can also view an animation of the axial stress as it changes over time, superimposed on the main geometry of the column.

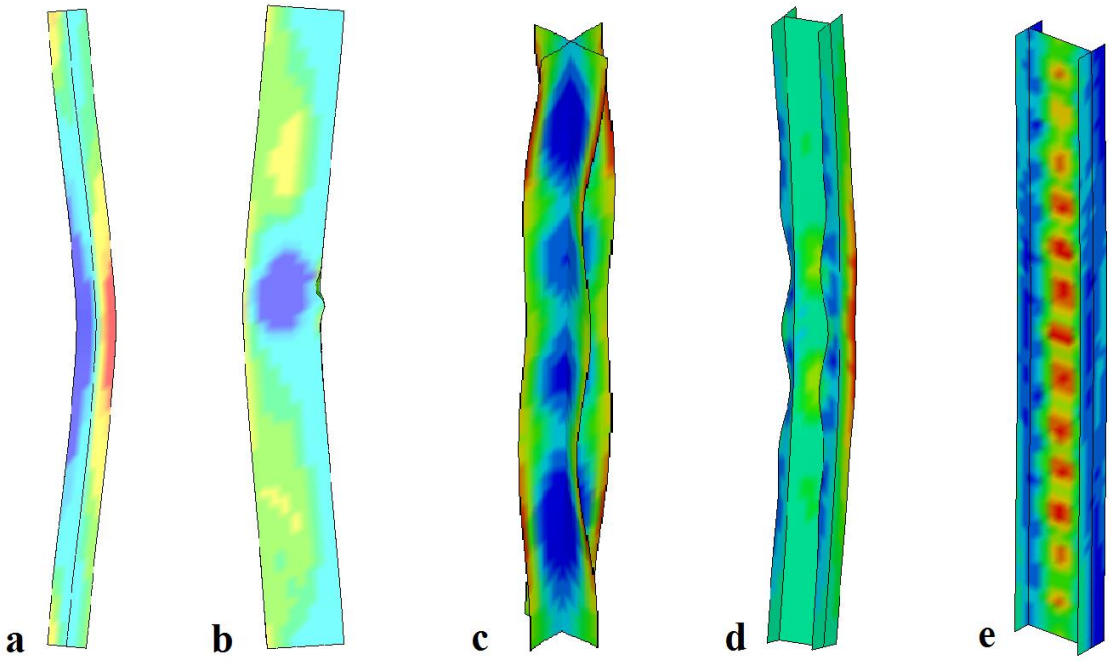

Figure 5-9. Five columns at various time steps illustrating a) weak-axis flexural, b) strong-axis flexural, c) torsional, d) local flange, and e) local web buckling.

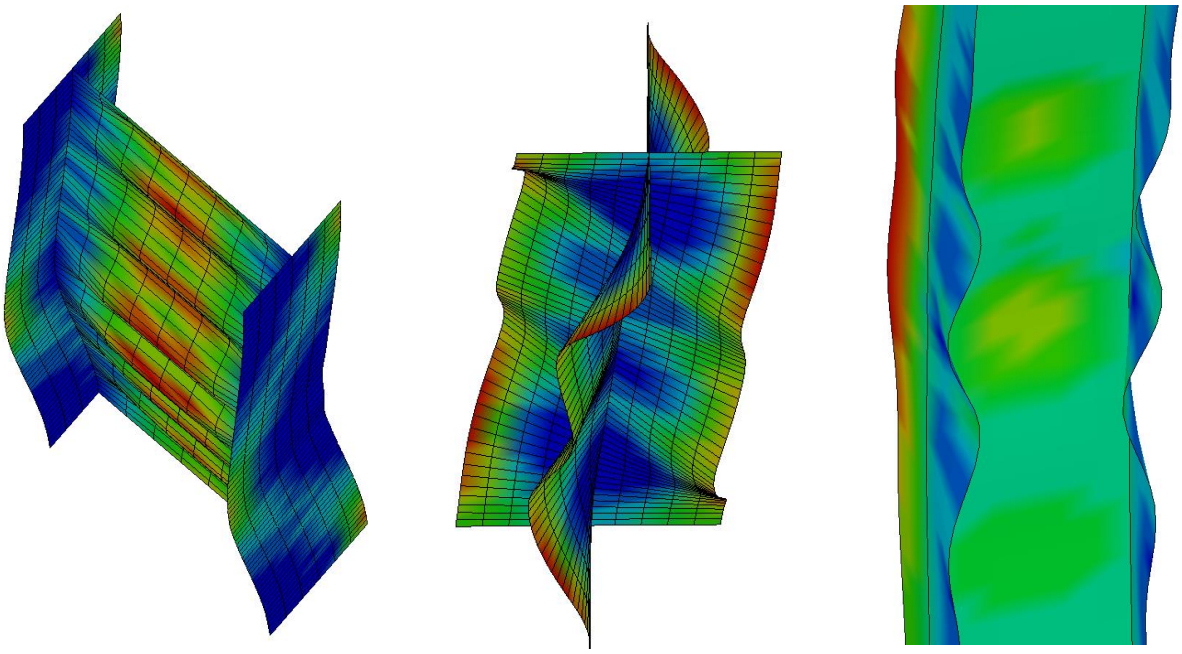

Figure 5-10. Additional views of global and local buckling behavior

5.4 EVALUATION OF VR MODELS

5.4.1 Theoretical Framework

This study is based on the theoretical framework for design research in education as defined by Cobb et al. (2003) and utilized by Koretsky et al. (2011). While the VR tools in this particular study are targeting a key concept in a specific field, the research questions are more concerned with understanding if and how these tools are helping students understand complex spatial arrangements. One goal of investigating these questions is to develop a design theory that "explains why designs work and suggests how they may be adapted to new circumstances," (Cobb et al. 2003, p. 9). As described by Cobb et al. (2003, p. 11), design experiments in the classroom have the "theoretical intent [to] identify and account for successive patterns in student thinking by relating these patterns to the means by which their development was supported and organized." To elicit these successive patterns, it is imperative to understand how students are thinking about the key concepts before, during and after their experience with the VR models.

As stated in the research questions, this thinking will be elicited by addressing student's perceptions about their learning and gaining an understanding of their epistemological beliefs meaning "the beliefs students hold to be true about the nature of knowledge and the nature of knowing," (Carberry et al. 2010, p. 1). Understanding how the identified patterns are developed and supported is necessary to provide a sense of the tool's affordances for helping students learn other content in the future. To prepare for this study and identify the appropriate methods to address the research questions, it is useful to understand how new technology has been used and evaluated in other educational situations.

Several studies have looked at the effects of using virtual laboratories in which students obtain data by interacting with computer simulations of laboratory or industrial process equipment. For example, Koretsky et al. (2011) investigated the effects of physical laboratories and a virtual laboratory on student knowledge and awareness of their own learning through the use of coded surveys. Their findings suggest that students had more knowledge of experimental design and made more references to critical thinking and higher order cognition with the use of the virtual laboratories as opposed to just being exposed to the physical laboratory. Chaturvedi and Akan (2011) also investigated the impact of virtual laboratories on student learning using statistical analysis on quiz results from control and experiment groups. This study showed learning gains for students who were exposed to the virtual laboratory using quantitative methods.

Schnabel and Kvan (2003) looked at spatial understanding by having participants reconstruct a three dimensional object after having studied the object in either a 2D or 3D environment. Students were interviewed after the task was completed and accuracy of the reconstructed object was compared across the two groups. The results of the study indicated that the immersive 3D

experience provided the user with a better understanding of complex volumes and their spatial arrangements.

Ragan et al. (2012) investigated the effect of navigational control on a user's ability to retain information learned in a virtual reality environment. Their virtual reality tool consisted of "fact cards" providing information about animals, and the results of their study did not support the hypothesis that interactive control affects learning positively for this simple environment. The study actually showed that allowing the user to have manual control in navigating the virtual environment resulted in a lesser ability to recall information. The authors attributed this unexpected finding to the fact that the task was time-pressured and having manual instead of automatic control detracted from the learning task.

In a study addressing the ability of animations to improve understanding, Tversky et al. (2002) indicated that despite enthusiasm for animation, it has not produced the anticipated benefits. This study acknowledges the fact that interactivity is a factor known to facilitate learning, but careful studies addressing interactivity in combination with animation in facilitating student learning have not been undertaken.

It is apparent there is minimal literature regarding use of tools similar to the VR models proposed in this study. Therefore, the study of these tools represents a unique opportunity to provide a design theory that will enable this new technology to be used in other applications. This present study will also investigate the idea of animation with interactivity (i.e. the ability for the user to zoom, view the animation from alternative perspectives, and stop/start or control the speed of animation) and thus address a gap in engineering education research.

5.4.2 Methods

A mixed methods approach as seen in previous design experiments such as Brown (1992) and Koretsky et al. (2011) is adopted for this work. To quantitatively evaluate the impact of the VR models on student understanding (Q1), students are presented with pre- and post-tests about local and global buckling in steel columns similar in nature to the way Chaturvedi and Akan (2011) used quizzes in their study. Since validated instruments such as concept inventories regarding steel design, particularly buckling of steel members, do not currently exist, pre- and post-tests developed from past exam problems are used to assess student understanding of the topic. Nine of the questions are multiple choice while the final question asks the student to draw a simple figure as shown in Figure 5-11. Guidelines for the format of multiple choice questions were followed to decrease threats to validity with respect to the measuring tool used in this study (Haladyna et al., 2002). Incorrect answers that are based on commonly held misconceptions as experienced by the two PIs, who have taught this course numerous times, serve as distractors in the multiple choice questions. Questions 1 and 2 address the student's ability to identify buckled shapes based on figures showing cross-section displacement at mid-span as well as isometric views of the displaced shape along the length. Question 3 addresses the student's ability to visualize the buckled shape by asking them to draw the displaced figure along the length.

Q1: Identify the mode of buckling by the configuration of section a-a pictured below:

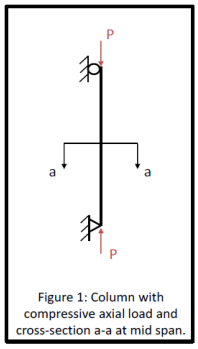

Figure 1: Column with compressive axial load and cross-section a-a at mid span.

A) Section a-a

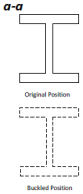

(A) Strong Axis Flexural Buckling
(B) Weak Axis Flexural Buckling
(C) Torsional Buckling
(D) Flexural-Torsional Buckling

B) Section a-a

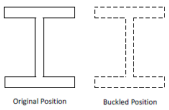

(A) Strong Axis Flexural Buckling
(B) Weak Axis Flexural Buckling
(C) Torsional Buckling
(D) Flexural-Torsional Buckling

C) Section a-a

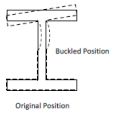

(A) Flange Local Buckling
(B) Web Local Buckling
(C) Torsional Buckling
(D) Flexural-Torsional Buckling

D) Section a-a

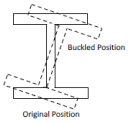

(A) Flange Local Buckling
(B) Web Local Buckling
(C) Torsional Buckling
(D) Flexural-Torsional Buckling

E) Section a-a

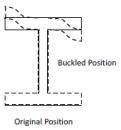

(A) Flange Local Buckling
(B) Web Local Buckling
(C) Torsional Buckling
(D) Flexural-Torsional Buckling

F) Section a-a

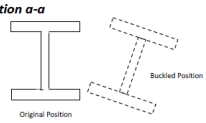

(A) Weak Axis Flexural Buckling
(B) Strong Axis Flexural Buckling
(C) Torsional Buckling
(D) Flexural-Torsional Buckling

Q2: Identify the mode of buckling by the configuration of the column pictured below.

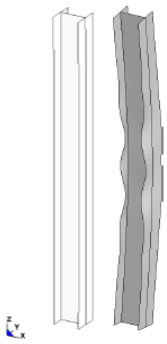

(A) Flange Local Buckling
(B) Flexural-Torsional Buckling
(C) Weak Axis Flexural Buckling
(D) Both A & C

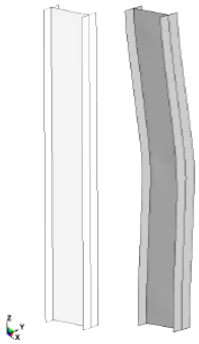

(A) Flange Local Buckling
(B) Web Local Buckling
(C) Weak Axis Flexural Buckling
(D) Flexural-Torsional Buckling

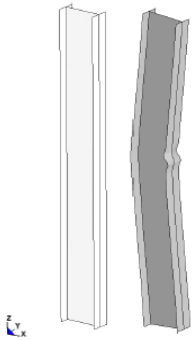

(A) Flange Local Buckling
(B) Strong Axis Flexural Buckling
(C) Weak Axis Flexural Buckling
(D) Flexural-Torsional Buckling

Q3: Given the following column and slenderness ratios:

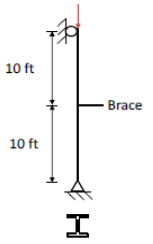

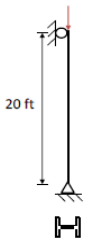

W12x65
Gr. 50 Steel
r_x=5.28 in
r_y=3.02 in
A=19.1 in^4

$$\frac{L}{r_x} = \frac{(20\,ft) * \left(12\frac{in}{ft}\right)}{5.28\,in} = 45.4$$

$$\frac{L}{r_y} = \frac{(10\,ft) * \left(12\frac{in}{ft}\right)}{3.02\,in} = 39.7$$

A) Draw the buckled shape for the axis that controls:

B) Draw the buckled shape for the axis that DOES NOT control:

Figure 5-11. Test questions used to assess student understanding of buckled shapes.

Surveys and interviews are used to assess student and instructor perception of the virtual reality tools (Q3). The survey consists of five questions meant to both elicit student perceptions of the models as well as offer feedback for improving and expanding the tools for other applications. The pre- and post-test data helped guide the selection of students to interview so that a range of student experiences are further explored. Specifically, three students whose test score improved, three students whose test score did not change, and three students whose test score decreased on the post-test were interviewed. Audio-recording devices are used during the semi-structured interviews and the conversation is transcribed with the exclusion of distractors and pauses as students contemplate or hesitate to answer. This denaturalized approach to transcription is employed in an effort to focus on the information context of the interview and accurately reflect the meanings and perceptions shared by the student (Oliver, et al., 2006). As discussed by Leydans et al. (2004), interviews are effective tools for obtaining the thoughts and perspectives of participants beyond the observations, such as the students' performance provided in the pre- and post-tests. Semi-structured interviews are used so that the same general ideas are discussed during each interview, but the interviewer has the opportunity to probe for additional information based on previous responses. Interviews were employed so students had the opportunity to not only identify what helped or hindered their understanding, but explain why different aspects of the virtual reality experience affected their ability to understand the concept in question. Only nine interviews were conducted due to the homogeneity of the group being studied and the fact that saturation appeared to occur, meaning additional information did not necessarily add anything to the theoretical narrative (Dey, 1999).

Field notes are used during observation of the students as they interact with the VR models and the instructor guiding them through the process. These observations address how the models are

affecting the students' ability to visualize or identify structural engineering concepts (Q2). Surveys and observation are performed for all the students who participate as the students only visit once and spend approximately 5-10 minutes using the VR tools. The duration and frequency of the visit is a product of the amount of class time that can be reasonably dedicated to this particular concept, but could vary depending on the content being conveyed by the VR tools.

5.4.2.1 Participants and Settings

The students involved are enrolled in a senior level undergraduate steel design course at a large Midwestern University. The first year that these models were deployed in this course, students could voluntarily choose to visit the CAVE-like environment during their regularly scheduled lab time. The generalizability of the impact on student learning that the proposed VR tools have is questionable due to the fact that the participants were not randomly chosen and already belong to a select and small pool of potential participants. In an attempt to address this lack of random sampling, the incentive for attending included having the higher of the pre- and post-test grades used to calculate their midterm grade. This incentive is given to encourage students who are struggling with the material to attend in addition to those who are naturally curious and want to learn more. As a result, students with a wide range of understanding chose to experience the VR models.

Of the 47 students enrolled in the steel design course during the fall of 2013, 24 students viewed the VR models as shown in 5-10. This group consists of 15 males and 9 females. Of the students who did not participate, 21 were male and 2 were female. The students who did not participate had an average score of 9.52 out of 10 on the pre-test and it is assumed that they did not participate due to satisfaction with their original exam grade, lack of interest in the VR tools, or misunderstanding in regards to the activity. Both groups of students received classroom

instruction regarding buckled shapes in a traditional manner (i.e. classroom lecture and 2D drawings) from the same instructor.

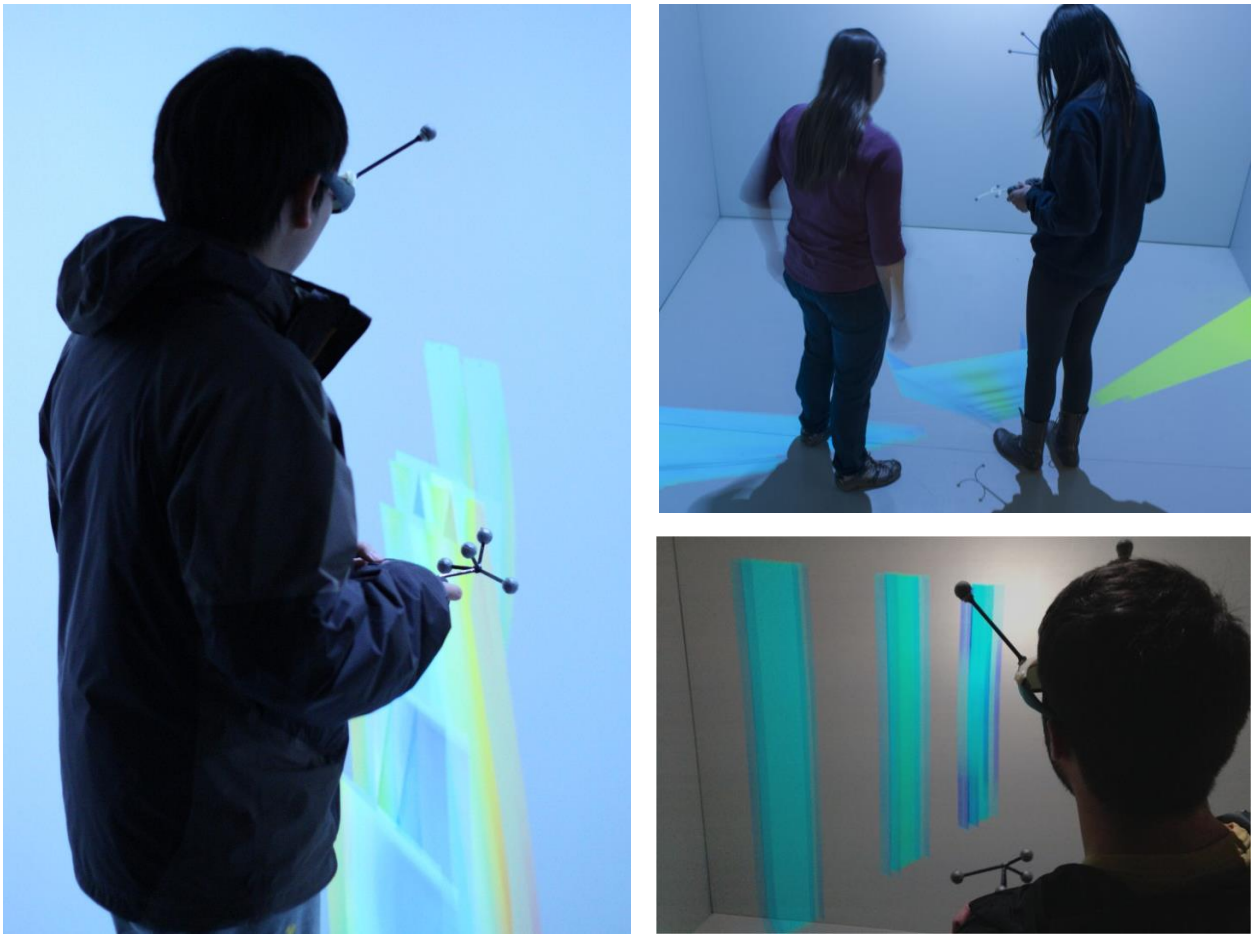

Figure 5-12. Students interacting with the buckling columns in the MIDEN.

Additional data was collected the following year in the same course. Due to the small size of the class, all 29 students participated in the virtual reality experience. While the measurement tools remained the same, both a CAVE-like environment as well as a portable head mounted device for a less immersive experience were employed as shown in Figure 5-13. The purpose of obtaining this additional data is to contribute to the validity of Q1 by increasing the sample size. This data also enables a comparison between using the CAVE-like environment and a Portable

VR Device to explore the effect of user navigation since students expressed concerns regarding the ease of using the controls in the previous year as described in the following section.

Figure 5-13. Students using the portable head mounted devices.

Concerns of validity include the fact that students who viewed the VR models received more instruction than those who did not participate, so their post-test score improvement may be a product of just more time spent discussing the subject matter as opposed to a reflection of the impact of the virtual reality tools. This reason was not substantiated when addressed in the interviews by students who felt they had an increased understanding of the concept. Triangulation (Patton 1999) in the form of multiple qualitative as well as quantitative methods of collecting data was used to produce a thorough understanding and address validity threats regarding all three research questions.

5.4.3 Results

After the interviews were transcribed and the data from the surveys were compiled, an iterative coding process was implemented. Following Miles et al. (2014), a set of first cycle codes were proposed and refined based on additional data. The *identify* and *visualize* codes are likely a product of the way students were asked questions on the survey as they were directly asked about their ability to identify and visualize buckled shapes. Open coding began with the survey data and additional codes were identified upon review of the transcribed interviews. All statements except for expressions emphasizing "how cool" the student found the experience were classified by a code developed in the first (survey) or second (interview) cycle of coding. These codes, or themes, were developed directly from the data based on patterns and repetitions and are summarized in Table 5-1. These themes were then used to provide a theoretical narrative for the learning process associated with the study as described subsequently (Auerbach and Silverstein, 2003).

Table 5-1. Codes applied to interviews and survey responses

Code	Description	Example
Identify	General expressions of recognizing buckled shapes	"The graphic models were very easily identifiable for the type of buckling that was occurring." "I wasn't sure how to first identify some, but the animations helped me compare the different types."
Visualize	General expressions of picturing buckled shapes	"I think it just gave me a better understanding of how they actually move instead of trying to envision in my head from the board or from something in the text book." "It helps a lot to visualize the buckling shapes."
Interaction	Expressions of being able to move around the model, view it from different angles, etc.	"I moved the column down more cause I was looking, almost as if I was like on a top floor of the building, and then once I lowered myself, I was sort of equal level, I saw it differently and that was helpful." "The maneuverability of the viewpoints was extremely helpful in making the buckling mode clear."
Colors	Expressions about the colors of the models	"I guess the colors helped me focus on a particular portion, so maybe if it was all the same color, you wouldn't know exactly where to look."
Project	Expressions of issues that student didn't have themselves, but felt other people might have	"I'm sure some people might have had a harder time." "I don't know if it was particularly, vastly beneficial for me, but I do know a lot of people who have a hard time visualizing things three dimensionally, and for that I can see this being, it's a very useful tool."
Guide	Expressions about the instructor interacting with the student during the experience	"…so he was kind of quizzing me, 'Well what form of buckling do you see on the end?' and I would tell him and he'd say 'Yeah, okay' and we'd go on."
Controls	Expressions about the device used to interact with the model	"It took a little to get accustomed to the controls." "I'm not used to playing with [video game controllers], so I was a little confused at first."
Difficulty	Expressions of confusion or lack of understanding of buckled shapes	"I think it's sort of hard to write on the board. Like, try to make students understand what it's supposed to look like in the field." "I know on some of them, I was a little bit confused about what they would actually look like or how they would behave. I think seeing them helped me."
Animation	Expressions about the movement of the models	"I liked how multiple types of buckling were shown and you can see which developed first." "Show stress concentration as they develop as well as the process in which different type of buckling occurs first." "…so then you can actually see what is moving."

5.4.3.1 Q1: Do virtual reality models improve student understanding of complex spatial arrangements?

Simple t-tests with respect to the difference between two means are employed to determine if the scores of participants significantly changed following the virtual reality experience. The scores are also compared between those who used the CAVE-like system and those who used the Portable VR system to determine if the ability to manually navigate through the VR environment significantly impacted their ability to identify and visualize the different deformed shapes. The simple t-tests assume that the data was obtained from an independent, random sample of students taking an undergraduate steel design course and that the distribution of pre- and post-test scores within each of the two compared groups is normal (Agresti and Finlay 2009).

A summary of the variables related to the various participants is found in Table 5-2. Results from the t-tests in Table 5-3 indicate that there was a statistically significant increase on average in the mean score of the post-test for students who experienced the fully immersive CAVE-like environment. The difference between the mean score for those who experienced the CAVE-like system and those who used the portable devices was not statistically significant at the 95% confidence level on both the pre and post-test.

Table 5-4 summarizes the differences in means between both the CAVE-like and portable device users compared to the students who did not have a VR experience. Students who participated in one of the VR experiences had on average, a statistically lower mean score on the pre-test than those who did not participate. Comparisons of the post-test results indicates that on average, the mean scores between VR users and Non-VR users were statistically insignificant at the 95% confidence level for Portable users. The significance for CAVE-like users lowered from 99.9% confidence to 95% confidence. This indicates that students who initially struggled with the

material closed the gap on the test scores with their peers who did not participate in the experience and previously had higher test scores on average.

Table 5-2. Descriptive statistics for variables related to test scores

Variable	Minimum	Maximum	Median	Mean	Standard Deviation
Pre-test Score (CAVE)	5.00	10.0	8.50	8.32	1.43
Post-test Score (CAVE)	7.00	10.0	9.00	8.94	0.919
Pre-test Score (Portable)	5.00	10.0	9.00	8.74	1.37
Post-test Score (Portable)	6.00	10.0	10.0	9.21	1.18
Non-VR Participant	8.00	10.0	10.0	9.52	0.593

Table 5-3. Comparison of means for participants with different VR techniques.

Variable	Difference in Mean Score (Post-Test – Pre-Test)	Degrees of Freedom	t-score
CAVE Test Score	0.620*	66	2.12
Portable Test Score	0.420	36	1.14
Variable	Difference in Mean Score (CAVE – Portable)	Degrees of Freedom	t-score
Pre-Test Score	0.41	51	1.04
Post-Test Score	0.27	51	0.86

*Note: *Significance, two tailed: p<0.05, **p<0.01, ***p<0.001*

Table 5-4. Comparison of means between VR users and non-users.

Variable	Difference in Mean Score (Non-VR User – VR User)	Degrees of Freedom	t-score
Pre-Test Score (CAVE)	1.40***	45	4.13
Post-Test Score (CAVE)	0.605*	45	2.67
Variable	Difference in Mean Score (Non-VR User – VR User)	Degrees of Freedom	t-score
Pre-Test Score (Portable)	0.763*	39	2.25
Post-Test Score (Portable)	0.289	39	0.97

*Note: *Significance, two tailed: p<0.05, **p<0.01, ***p<0.001*

5.4.3.2 Q2: How do these models affect a student's ability to visualize or identify structural engineering phenomena?

Based on observations of the students as they used the virtual reality tools, there appeared to be several different factors that influenced their ability to visualize and identify the structural engineering concepts. When asked to identify a shape by the instructor, many students hesitated, waited for the animation to complete more than one cycle, made the motion of the deforming column with their hand or described the motion they were seeing in a questioning tone, before providing a direct answer as to the type of buckling they were seeing. This behavior seemed to indicate that the animation and not just the final state of the column shape was pivotal in helping the student understand the buckling behavior.

Students also commented to the instructor about the colors drawing their eyes to behavior that helped them identify the type of buckling. For example, one student commented while pointing to two different columns in the VR space, "I can tell the difference between the column undergoing weak-axis buckling and the one undergoing web local buckling because of the stress concentrations on the web." These colors highlighted the differences in deformed shapes that were more nuanced and not discernable immediately or without rotating about the structural members.

Many students who hesitated to respond to the instructor's questions about identifying the buckling behavior would also navigate around the structural member before replying. After navigating around or being guided by the instructor to view a particular column from a certain vantage point, several utterances of "Oh" or "I see" were made by the students, followed by a correct declaration of the type of buckling behavior. The combination of being able to interact

with the models by viewing them from several angles appeared to elicit insight or sudden comprehension of the column behavior.

While looking at the deforming members, a few students expressed conflicting mental images with what they were seeing with comments like, "it's not what I imagined it looked like when it was described in class," or "I didn't think flange local buckling looked like that." Correcting misconceptions based on the way the concepts are described in class or displayed in a 2D format occurred based on observations of the students interacting with the VR tools.

5.4.3.3 Q3: How are these tools perceived by both the students and instructor in terms of their impact on student learning?

One student who was interviewed described the virtual reality experience as, "… a very useful tool. Not only because of the aide itself, but because it's so instantaneous, you can learn something right then. You can see it. It's not trying to imagine and confuse things and muddle them together." This idea, articulated in different ways, was echoed by several students – in essence, students felt that experiencing a spatial phenomenon in a spatial environment was useful in adding to their knowledge of the subject. Two of the students interviewed, who struggled on the pre-test, expressed *difficulty* extrapolating a 2D version of the phenomenon into 3D space, and stated that "seeing the whole entire member, rather than just the cross-section" helped them approach the post-test with more confidence and a better appreciation for buckled shapes. Some of the difficulties with these complex spatial arrangements were also expressed as projections onto other people, meaning the student did not feel they had an issue understanding the concept, but would *project* onto their cohort, perceived difficulties that they felt the VR models helped address as explained below.

5.4.4 Discussion

While many students made general statements about improvements or better understanding in their ability to *identify* or *visualize* buckled shapes, several of them associated these benefits with their ability to *interact* with the model (i.e. maneuver around it), the *colors* accentuating important features, and being able to communicate with the *guide* about concepts discussed in class while viewing the models.

Several students surveyed and those interviewed remarked on the advantage of being able to see this dynamic process actually occurring. While Tversky et al. (2002) commented that *animations* tend to not actually be useful when compared with a static version of the same phenomenon even if it is conveying a change over time as is the case with the topic studied here, students indicated that had the virtual reality model been paused at the point where buckling had occurred, it would not be as useful to them as seeing the process occurring. Tversky et al. (2002) mentions that interactivity, i.e. the ability to zoom in, change perspectives, and alter the speed of the animation, may overcome the difficulties of perception and comprehension that may arise from using animations versus static models. It appears the hypothesis of Tversky et al. (2002) is valid as students on average showed quantitative and expressed qualitative improvement in understanding the concept and attributed this improvement to their ability to interact with the animated process. Since this interactivity is an integral part of the VR models developed in this study, a careful comparison will be undertaken in future deployments so that students will be able to directly compare static versions of the models with animated ones and the usefulness of animations in teaching complex spatial arrangements can be explicitly addressed to determine if the interactivity or the animation is the key contributor to student learning.

While many commented on how useful the interaction and animation was for helping them visualize or identify buckled shapes, a few struggled to get a good command of the *controls* that allowed them to interact with the model. This is an issue that can be addressed by additional prep before entering the CAVE-like environment and future improvements in technology associated with VR environments. Use of the Portable VR devices also eliminates this issue as the instructor is guiding the students through the environment. One student described the experience as being "in a world that's controlled by the instructor where you actually get to see what's going on in his mind." This student also stated, "It was easier having [the instructor] guide because he could talk through the shapes at the same time as we were moving along and we were all on the same page." The quantitative results indicate that use of the manual control (CAVE) and automated control (Portable) did not result in a difference in the average post-test scores between the two groups as was found in Ragan et al. (2012). This is likely due to the fact that this was not a time sensitive exercise and the VR environment was used for conceptual understanding as opposed to memorization of facts.

Comparison of the fully immersive CAVE-like environment with the less immersive Portable device indicates that they are comparable in terms of improving student understanding. This is consistent with the results from Schnabel and Kvan (2003) indicating that studying a 3D concept in a 3D environment improves spatial understanding. This is also useful information in terms of implementing these tools for other concepts in classrooms of various sizes as the Portable devices are more cost and time efficient in conveying the desired information to an entire classroom.

The perceived relation among these recurring patterns is summarized in Figure 5-14 beginning with students expressing difficulties with the material and ending with an improved perception of

their spatial abilities related to the subject matter. This general theory of how the proposed intervention is supplementing the traditional method of teaching the material to help improve students ability to understand complex spatial arrangements is supported by the current data.

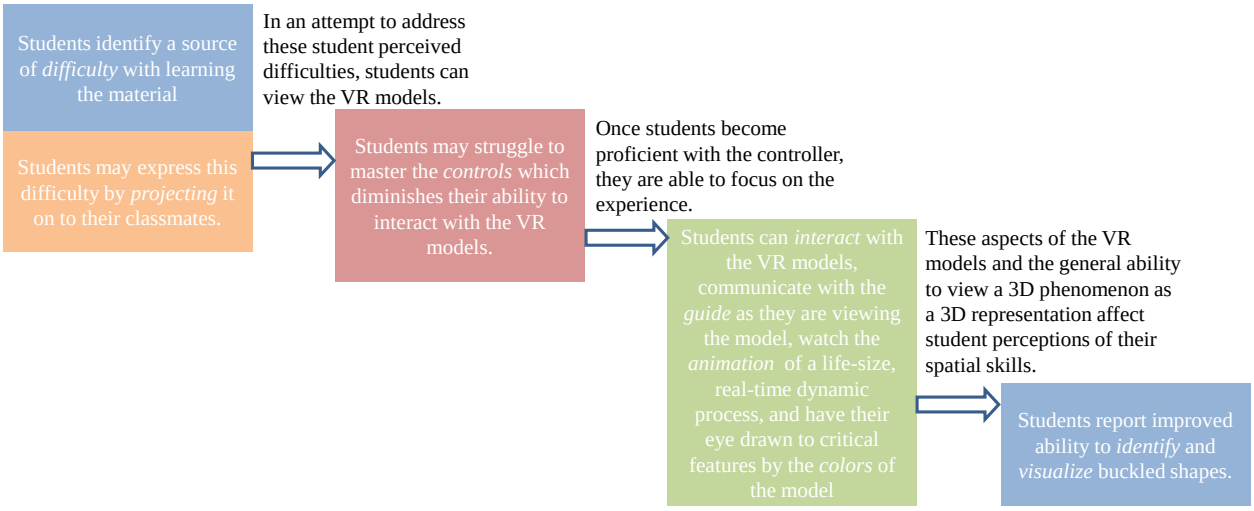

Figure 5-14. Relation among the patterns identified in the data.

5.5 CONCLUSIONS

The presented virtual reality models provide a unique learning tool to be used in the classroom when explaining complex spatial concepts. The versatility of these tools is evident by the ease with which the models can be modified and expanded to include the desired behavior or concept. These models also present an economical and time efficient method of conveying concepts to students at universities where lab space or physical structures are unavailable.

This mixed methods study addresses the use of virtual reality tools in the classroom and how they can aide in improving student understanding of multifaceted spatial arrangements. A simple multiple choice test to check for understanding of the concept was developed based on the knowledge of instructors with significant years of experience teaching the concepts. Simple tests of significance comparing pre and post-test mean scores of participants and non-participants

indicates that students on average improved their test score and thus their understanding of the concept. Instructors felt that their ability to communicate the material was improved with the virtual reality tools. Observations, surveys, and interviews all indicated that students believed they had a better grasp of the concept following the virtual reality experience. Future work includes improving the tools used to measure student understanding and further investigating the benefits of interaction versus animation. Deployment of different spatial concepts using the virtual reality tools should also be undertaken to further validate if the general theory on how student understanding is improving from this models is reasonable.

CHAPTER 6

SUMMARY AND CONCLUSIONS

6.1 SUMMARY

This dissertation explores the behavior of steel columns under various states of damage and extreme loading conditions. Computational and analytical techniques are used to quantify the axial resistance of steel columns that have undergone local flange damage as well as explore the behavior of steel columns under combined axial and lateral loading schemes. Virtual reality column buckling models are also created and their impact on student learning is evaluated using quantitative and qualitative methods. More details regarding these specific areas are summarized below.

6.1.1 Behavior of Locally Flange Damaged Steel Columns

The strength and stability of steel columns that have suffered localized damage is investigated through analytical and computational means. An analytical model based on the Rayleigh-Ritz technique is employed in conjunction with detailed finite element models that were validated using available experimental results. An equilibrium-based analytical model is also used to assess the performance of locally flange damaged steel columns. A parametric study is performed using the finite element models to assess the effect of location of damage, extent of damage, role of initial imperfection, as well as asymmetric damage on the stability of a steel column. Analytical and simulation results show that localized flange loss in a steel column could lead to a severe reduction in its axial resistance. Design guidelines utilizing commercial software typically found in a design office are presented to provide a practical technique for

approximating the results obtained using the analytical and computational models. An empirical model for quick use in the field is also proposed and validated with additional finite element models.

6.1.2 Behavior of Steel Columns Subjected to Combined Axial and Lateral Loading

Detailed finite element models validated with available experimental data are used to investigate the behavior of steel columns under a combined cyclic axial and lateral loading scheme. Local buckling and lateral torsional buckling appear to be reducing the column strength significantly at lateral drift levels lower than expected based on current AISC Seismic Design requirements, indicating that the current h/t_w and b/t limits are not sufficient for ensuring adequate ductility. Statistical regression analysis is performed to determine the critical parameters affecting the ability of the member to carry axial compressive loads up to 4% lateral drift so that more effective limits can be developed for highly ductile members. The results of this analysis indicate that L/r_y and h/t_w are the most critical parameters affecting the CALR. A design aide to supplement the current AISC guidelines is developed based on these parameters.

To further understand how these parameters are influencing the behavior and axial resistance of steel columns under a combined loading scheme, analytical and computational models are studied under combined monotonic axial and lateral loading schemes. A regression analysis using the monotonic loading protocol also indicates that L/r_y and h/t_w are the most critical parameters with L/r_y dominating the behavior of the member. While the analytical model shows steep reductions due to damage within the cross-section, it is seen in the finite element models that locally buckled regions are able to support a much higher axial load than anticipated and removal of these elements to mimic a load path interruption is not an appropriate assumption. While some reduction in capacity can be attributed to interruption of the load path in locally

buckled regions, these regions also contribute to weakening and altering the original boundary conditions, further reducing the axial capacity of the member. This understanding led to the proposal of a modified effective length factor for predicting the capacity of members that has experienced a global failure mode.

6.1.3 Visualization of Complex Spatial Arrangements using Virtual Reality

Models that are undergoing different modes of deformation and failure are deployed in a virtual reality setting. This allows students and educators to immerse themselves in a 3D environment and enables them to fully explore a structure from all facets to better understand structural behavior at both the member and system level. The virtual reality environment developed allows users to interact with a structure through a head mounted device and hand system that can be deployed on a virtual reality headset such as the Oculus Rift if a CAVE-like system for complete immersion is unavailable. This allows the virtual reality models to be directly accessible in the classroom. Pre- and post-tests covering the structural engineering topic as well as surveys and interviews of the students using the virtual reality tools were analyzed in this mixed methods study. Quantitative results indicate that students were able to identify and visualize the deformed structural shapes more accurately after the virtual reality experience. Qualitatively, students expressed an improved understanding, greater enthusiasm for the topic, and a desire for other topics to be presented using the proposed VR tools. Both instructors and students noted the advantages of using virtual reality to explain and understand the deformation of complex spatial arrangements. Students felt they had a stronger understanding of the concept after the experience and on average, showed a statistically significant increase on the post-test evaluating their understanding.

6.2 CONCLUSIONS

Major findings from this research are as follows.

6.2.1 Behavior of Locally Flange Damaged Steel Columns

- Analytical and computational techniques indicate that local flange damage can severely reduce the axial capacity of steel column members. As long as damage has occurred the reduced capacity is relatively insensitive to the amount of damage along the length of the column.
- The capacity of the damaged column relative to its original capacity is primarily a function of the ratio of the cross-sectional area in the damaged segment to the area of the undamaged cross-section. The trend correlating these two ratios was insensitive to the type of cross-section studied.
- The proposed simplified design model affords practicing engineers a method by which they can reasonably estimate the residual capacity of a locally damaged column.
- An empirical model is derived and enables a quick, but reliable assessment of the residual capacity of locally flange damaged steel columns in the field.

6.2.2 Behavior of Steel Columns Subjected to Combined Axial and Lateral Loading

- Steel columns subjected to a combined axial and cyclic loading scheme are experiencing local and lateral-torsional buckling effects that are reducing their strength significantly at drift levels much lower than expected based on current AISC seismic design requirements. This indicates that the current requirements are not conservative.

- Statistical analysis indicates that the web width-to-thickness ratio and unbraced length to radius of gyration play the most significant role in predicting the critical axial load ratio provided the current AISC flange width-to-thickness seismic requirements are satisfied.
- The ability to predict the amount of load under which a column can still be expected to perform as a highly ductile member (i.e. be able to support the applied axial load up to 4% drift) is made possible with the proposed design aide.
- Additional studies using the monotonic drift-then-load protocol indicate that while an increase in the lateral drift ratio decreases the final axial load capacity, it is relatively insignificant compared to the effect of increasing the initial axial load.
- Axial shortening is well correlated to the amount of local buckling present in a member. Reducing the amount of local buckling with limits on slenderness parameters will therefore limit the amount of axial shortening.
- The assumption that local buckling in hot rolled sections is as severe of a load path interruption as removal of the flange or web elements is invalid. While there is a slight reduction due to an interruption of the load path, locally buckled regions are still able to transfer a considerable amount of the axial load.
- While the load path interruption is minor, local buckling under a combined loading scheme also alters and weakens the boundary conditions leading to a reduction in the axial resistance of deep wide-flange members that are already susceptible to lateral torsional behavior.

6.2.3 Visualization of Complex Spatial Arrangements using Virtual Reality

- Static and dynamic virtual reality models can be created in CAD or finite element software environments and used as supplemental tools in undergraduate steel design courses.
- Qualitative and quantitate results indicate that the virtual reality tools created help improve student understanding of buckled shapes. These tools can be modified and expanded upon to address a variety of complex structural configurations.

6.3 FUTURE WORK

The work presented in this dissertation provides the groundwork for several different research directions. The suggested areas of research are described in detail below.

6.3.1 Behavior of Locally Web-Damaged Steel Columns

While the work here focused on the behavior of steel columns subjected to local flange damage, the computational and analytical techniques could be extended to address local web damage. Since local flange damage can cause a severe reduction in the axial capacity of the member, it would be prudent to know the effect of local damage to the web which can result from corrosion or removal for electrical or HVAC equipment access in existing structures.

6.3.2 Behavior of Steel Columns Subjected to Combined Axial and Cyclic Loading

The effect of different loading protocols and boundary conditions at the member level need to be explored to ensure the versatility of the proposed design aides in adequately predicting steel column behavior under a combined axial and reversed lateral loading scheme.

Additional studies to determine the role that local, flexural, and lateral-torsional buckling at the member level play in promoting vertical progressive collapse of seismically loaded steel moment-resisting frames would also be greatly beneficial.

Using detailed finite element models of the sort utilized here, an incremental dynamic analysis (IDA) framework could be utilized to identify and quantify the degree of collapse resistance of full structural systems to selected ground motions. The proposed IDAs would be more sophisticated than those commonly found in the literature because the developed finite element models will be able to explicitly account for member deterioration and separation in a comprehensive and realistic manner. Previous IDAs were typically based on plastic hinge analysis in which local and global instabilities were not accounted for and therefore they could not fully address progressive collapse vulnerability in the same manner as the proposed simulations.

The information gained from the system level studies would provide valuable information for how much lateral restraint is needed to ensure good column behavior under extreme seismic events. It would also provide reasonable levels of axial loads that should be applied as well as cyclic loading schemes in both vertical and lateral directions for future experimental testing.

6.3.3 Visualization of Complex Spatial Arrangements using Virtual Reality

The virtual reality tools presented provide a platform for additional concepts in the field of civil engineering to be addressed using these methods. The results of the qualitative study indicate the characteristics of the models that students felt contributed most to their increased understanding of the topic and could be useful in guiding the creation of future educational tools.

REFERENCES

Abdel-Lateef, T.H., Dabaon, M.A., Abdel-Moez, O.M., and Salama, M.I. (2000). "Buckling of columns with sudden change in cross section." *Proceedings of Mansoura Third International Engineering Conference*, Mansoura, Egypt.

Abdel-Lateef, T.H., Dabaon, M.A., Abdel-Moez, O.M., and Salama, M.I. (2001). "Buckling loads of columns with gradually changing cross-section subjected to combined axial loading." *Proceedings of Fourth Alexandria International Conference on Structural and Geotechnical Engineering*, Alexandria, Egypt.

Agresti, A. and Finlay, B. (2009). *Statistical Methods for the Social Sciences*, 4th Edition. Pearson, Upper Saddle River, NJ.

AISC (American Institute of Steel Construction). (2010). *Steel construction manual*, 14th Ed. AISCE, Chicago, IL.

AISC (American Institute of Steel Construction). (2010) *Seismic Design Manual*, 2nd Ed. AISC, Chicago, IL.

Altair Computing. (2011). Hypermesh Version 11.0. Altair Engineering Inc. Troy, MI.

Al-Thairy, H and Wang, YC. (2011). "A numerical study of the behavior and failure modes of axially compressed steel columns subjected to transverse impact." *J. Impact Eng.*, 38, 732-44.

ANSI/AISC 341-10. (2010). Seismic Provisions for Structural Steel Buildings. American Institute for Steel Construction, Chicago, IL.

Brown, A.L. (1992). "Design Experiments: Theoretical and Methodological Challenges in Creating Complex Interventions in Classroom Settings." *J. of the Learning Sciences*, 2(2), 141-178.

Carberry, A., Ohland, M., and Swan, C. (2010). "A pilot validation study of the Epistemological Beliefs Assessment for Engineering (EBAE): First-Year Engineering Student Beliefs", *ASEE Annual Conference & Exposition*. Louisville, KY.

Chajes, A. (1974). *Principles of Structural Stability Theory.* Prentice Hall, Englewood Cliffs, NJ.

Chaturvedi, S. and Akan, O. (2011). "Simulation and Visualization Enhanced Engineering Education – Development and Implementation of Virtual Experiments in a Laboratory Course." *Proc. of 1st World Eng. Education Flash Week*, Lisbon, Portugal.

Chatterjee, S., Hadi, A., and Price, B. (2000). *Regression Analysis by Example.* 3rd Ed. Wiley, New York, NY.

Chi, B, and Uang, C. (2002). Cyclic Response and Design Recommendations of Reduced Beam Section Moment Connections with Deep Columns. *J. of Struct. Eng.*, 128(4), 464-473.

Chen, W. and Lui, F. (1987) *Structural Stability: Theory and Implementation*. Elsevier Science Publishing, New York.

Cheng, X, Chen, Y., and Pan, L. (2013). Experimental study on steel beam-columns composed of slender H-sections under cyclic bending. *J. of Struct. Eng.*, 128(4), 464-473.

Cobb, P., Confrey, J., diSessa, A., Lehrer, R., and Schauble, L. (2003). "Design Experiments in Educational Research," *Educ. Researcher*, 32(9), 9-13.

Cook, R.D., Malkus, D.S., Plesha, M.E., and Witt, R.J. (2001). *Concepts and Applications of Finite Element Analysis*. 4th ed. Wiley, New York, NY.

Cruz-Neira, C., Sandin D., DeFanti, T., Kenyon, R., and Hart, J. (1992). "The Cave: Audio Visual Experience Automatic Virtual Environment." *Communications of the ACM*, 35(6), 64-72.

Dey, A. (1999). *Grounding Grounded Theory: Guidelines for Qualitative Inquiry.* Emerald Group Publishing Limited, Bingley, England.

Elkady, A. and Lignos, D. (2015). Analytical investigation of the cyclic behavior and plastic hinge formation in deep wide-flange steel beam-columns. *Bull. Earthquake Eng.*, 13, 1097-1118.

Engelmann B.E, Whirley, R.G., and Goudreau, G.L. (1989). "A simple shell element formulation for large-scale elastoplastic analysis." In *Analytical and Computational Models of Shells*, Noor, A.K., Belytschko, T., and Simo, J.C., Eds., CED-Vol. 3, ASME, New York, NY.

Fadden, M. and McCormick, J. (2014). "Finite Element Model of the Cyclic Bending Behavior of Hollow Structural Sections." *J. Constr. Steel Res., 94*, 64-75.

FEMA 273. (2000). State of the Art Report on Systems Performance of Steel Moment Frames Subject to Earthquake Ground Shaking, prepared by Helmut Krawinkler for the SAC Joint Venture Partnership.

Ferrer, B., Ivorra, S., Segovia, E., and Irles, R. (2010). "Tridimensional modelization of the impact of a vehicle against a metallic parking column at a low speed." *Eng. Struct.*, 32, 1986-92.

Gambhir, M.L. (2004). *Stability Analysis and Design of Structures.* Springer, Germany.

Haladyna, T., Downing, S., Rodriguez, M. (2002). "A Review of Multiple-Choice Item-Writing Guidelines for Classroom Assessment." *Applied Measurement in Educ.*, 15(3), 309-334.

Hallquist, J. (2005). *LS-DYNA,* Livermore Software Technology Corp., Livermore, CA.

Jones, N. (1989). *Structural Impact.* Cambridge University Press, New York, NY.

Kaufman, E., Metrovich, B., and Pense, A. (2001). Characterization of Cyclic Inelastic Strain Behavior on Properties of A572 Gr. 50 and A913 Rolled Sections. *ATLSS Report No. 01-13*, National Center for Engineering Research on Advanced Technology for Large Structural Systems, Lehigh University, Bethlehem, PA.

Khandelwal, K., El-Tawil, S., Kunnath, S.K. and Lew, H.S. (2008) "Macromodel-Based Simulation of Progressive Collapse: Steel Frame Structures." *J. of Struct. Eng.* 134(7), 1070-1078.

Koretsky, M. Kelly, C. and Gummer, E. (2011). "Student Perceptions of Learning in the Laboratory: Comparison of Industrially Situated Virtual Laboratories to Capstone Physical Laboratories," *J. of Eng. Educ.*, 100(3), 540-573.

Krishnan, S. and Muto, M. (2012). Mechanism of Collapse of Tall Steel Moment Frame Buildings under Earthquake Excitation. *J. of Struct. Eng.*, 138(11), 1361-1387.

Lamarche, C. and Tremblay, R. (2011). Seismically induced cyclic buckling of steel columns including residual – stress and strain-rate effects. *J. of Constr. Steel Res.*, 67, 1401-1410.

Lee, E-J and El-Tawil, S. (2008), "FEMvrml: An Interactive Virtual Environment for Visualization of Finite Element Simulation Results" *Adv. Eng. Software, Elsevier*, 39, 737–742.

Lee, K., Kim, T., and Kim, J. (2009). "Local response of W-shaped steel columns under blast loading." *Struct. Eng. and Mechanics*, 31(1), 25-38.

Leydans, J., Moskal, B., and Pavelich, M. (2004). "Qualitative Methods Used in Assessment of Engineering Education." *J. of Eng. Educ.*, 94(1), 13-25.

Lignos, D. (2008), "Sidesway collapse of deteriorating structural systems under seismic excitations," PhD. Dissertation, Stanford University, Palo Alto, CA.

Lignos, D., and Krawinkler, H. (2009). "Sidesway Collapse of deteriorating structural systems under seismic excitations. *Report No. TB 172*, John A. Blume Earthquake Engineering Research Center, Department of Civil & Environmental Engineering, Stanford University, Stanford, CA.

Lignos, D., and Krawinkler, H. (2011). "Deterioration Modeling of Steel Components in Support of Collapse Prediction of Steel Moment Frames under Earthquake Loading." *Earthquake J. Struct. Eng.*, 137(11), 1291-1302.

Lignos, D., Krawinkler, H., and Whittaker, A.S. (2011). "Prediction and validation of sidesway collapse of two scale models of a 4-story steel moment frame." *Earthquake Eng. Struct. Dyn.*, 40, 807-825.

MacRae, G.A., Carr, A.J., Walpole W.R. (1990). The seismic response of steel frames." *Report No. 90-6*, Department of Civil Engineering, University of Canterbury, Christchurch.

Moehle, J.P., Elwood, K.J., and Sezen, H., (2002), "Gravity load collapse of building frames during earthquakes," *S. M. Uzumeri Symposium: Behavior and Design of Concrete Structures for Seismic Performance, ACI Special Publication (SP-197)*, American Concrete Institute, 215-238.

Nakashima, M., Takanashi, K., and Kato, H. (1990). "Test of Steel Beam-Columns Subject to Sidesway." *J. Struct. Eng.*, 116(9), 861-868.

Nakashima, M., and Liu, D. (2005). "Instability and Complete Failure of Steel Columns Subjected to Cyclic Loading." *J. Struct. Eng.*, 131 (6), 559-567.

Newell, J. and Uang, C. (2006). Cyclic Behavior of Steel Columns with Combined High Axial Load and Drift Demand. *Report No. SSRP-06/22*, Department of Structural Engineering, University of California, San Diego, La Jolla, CA.

Oliver, D., Serovich, J., and Mason, T. (2006). "Constraints and Opportunities with Interview Transcription: Towards Reflection in Qualitative Research." *Social Forces*, 84(2), 1273-1289.

Paik, J. and Thayamballi, A. (2007). *Ship-shaped Offshore Installations: Design, Building, and Operation*. Cambridge University Press, New York, NY.

Patton, M.Q. (2001). *Qualitative Evaluation and Research Methods,* 2nd Edition. Sage Publications, Thousand Oaks, CA.

Raftoyiannis, I.G. and Ermopoulos, J.Ch. (2005). "Stability of tapered and stepped steel columns with initial imperfections." *Eng. Struct.*, 27, 1248–57.

Ragan, E.D., Huber, K., Laha, B., and Bowman, D.A. (2012). "The Effects of Navigational Control and Environmental Detail on Learning in 3D Virtual Environments." *IEEE Virtual Reality,* Costa Mesa, CA.

Ricles, J., Mao, C., Lu, L-W, and Fisher, J. (2003). "Ductile Details for Welded Unreinforced Moment Connections Subject to Inelastic Cyclic Loading," *J. of Eng. Struct.*, Elsevier, 25, 667-680.

Schnabel, M., and Kvan, T. (2003) "Spatial Understanding in Immersive Virtual Environments," *Int. J. of Architectural Computing*, 4(1), 435-448.

Setzler, E., and Sezen, H. (2008) "Model for the Lateral Behavior of Reinforced Concrete Columns Including Shear Deformations," *Earthquake Spectra*, 24(2), 493-511.

Shen, J.-H. J., Astaneh-Asl, A., and McCallen D.B. (2002). "Use of Deep Columns in Special Steel Moment Frames," Steel Tip Report No. 24, Structural Steel Educational Council, Moraga, CA.

Sim, S.H., Spencer, B.F., and Lee, G.C. (2009). "Virtual laboratory for experimental structural dynamics," *Computer Appl. in Eng. Educ.*, 17(1), 80-88.

Sorby, S. (1999). "Developing 3-D Spatial Visualization Skills," *Eng. Design Graphics J.*, 63(2): 21-32.

Suita, K., Yamada, S., Tada, M., Kasai, K., Matsuoka, Y., and Sato, E. (2007). "E-Defense tests on full-scale steel buildings: Part 2-Collapse experiments on moment frames." *Proc. of ASCE Structures Congress,* ASCE, Reston, VA.

Suita, K., Yamada, S., Tada, M., Kasai, K., Matsuoka, Y., and Sato, E. (2008). "Results of recent E-Defense tests on full-scale steel buildings: Part 1-Collapse experiment on 4-story moment frame." *Proc. of ASCE Structures Congress,* ASCE, Reston, VA.

Takizawa, H, and Jennings, P. (1980). "Collapse of a Model for Ductile Reinforced Concrete Frames under Extreme Earthquake Motions" *Earthquake Eng. Struct. Dyn.*, 8, 117-144.

Trahair, N.S., Kayvani, K. (2005). "On the design of damaged steel columns." *Research Report No. R846,* University of Sydney, Sydney, Australia.

Tversky, B, Morrison, J., and Betrancourt, M. (2002). "Animation: can it facilitate?" *International J. of Human Computer Studies*, 57, 247-262.

Uang, C-M., Ozkula, G., and Harris, J. (2015). "Observations from Cyclic Tests on Deep, Slender Wide-Flange Structural Steel Beam-Column Members." *Proc. of Annual Stability Conference*, SSRC, Chicago, IL.

Velez, M.C. Silver, D., Tremaine, M. (2005). "Understanding Visualization through Spatial Ability Differences." *IEEE Visualization*, VIS 2005, 511-518.

Vian, D. and Bruneau, M. (2001), "Experimental investigation of P-Delta effects to collapse during earthquakes," *Technical Report MCEER-01-0001*.

Vian D, Bruneau M. (2003), "Tests to structural collapse of single degree of freedom frames subjected to earthquake Excitations," *J. of Struct. Eng,* 129**,** 1676–1685.

Wai, J., Lubinski, D., and Benbow, C. (2009). "Spatial Ability for STEM Domains: Aligning Over 50 Years of Cumulative Psychological Knowledge Solidifies Its Importance." *J. of Educ. Psychology*, 101(4): 817-835.

Wu C-L., Yang, Y-S, Hwang, S-J, and Loh, C-H. (2010), "Dynamic Collapse of Reinforced Concrete Columns." *Proc. Of 9th U.S. National and 10th Canadian Conference on Earthquake Eng.* EERI, Oakland, CA.

Yossef, N., Fogarty, J., and El-Tawil, S. (2014). "Residual Compressive Strength of Flange-Damaged Steel Columns," *J. Struct. Eng.*, 10.1061/(ASCE)ST.1943-541X.0001226, 04014241.

Zareian, F., Krawinkler, H., Ibarra, L., and Lignos, D. (2010), "Basic Concepts and Performance Measures in Prediction of Collapse of Buildings under Earthquake Ground Motions," *Struct. Des. Tall and Special Build.*, 19, 167-181.

Zargar, S., Medina, R.A., and Miranda, E. "Cyclic Behavior of Deep Steel Columns Subjected to Large Drifts, Rotations, and Axial Loads," *Proc. of the 10th U.S. National Conference on Earthquake Engineering*, EERI, Oakland, CA.

Zeinoddini, M., Harding, J.E., and Parke, G.A.R. (2008). "Axially pre-loaded steel tubes subjected to lateral impacts (a numerical simulation)." *J. Impact Eng.*, 35(11), 1267-1279.

Zeinoddini, M., Parke, G.A.R., and Harding, J.E. (1999). "Dynamic behavior of axially pre-loaded tubular steel members of offshore structures subjected to impact damage." *Ocean Eng.*, 26, 963-978.

Zeinoddini, M., Parke, G.A.R., and Harding, J.E. (2002). "Axially pre-loaded steel tubes subjected to lateral impacts: an experimental study." *J. Impact Eng.*, 27(6), 669-690.

Ziemian, R. (2010). *Guide to Stability Design Criteria for Metal Structures.* Wiley, Hoboken, N.J.